# Identifying and Characterising Eclipsing Binary Stars in the MOSES Survey

by

**Jade Atanya Cullen**

A thesis submitted in partial fulfilment of the requirements for the degree of Master of Science (by Research)



Jeremiah Horrocks Institute
University of Central Lancashire

March 2022

# Declaration

**Type of Award:** Master of Science

**School:** Natural Sciences

I declare that while registered as a candidate for the research degree, I have not been a registered candidate or enrolled student for another award of the University or other academic or professional institution.

I declare that no material contained in the thesis has been used in any other submission for an academic award and is solely my own work.

No proof-reading service was used in the compilation of this thesis.

Jade Atanya Cullen

March 2022

**Abstract**

This thesis presents the research methods and results from analysing data from the MOSES survey in search of variable stars. The work focuses on classifying and analysing light curves of eclipsing binary stars. Of the 33,038 stars in the MOSES survey that were analysed, 697 of them were determined to be variable objects. Using a custom written version of Phase Dispersion Minimisation (PDM), 70 of these variable objects were determined to be eclipsing binary (EB) stars, with 12 newly discovered, and their periods were subsequently determined. The EBs were analysed using PHOEBE to plot their phased light curves and determine the eclipse widths, depths of minima, and ingress and egress times. A subgroup of EBs were classified into their subclasses, resulting in 7 Algol type systems, 5 $\beta$ Lyrae type systems, and 3 W UMa type systems. This subgroup was also analysed to find the ratios of the temperatures between the component stars, and the relative diameters of the components in terms of their orbital separation. For 11 of the EBs analysed in detail, TESS data are also available. The TESS data were analysed using the same methods and when compared with the results from the MOSES data there was found to be good congruence between results.

# Contents

# Acknowledgements

I would like to thank my primary supervisor Dr Daniel Holdsworth for his continuous guidance and support throughout this project. His knowledge and advice have been invaluable. I would also like to thank my secondary supervisor Dr Mark Norris for his knowledge regarding the MOSES survey and his ideas and feedback on the direction of my project.

I would also like to extend special thanks to my friends and family for their ongoing encouragement throughout my entire university career, and to my late great-grandmother whose pride in my academic achievements continues to motivate me to this day.

# List of Figures

x

# List of Tables

# 1 Introduction

## 1.1 Variable Stars

Variable stars are defined as stars that vary in apparent brightness over time. Variable stars can be classed as either intrinsic variables or extrinsic variables. Intrinsic variables vary due to physical properties of the star, whereas extrinsic variables vary due to external properties.

Intrinsic variables include:

- Pulsating variables

- Eruptive variables/Cataclysmic variables

Extrinsic variables include:

- Eclipsing variables

- Rotating variables

The different types of variable stars will be discussed below, with emphasis on the eclipsing binary stars.

## 1.2 Intrinsically Variable Stars

### 1.2.1 Pulsating Variables

Pulsating variables are stars whose stellar radii grow and shrink over time due to the expansion and contraction of the star's surface layers. As the star's dimensions change

their spectral properties change as well. Pulsations are caused by evolutionary changes within the stars, with typically the more evolved, older stars that pulsate.

Pulsations in stars can be described as radial or non-radial, meaning either the whole star expands and contracts at the same time or one part of a star expands while another part contracts. There are several types of pulsating variables, however the main types to be aware of for this project are Cepheids, RR Lyrae, RV Tauri, and Long-Period Variables.

Cepheids are characterised by periods of around 1-100 days and are very massive, luminous stars that pulsate radially (Catelan & Smith 2015). They are found on the instability strip of an HR diagram and have a strong period-luminosity relationship, which allows the distance to the star to be determined and allows them to be used as standard candles. Type I cepheids are population I, yellow giants and supergiants, with typical periods between 5-10 days. Type II cepheids are population II variable stars, with typically longer periods than their type I counterparts, usually of 1-25 days, and are also intrinsically less luminous (Catelan & Smith 2015). A typical cepheid light curve is characterised by a sawtooth pattern, as can be seen in Figure 1. The shape of the light curve is caused by the phase difference between the temperature and radius variations, causing a steep rise in light intensity followed by a more gradual decrease.
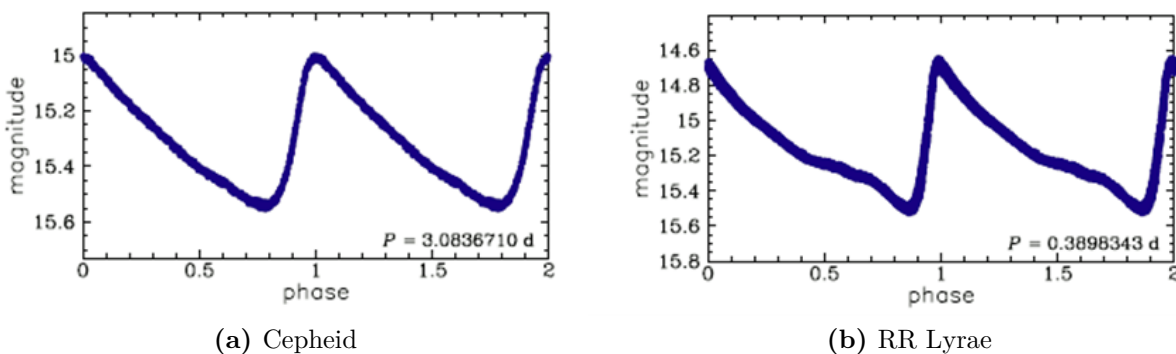


**(a)** Cepheid            **(b)** RR Lyrae

**Figure 1:** An example light curve of a classical Cepheid (HV 5558) and an RR Lyrae variable (V2438). (Udalski et al. 2015)

RR Lyrae variables are another type of pulsating variable. They are population II stars that are less massive than cepheids and are commonly found in globular clusters,

with short periods of 0.2-1.0 day and are also found in the instability strip (Catelan & Smith 2015). They also have a period-luminosity relationship, allowing distances to RR Lyrae stars to be determined. An example of their light curve can be seen in Figure 1 which can be seen to be similar in shape to a cepheid type variable.
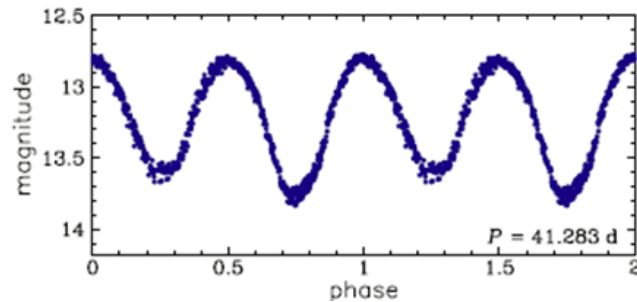


**Figure 2:** An example light curve of a RV Tauri star. (Udalski et al. 2015)

RV Tauri variables have periods of 30-150 days and are yellow supergiants which are post AGB (asymptotic giant branch). An example light curve can be seen in Figure 2 which is characterised by a pattern of deep and shallow minima, similar to an eclipsing binary (henceforth EB) light curve. However, RV Tauri show significant modulation in their maxima and minima, whereas EB type stars do not, and the phase difference between harmonics varies more for RV Tauri stars than for EBs.
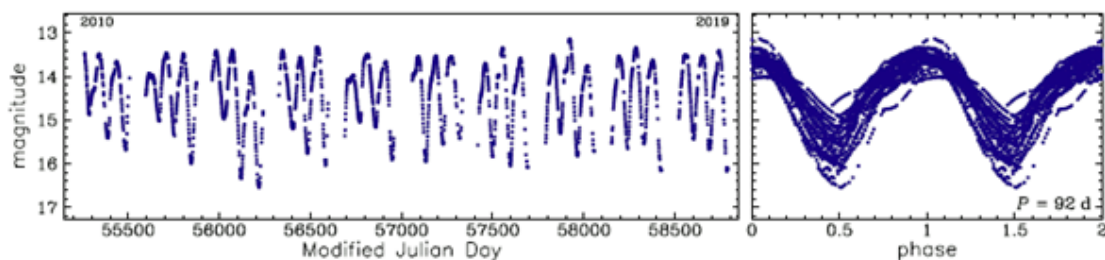


**Figure 3:** An example light curve of a Mira variable, a type of Long-Period variable. The left image shows the unfolded light curve, and the right shows the phase-folded version. (Udalski et al. 2015)

Long-Period Variables are characterised by their long periods, typically 80-1000 days, and are cool red giants or supergiants (Catelan & Smith 2015). These variables can be population I or II and are typically found on the AGB of an HR diagram. An example light curve can be seen in Figure 3. These types of variables tend to vary slightly cycle to cycle.

## 1.2.2 Eruptive/Cataclysmic Variables

Eruptive variables are stars whose variability is caused by mass ejection or chromospheric activity (Simonsen 2012). Young Stellar Objects (YSOs) are pre-main sequence stars that may be eruptive variables due to instabilities in their accretion disks or violent activity in their stellar atmosphere (Simonsen 2012). Other types of eruptive variables include flare stars that vary due to the ejection of mass, and rapidly rotating variables that vary due to mass outflow from their equatorial zones and the formation of equatorial rings or disks (Simonsen 2012).

Another type of eruptive variable are novae. They occur in close binary systems and are caused by thermonuclear fusion of material that is accreted onto a companion star. Polars are binary star systems in which the magnetic field of the white dwarf companion has synchronised the latter's rotational period with the binary orbital period, resulting in matter from the donor star being magnetically channelled onto the white dwarf rather than forming a disk. Symbiotic variables are close binaries with a large cool component that loses mass from its outer layers via stellar winds to a hotter, compact companion star and accretion disk. These are all eruptive variables characterised by mass ejection.

Cataclysmic variables are systems that undergo large amplitude outbursts and result in the destruction of the star. Supernovae are a type of cataclysmic variable that are characterised by a sudden, extreme increase in brightness. Type Ia supernovae result from binary systems which contain a white dwarf which accretes enough mass to surpass its Chandrasekhar limit, leading to a runaway thermonuclear explosion (Knigge et al. 2011). Type II supernovae occur when a very massive single star has fused all the material in its core to iron, leading to a decrease in radiation pressure and resulting in the gravitational collapse of the star, ending with the explosion of the star as the core collapses.

X-ray variables are a type of cataclysmic variable in which material from a donor

star falls onto a compact object or accretion disc. They are binary systems that contain neutron stars or blackholes (Simonsen 2012). One type of X-Ray variable is a Gamma Ray Burster (GRB). A GRB is an extremely energetic explosion that has been observed in a distant galaxy which releases an abundance of gamma rays. They typically last 20-40 seconds but can range from 10 ms, to several minutes, up to several hours (Gendre et al. 2013).

## 1.3  Extrinsically Variable Stars

### 1.3.1  Rotating Variables

A rotating variable is a star whose variability is related to their rotation, such as those with starspots, and tidally locked stars. Starspots are areas on a star's surface that appear dimmer or brighter due to being cooler or hotter than the surrounding area and are created by strong, local magnetic fields (Catelan & Smith 2015). When a star rotates, these starspots will rotate in and out of view, causing the observed brightness of the star to vary. An example of this would be our own Sun. Our Sun has starspot activity and as it rotates, we are able to detect a change, albeit very small, in its brightness. The spots themselves are not constant and can disappear and reappear dependant on activity on the star's surface. For our Sun this is well observed and recognised as the 11-year sunspot cycle. An example of a rotating variable light curve can be seen in Figure 4. This shows a pattern that could be confused with an eclipsing binary light curve, however rotating variables tend to have irregularities in their light curve as it changes in shape from one cycle to the next and their periods are close to the length of time it takes for the star to rotate.

Stars that are part of a close binary system may be so close together that they are tidally locked with each other and subject to reflection effects. This causes the hotter star to heat up the part of its companion star that is facing it, which in turn causes that part of the star to appear brighter. As the binary system rotates its brightness
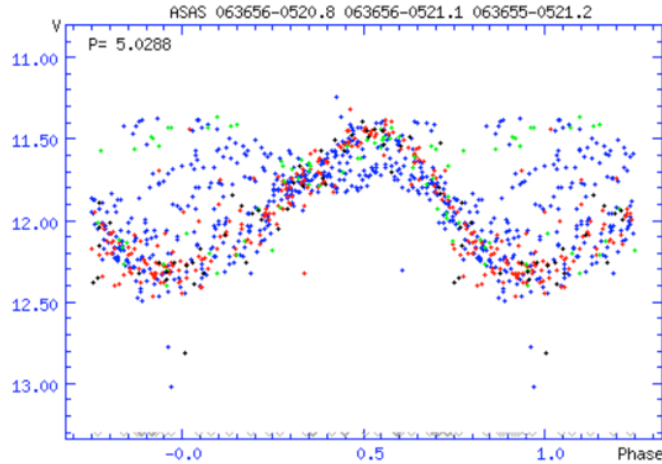
**Figure 4:** An example light curve of a rotating variable (BY Dra). (Simonsen 2012)

can thus be seen to vary. The component stars of tidally locked binary systems can also be distorted due to the gravitational stress put on them by their companion star. This causes the component stars to be non-spherical, meaning that the surface area viewed by an observer changes as the stars rotate. Since the observed surface area changes, the brightness observed also changes, causing the system to vary in brightness. These are known as ellipsoidal variables.

### 1.3.2 Eclipsing Binary Stars

Eclipsing variables are another type of extrinsically variable star and are the focus of this research. They are a binary star system in which two or more stars orbit each other and cause a variation in brightness when the stars eclipse one another relative to the observing plane. Their light curves are characterised by periodic drops in brightness when one star eclipses another. The largest decrease in brightness is known as the primary eclipse, typically when the cooler star passes in front of the hotter star.

Eclipsing variables are important to scientific research because binary stars make up over 50% of our solar neighbourhood and those with observable eclipses are our primary source of knowledge to understand the fundamental properties of stars (Kallrath & Milone 2009a). Many parameters of the component stars in EBs can be determined. Absolute parameters may be derived if both a light curve and radial velocity curve is available

for the system, and relative quantities may be determined if only one of the two is available. These parameters include orbital inclination, radius, mass, luminosity, effective temperature, and distance to the system. Determination of these parameters in eclipsing binaries is relatively easy and more accurate in comparison with other stars, making eclipsing binaries a useful tool in testing stellar structure and stellar evolution theories (Kallrath & Milone 2009a). They are also useful in improving our understanding of Wolf-Rayet stars, novae, and X-ray binaries.

EBs can be split into three main classes based on their light curves: Algols, $\beta$ Lyrae systems, and W Ursae Majoris systems.

Algols (detached binary/semi-detached binary): The prototype for Algols is $\beta$ Persei, known as Algol. These EBs are characterised by constant light outside of their eclipse. Their minima dip and rise again abruptly and take up only a small portion of the phased light curve, as seen in Figure 5 (Kallrath & Milone 2009a). They typically have long periods but they can range from less than a day to several years, and there is little interaction between their components.
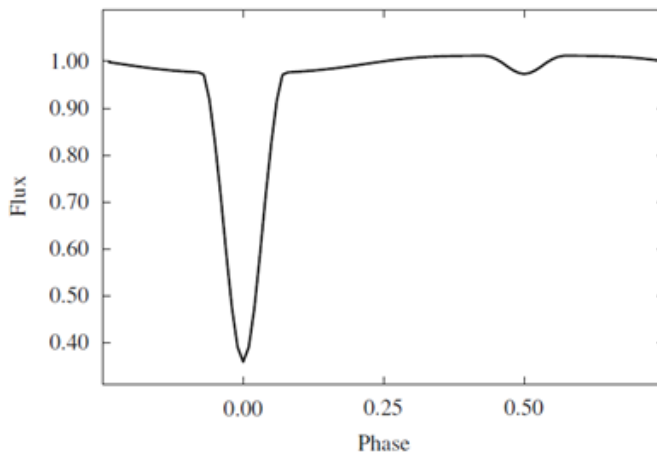


**Figure 5:** The light curve for $\beta$ Persei. (Kallrath & Milone 2009a)

$\beta$ Lyrae (semi-detached): The prototype for these EBs is $\beta$ Lyrae. Their light curves continuously vary across the cycle of variation, and their minima occupy a sizeable portion of their phased light curve, as shown in Figure 6 (Kallrath & Milone 2009a). They have periods usually of days, or longer if giants/supergiants are involved. The continuous

variation of light is partially due to the changing aspects of the stars as they rotate (ellipsoidal variation). The relative depths of minima indicate the temperature difference between components. The stars involved interact gravitationally with each other, causing tidal forces to distort the shapes of the stars (Kallrath & Milone 2009a).
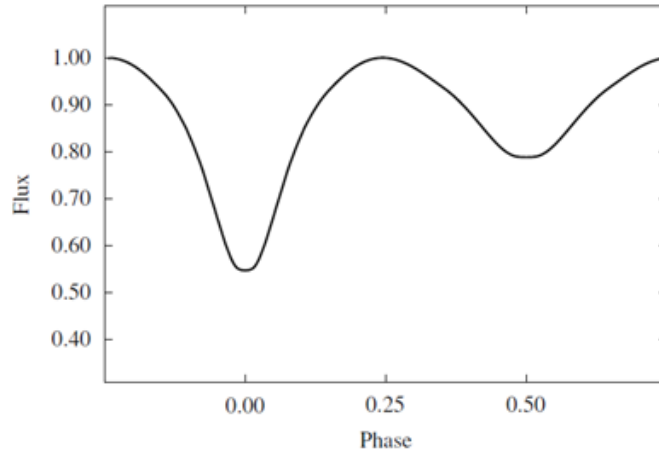


**Figure 6:** The light curve for $\beta$ Lyrae. (Kallrath & Milone 2009a)

W Ursae Majoris or W UMa (contact binary/overcontact binary): The prototype for this type of EB is W Ursae Majoris. They are typically eclipsing binary systems with periods less than a day. Their light curves vary continuously, with the depths of their minima being very similar, but rarely identical, as can be seen in Figure 7 (Kallrath & Milone 2009a). The binaries are in physical contact with each other, connected by a neck, not a stream. An A-type system is defined by the more massive star being both larger and hotter, and a W-type system is defined by the more massive star being larger but cooler (Kallrath & Milone 2009a).

Another way to classify eclipsing binary systems is dependant on the distance between the component stars, relative to their sizes. This splits them into three main classes: Detached binaries, semidetached binaries, and contact/overcontact binaries.

In a detached binary the component stars are within their Roche lobes as can be seen in Figure 8 (Detached), are spherical in shape (unless they are a fast rotator) and have no physical contact with each other. The component stars do not affect the evolution of their companion stars. Most binary stars fall into this category.
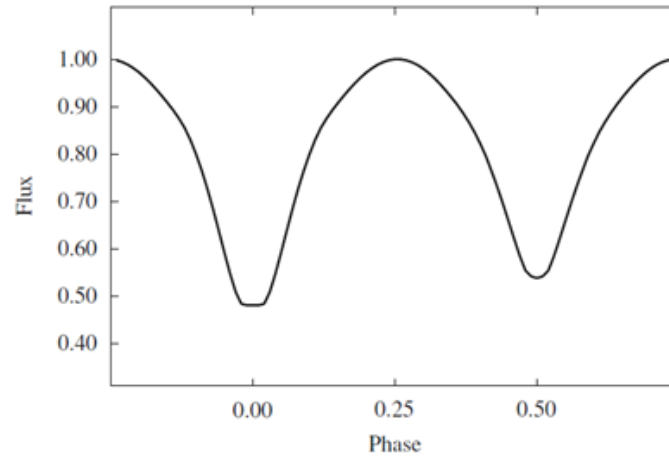
**Figure 7:** The light curve for W UMa. (Kallrath & Milone 2009a)

In a semi-detached binary only one of the component stars has filled its Roche lobe as can be seen in Figure 8 (Semi-detached). The distorted donor star transfers gas from its surface to its companion, often forming an accretion disc around the companion star due to the high angular momentum of the inflowing matter.

In a contact binary, both component stars have filled their Roche lobes as seen in Figure 8 (Contact) and are so close that they are in contact with each other. The more massive star can transfer mass to its companion star, often until they are of similar effective temperatures and luminosities when there is substantial thermal contact (Ivanova et al. 2013). They can share a common gaseous envelope that surrounds both stars, making what is sometimes known as an overcontact binary that can lead to the merging of the component stars as the shared envelope slows their orbital motion (Csizmadia & Klagyivik 2004).
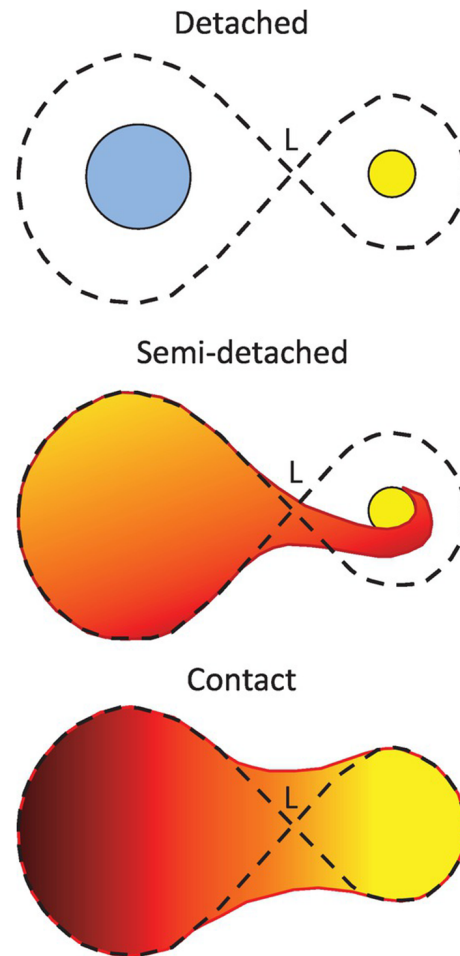
**Figure 8:** A diagram of the different Roche lobe configurations for different types of binary star systems. The 'L' labels show where the Lagrangian point is in the system, the area where the net gravity is zero and the point where mass transfer passes through. The dotted line shows the boundaries of the Roche lobes in the system. (Walker 2017)

# 2 Previous Research in the Field

## 2.1 Previous Research on Eclipsing Binary Stars

In the late 1700s and early 1800s, William Herschel observed several double stars (two stars that appear close together in the sky) and eventually came across two stars in orbit around one another. In his research he first coined the term "binary star" to describe such systems. In 1782, John Goodricke proposed a mechanism to explain the variability observed in Beta Persei (Algol). He suggested that its variability could be caused by starspots or similar, or that a large body could be orbiting the star. Edward Pickering presented evidence of the latter proposal in 1881, and Beta Persei was confirmed as an eclipsing binary in 1889 by Carl Vogel when he found periodic doppler shifts in its spectrum (Vogel 1890). Thus, Beta Persei was one of the first known spectroscopic binaries.

Research on binary star light curves was first led by Henry Russell who employed rigorous mathematical models to estimate parameters of the system (Russell & Merrill 1952). Zdenek Kopal was another key researcher in the field who adopted the use of the Roche model equipotentials to model the surfaces of the stars (Kopal 1959). Once computers became more commonplace the research area prospered with programs to model the stars using Roche geometry now plausible. The Wilson-Devinney program was one such program that emerged during this time (Wilson & Devinney 1971). It also implemented least-squares analysis to determine light curve parameters. This program is still in use and being built upon by other researchers to this day.

The light curve of an eclipsing binary star can yield a plethora of information about the stars involved and the methods to derive such parameters are relatively simple. The period of the system can be derived by finding the time between primary eclipses in the light curve data. There are several methods that can be used to do this and are subsequently discussed in section 4. The radii of the component stars may also be found

with respect to the orbital seperation by looking at the ingress and egress times, and the times when maximum eclipse depth starts and ends for the secondary eclipse. These give the required information to calculate the radii of the stars and assumes an inclination angle of 90°. The ratio of the temperatures of the component stars can also be found by comparing the relative depths of the primary and secondary eclipses. The equations required for this analysis can be found in section 3.

Absolute parameters can be derived if radial velocity data is available for the system. Using the width of the eclipses and the radial velocity of each star allows the radius of each star to be found. The semi-major axis may be found by calculating the orbital radius of each star using the period of the system and each star's orbital velocity. This then allows the masses of each star to be found using Kepler's third law. To derive the temperatures of the component stars requires full spectral modelling of each star's photosphere, but finding the temperatures allows the luminosities of each star and the distance to the system to also be found.

## 2.2 Modern Surveys that detected Eclipsing Binary Stars

### 2.2.1 Kepler

The Kepler space telescope was initially sent on a 3.5-year mission by NASA in order to find Earth-size and smaller planets that are in or near their respective habitable zones by searching for planetary transits (Borucki et al. 2007). It was launched on the 7th of March 2009 into an Earth-trailing heliocentric orbit. Kepler continued on an extended mission until it ran out of fuel and retired on the 30th of October 2018. Kepler has observed over 500,000 stars and detected more than 2,600 confirmed planets and over 2,000 eclipsing binary stars.

Kepler had a fixed field-of-view on the sky, surveying a portion of Earth's region of the Milky-Way. The mission focused on determining how many Earth-sized exoplanets

there were in, or near, the habitable zones of their host stars for a wide variety of spectral types. Other goals included determining orbital parameters of the planets, estimating how many planets are in multiple-star systems, and determining the properties of stars that have planets orbiting them (Borucki et al. 2007).

The Kepler photometer is a Schmidt telescope design with a 0.95 metre aperture and 1.4 metre primary mirror, with a field-of-view of 105 square degrees and wavelength range of 400 – 850 nm (Borucki et al. 2007). It contained an array of 42 CCDs each with 2200x1024 pixels, giving a total resolution of 94.6 megapixels (Borucki et al. 2007). However, due to the limitations of storing and sending data back to Earth, relevant pixels were preselected for each star, bringing the resolution down to around 5.4 megapixels as less pixels were utilised (Borucki et al. 2007).

Some of the Kepler data for eclipsing binary stars were utilised in this project in order to develop code that can determine the periods of these systems. As Kepler was a space-based telescope, its data quality is much higher that the ground-based data for MOSES, providing a good starting point for testing the reliability of the code written and testing its accuracy against the known orbital periods of the Kepler EB systems.

### 2.2.2 TESS

The Transiting Exoplanet Survey Satellite (TESS) is a space telescope that was sent on a two-year NASA mission led by Massachusetts Institute of Technology (MIT) with goals of discovering transiting exoplanets using the first spaceborne all-sky transit survey. It was launched on the 18th of April 2018 into a highly elliptical 13.7-day orbit around the Earth. On the 5th of April 2021, TESS had identified 2,601 candidate exoplanets, with 122 that have been confirmed. Although the prime mission has ended, TESS continues to acquire additional data on an extended mission until at least 2025.

During TESS's prime mission approximately 200,000 stars were to be studied, with a focus on nearby main-sequence dwarf stars of types F5 to M5, with apparent

magnitudes brighter than 12 mag (Ricker et al. 2015). Depending on each star's ecliptic latitude, they were to be observed for a span of a month to a year. Brightness measurements were to be taken every 2 minutes of preselected target stars, with full frame images taken every 30 minutes (Ricker et al. 2015).

TESS's instrumentation comprises of four wide-field-of-view optical CCD cameras, with each camera covering a field-of-view of $24° \times 24°$ with a wavelength range of $600 - 1000$ nm, together giving a combined field-of-view of $24° \times 96°$ (Ricker et al. 2015). Each camera has four low-noise 4-megapixel CCDs that are arranged in a 2x2 detector array, giving a total of 16 megapixels per camera.

TESS data have been used in this project as TESS has observed the same area of the sky that has been surveyed by MOSES. Some of the EBs found in this project have also been detected in the TESS data, allowing comparisons between the results from MOSES versus TESS for this subcategory of EB stars. The TESS data are space-based, whereas the MOSES data are ground-based, meaning that we expect the TESS results to be of a higher quality. This gives a good baseline to compare the MOSES results to in order to see how accurate they are.

### 2.2.3  Gaia

Gaia is a space observatory that was launched on the 19th of December 2013 into orbit around the L2 Lagrange point by the European Space Agency (ESA) where its aim is to make the largest and most precise 3D map of approximately a billion stars in our galaxy (Brown et al. 2018). To date the mission has released two data releases known as DR1 and DR2 and an early data release 3 (EDR3), with the third full data release expected sometime in 2022. The spacecraft was originally sent on a 5-year mission, but this was extended to the 31st of December 2022 with an indicative further extension to December 2025.

Gaia observes and processes stars in the range of 3-20 mag and raw data for

targets brighter than 3 mags are also downloaded for later processing (Martín-Fleitas et al. 2014). The first data release contains the positions and magnitudes for 1.1 billion stars and parallaxes and proper motions for more than 2 million of these (Lindegren et al. 2016). The second data release builds on this with positions and magnitudes of 300 million stars and positions, parallaxes, and proper motions of approximately 1.3 billion stars (Lindegren et al. 2018).

Gaia contains three main instruments which are an astrometry instrument, a photometric instrument, and a radial-velocity spectrometer. The astrometry instrument measures the angular position of stars to determine their positions and allows the parallax, distance, and proper motion to be determined by combining the observations that are taken over the duration of the mission. The photometric instrument covers the wavelength range 320 nm - 1000 nm to record luminosity measurements of the stars (Brown et al. 2018). It contains blue and red photometers which allow determination of temperatures, composition, mass, and age. The radial-velocity spectrometer measures the Doppler shift of absorption lines in medium resolution spectral data to determine the velocity of astronomical objects.

Gaia observes each of its targets around 70 times which allows the brightness and position of each target to be studied over time. This allows objects such as different types of variables stars, exoplanets, and asteroids to be discovered, including eclipsing binary stars. The positional data for the eclipsing binary stars found in this project and all of the other objects found by the MOSES survey were cross-refenced with the Gaia archive in order to use the parallaxes found by Gaia to calculate distances to the EBs, and thus allow an HR diagram to be made.

## 2.3   Key Results from Recent Eclipsing Binary Star Research

Due to the usefulness of eclipsing binaries in deriving star parameters and in testing stellar evolution theories, they have been the subject of many research papers. A short

summary of some of the recent research in the field is provided henceforth.

In 2005, Southworth et al. showed the promise of using EBs to estimate the distance to stellar clusters when they analysed HD 23642, an A-type detached eclipsing binary belonging to the Pleiades cluster, and estimated the distance to it to be $139 \pm 4$ pc from the use of surface brightness-effective temperature relations (Southworth et al. 2005a, Kervella et al. 2004). They also analysed WW Aurigae and derived the masses of the two stars to an accuracy of 0.4% by cross-correlating the observed spectra against standard star spectra to obtain a radial velocity curve (Southworth et al. 2005b). The radii were derived to accuracies of 0.6% by analysing UBV and uvby light curves with the EBOP code (Eclipsing Binary Orbit Program; (Southworth et al. 2005b)).

The detached eclipsing binary V20 in the open cluster NGC 6791 was analysed by Grundahl et al. in 2008. They were able to derive precise mass and radius measurements for both the component stars to an accuracy of approximately 0.6% and 1.0% respectively (Grundahl et al. 2008). The distance to the cluster was also determined to be 4000 pc with an error of 5%, and they were able to derive the age of the cluster with an uncertainty of just 0.5 Gyr (Grundahl et al. 2008). This showed that the dominant error in deriving the age of the cluster was no longer in the observational errors, but due to the difference in stellar models.

The analysis of eclipsing binaries has also been used to determine the distances to nearby galaxies. In 2010, the distance to the Andromeda galaxy (M31) was determined by analysis of an EBs light curve, radial velocity curve and spectra to find the masses, radii and temperatures of its component stars. The distance to the binary was then found to be $744 \pm 33$ kpc, which is in agreement with other distance determinations for the galaxy (Vilardell et al. 2010). With an error of only 4% this further shows how the analysis of EBs can be used as a robust way to derive cosmic distances.

On a larger scale, several space telescopes such as Kepler, TESS, and Gaia have recorded high quality data for many EBs, as mentioned in the previous section. For

example, the Kepler Space Telescope catalogued 1,879 unique eclipsing binary objects during its first 44 days of observation, finding a 1.2% occurrence rate for eclipsing binaries across its field (Prša et al. 2011a). Transit Planet Search (TPS) identified most EBs with periodic signals with durations from a few hours to half a day. They also used morphological classification of each light curves power spectrum to identify potential EBs. The periodograms for the EBs found were computed using three methods, Analysis of Variance, Lomb-Scargle, and Box-fitting Least Squares, the latter two have been investigated as possible methods to be used in this project (see Section 4). Preliminary manual classification of EBs found yielded 52.3% detached systems, 7.5% semi-detached systems, 25.4% overcontact systems, 7.5% ellipsoidal variables, and 7.3% uncertain types (Prša et al. 2011a). Principal parameters including temperature and mass ratios were also found for the EBs analysed.

These studies demonstrate some of the methods used to analyse EB type systems, as well as the usefulness of studying EBs in order to accurately derive stellar parameters and cosmic distances.

## 2.4 Analysing Eclipsing Binaries

Using photometric observations allows some relative parameters of EB systems to be derived. Using the phase folded light curve of an EB, the depths of minima can be compared to find the ratio of the temperatures between the two components since the flux of the system is related to the temperature as shown in Equation 1.

$$F_e \propto T^4 \tag{1}$$

In the equation $F_e$ is the effective flux of the system and $T$ is the temperature of the system. If we assume that the smaller radius star is the hotter star, then the flux outside of eclipse is related to the temperature and radii of the component stars as shown in

Equation 2.

$$F_0 \propto r_l^2 T_l^4 + r_s^2 T_s^4 \tag{2}$$

In Equation 2, $F_0$ is the flux outside of eclipse, $r_l$ and $r_s$ are the radii of the larger and smaller radii component stars, and $T_l$ and $T_s$ are the temperatures of the larger and smaller radii component stars respectively. For the primary eclipse (deeper minimum) the parameters are related as shown in Equation 3, and for the secondary eclipse (shallower minimum) they are related as shown in Equation 4.

$$F_{prim} \propto r_l^2 T_l^4 \tag{3}$$

$$F_{sec} \propto (r_l^2 - r_s^2) T_l^4 + r_s^2 T_s^4 \tag{4}$$

In these equations $F_{prim}$ and $F_{sec}$ are the flux at the maximum eclipse depth during the primary and secondary eclipse respectively. These equations can be used to derive an expression for the temperature ratio between the components using the flux outside of eclipse, and the flux at maximum depth of each of the eclipses, as shown in Equation 5.

$$\left(\frac{T_s}{T_l}\right)^4 = \frac{F_0 - F_{prim}}{F_0 - F_{sec}} \tag{5}$$

If we assume that the larger radius star is hotter, then the temperatures in the brackets on the left-hand side of the equation are flipped.

The relative diameters of the system can also be derived in terms of the orbital separation of the system by using Equations 6 and 7.

$$\frac{t_4 - t_1}{P} = \frac{D_1 + D_2}{2\pi R} \tag{6}$$

$$\frac{t_3 - t_2}{P} = \frac{D_1 - D_2}{2\pi R} \tag{7}$$

In the equations above, $t_1$ and $t_4$ are the ingress and egress times of the eclipse respectively,

$t_2$ and $t_3$ are the times when maximum eclipse depth starts and ends, $P$ is the period of the system, $D_1$ and $D_2$ are the diameters of the two component stars, and $R$ is the orbital separation of the system. These equations assume an inclination angle of 90°, when the stars pass across the centre of each other with respect to the observer and form flat bottom eclipses. It is the secondary eclipse in the phase-folded light curve, when the smaller radius star passes in front of the larger radius star, which gives the information required for the equations. The slopes of the eclipse minima give information on the radius of the smaller star, and the duration of the flat bottom of the minima gives information on the radius of the larger star.

In order to calculate the distances to the EB systems using the parallaxes found from Gaia, Equation 8 can be used.

$$d = \frac{1}{p} \tag{8}$$

In the equation, $d$ is the distance to the system in parsecs and $p$ is the parallax of the system in arcseconds. The distance can then be used with the apparent magnitude of the system to find its absolute magnitude using Equation 9.

$$M - m = -5\mathrm{log d} + 5 \tag{9}$$

In the equation, $M$ is the absolute magnitude, $m$ is the apparent magnitude, and $d$ is the distance to the system in parsecs.

# 3   MOSES Archive

## 3.1   The MOSES Project

This project makes use of data from the MOSES project (Rambukwella-Gill 2019). The MOSES project was run over 180 days in 2018-2019 at the University of Central Lancashire. The aim of the survey was to observe sources of stellar variability, including transiting exoplanets, in a certain area of the sky. It was centred around R.A: 2h 18m 17s and Dec: 63° 30' 44" (Rambukwella-Gill 2019). The survey was arranged as a 4 x 4 mosaic centred on the chosen field, with 16 images being observed in sequence and given mosaic coordinates. Each image had an observing time of 60 seconds, which allowed for photometry of objects with a visual magnitude between 11.5 and 17 mag (Rambukwella-Gill 2019). Each image is 40 x 40 arcmins, with the full FOV of the mosaic being 7 square degrees. The survey observed 87,397 unique objects in the field, with 29,399 objects having over 200 measurements. There were two known variables detected within the field: RAFGUL 3155 and TYC 4037-209-1. Initial analysis of the data by Rambukwella-Gill (2019) found 719 variable objects in the field. Visual examination of those objects determined that 60% of them display genuine variability, with the remaining 40% of apparent variables being due to problems with the photometric pipeline. At least 5 eclipsing binary systems were found during initial analysis (Rambukwella-Gill 2019).

## 3.2   MOSES Project Hardware

### 3.2.1   MHT

The Moses Holden Telescope (MHT), from which the data in this project is obtained, is located at Alston Observatory (+55.80°N, -2.59°W) and is a Planewave CDK700 telescope using an alt-az mount. It has a 0.7 m primary mirror with an 83% effective collecting area, 0.29 m secondary mirror, and a tertiary flat mirror to reflect light to the eyepiece or CCD.

The typical seeing at Alston Observatory is 3 arcsec. The MHT and CCD was operated in the 2x2 binning mode and has a pixel scale of 1.18 arcsec/pixel. The alt-az mount that the MHT uses has a pointing accuracy of 2 arcseconds, with a tracking accuracy of <1 arcsecond over a 10-minute period, and field de-rotation accuracy of 3 microns of peak-to-peak error at 35 mm off-axis over 1 hour of tracking (18 arcsec) (*Planewave Instrument, CDK700* 2020).

### 3.2.2 CCD and Filter Set

The CCD used by the MHT is the Apogee Aspen CG16m CCD. It has a 16.8 Megapixel sensor with 16-Bit digitisation consisting of 4096 x 4096 pixels, each measuring 9 µm in size. The MHT has a native plate scale of 45 $\text{arcsec}\,\text{mm}^{-1}$. The MHT uses the Johnson-Cousins filter set, which consists of U, B, V, R, and I filters. The observations analysed in this project used the V band, with a central wavelength of 545 nm (Karttunen et al. 2007).

# 4 Comparison of Period Finding Methods

In order to classify the variable stars from the MOSES archive, the period of each variable system must be found. There are several methods that could be used to achieve this but given that the data being used in this project are ground based with sparsely sampled light curves this makes period finding more difficult (Dongen et al. 1999). Several of the methods available were thus tested using high quality data first. Kepler data for a known EB (KIC5534702) were used initially, then the same Kepler data that had been modified to replicate ground-based observations, and finally two EBs from the MOSES survey that were recognised as EBs after preliminary analysis. The phase folded light curve for the Kepler data used (KIC5534702) can be seen in Figure 9. In this project, Python was used as the programming language throughout.
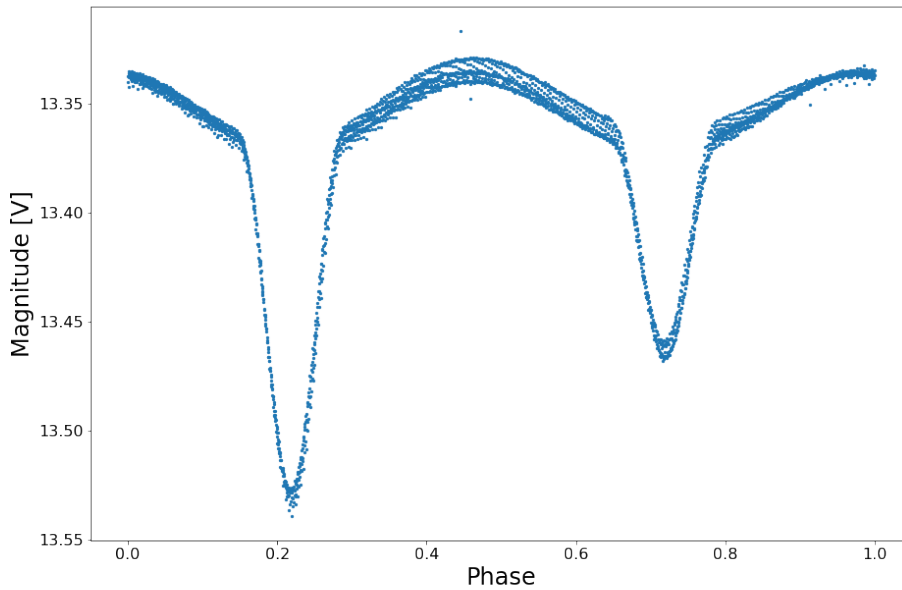


**Figure 9:** The phase folded light curve of KIC5534702. This EB has a period of 1.025 days. (Kirk et al. 2016)

The known EBs from the MOSES survey were systems MHT 3799 and MHT 5720, both of which were found during some preliminary analysis of the data by Rambukwella-Gill (2019). The phase folded light curves for these can be found in Figures 10 and 11 respectively.

The modified Kepler light curve was made by removing two thirds of the data points periodically to replicate an 8-hour observing night with a ground-based telescope. Some randomly chosen sections were also removed from the data to further reduce the number of data points, to make the light curve comparable to the datasets collected during the MOSES survey.
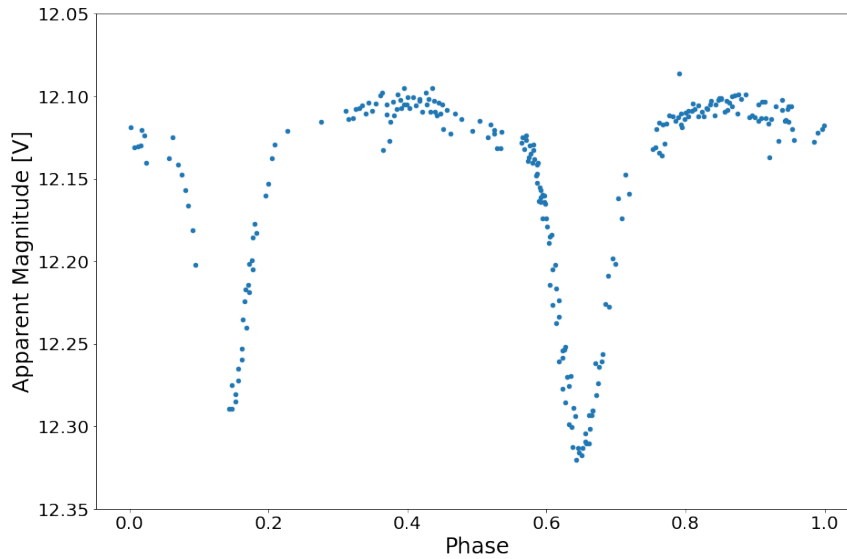


**Figure 10:** The phase folded light curve of MHT 3799 from the MOSES archive. This EB has a period of 3.68 days. (Rambukwella-Gill 2019)

When testing the different period finding methods using the different Kepler datasets the search step size was kept the same throughout at a value of 0.01 days. This step size was chosen to allow fast computation as smaller steps would result in longer computation times. This step size is also small enough for accurate periods to be determined from the data if the period finding method is capable of doing so from the data provided. The period range chosen for analysis of the Kepler light curves was kept to 0-4 days since the true period of the system was known to fall in this range, and also allowed any harmonics close to the true period to be found. This small range also kept computational times down.

When testing using the known EBs from the MOSES survey the step size was kept the same as when testing using the Kepler datasets, and the period range used was
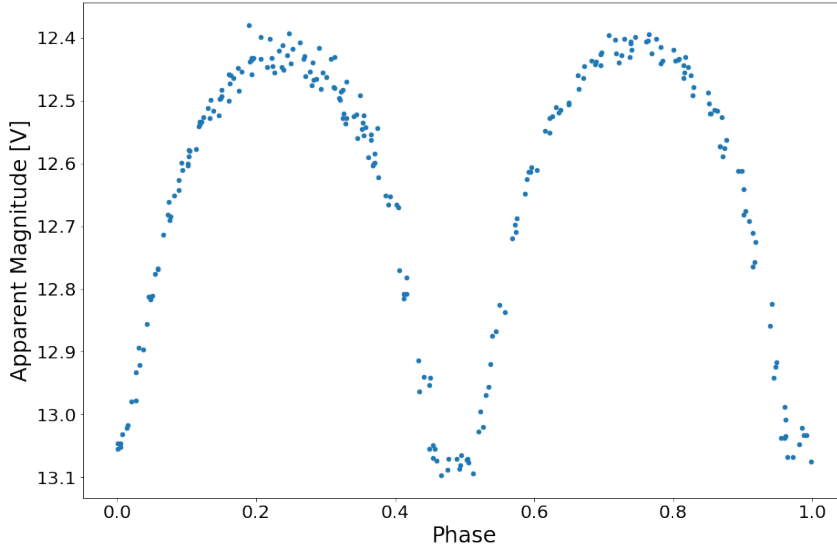
24



**Figure 11:** The phase folded light curve of MHT 5720 from the MOSES archive. This EB has a period of 0.39 days. (Rambukwella-Gill 2019)

kept to 0-8 days for MHT 3799 and 0-2 days for MHT 5720 since the known periods of the systems fell into these ranges and also covered possible harmonics close to the true period.

The main features of the different period finding methods being investigated were their ability to find the periods of the variable stars from unevenly sampled time-series data, and the speed at which they could accurately perform this task.

## 4.1 Box Least Squares (BLS) Fitting

BLS fitting is a box fitting algorithm that involves fitting a model to the photometric time series data at each candidate period and searching for a periodic change between two distinct levels (i.e two different magnitudes) (VanderPlas 2018, Kovács et al. 2002). Astropy's BoxLeastSquares program was used for the testing of this method. It outputs a power spectrum where the peaks on the graphs indicate the periods where repeating patterns have been found. The largest peak on the graph indicates where the program thinks the true period is. Astropy's BoxLeastSquares software allows the user to select

a range to search for periodicity within and the step size at which periodicity is sampled for within these limits

BLS found a harmonic of the period of the full Kepler light curve at one quarter of the true period. It found it using a step of 0.01 days and a range of 0-4 days, as can be seen in Figure 12. It also found one quarter of the period of the Kepler data that was modified to look like a ground-based observation, as seen in Figure 13. However, when this method was tested using a known EB from the MOSES survey it was unable to find even a harmonic of the period, as seen in Figure 14.
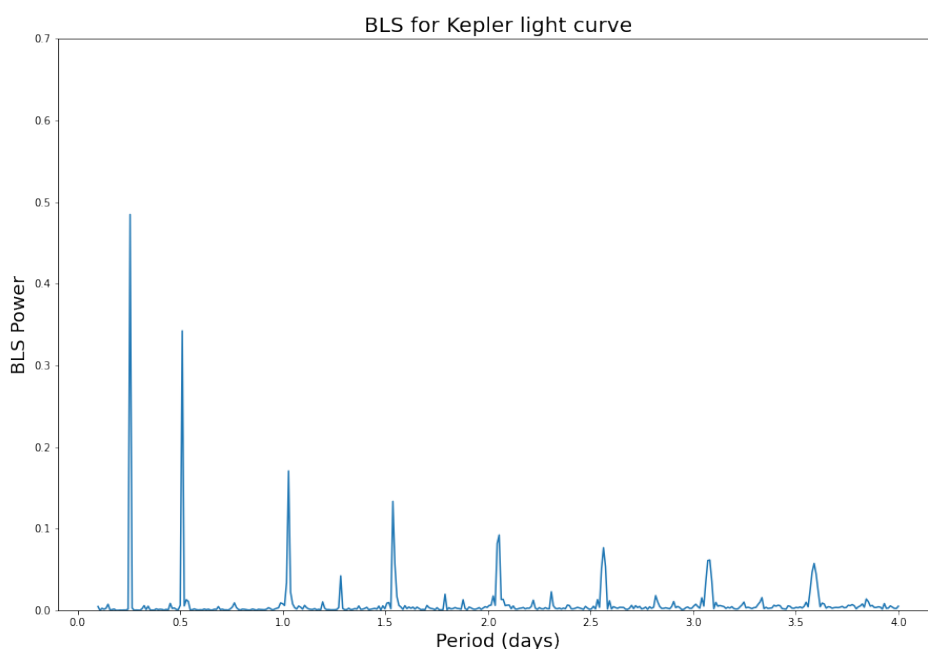


**Figure 12:** BLS power spectrum for Kepler light curve KIC5534702. The peaks on the graph indicate where the period of the system has been found, with stronger peaks indicating the more likely periods. The true period of the system is 1.025 days, whereas BLS found the period to be a quarter of that at approximately 0.25 days.
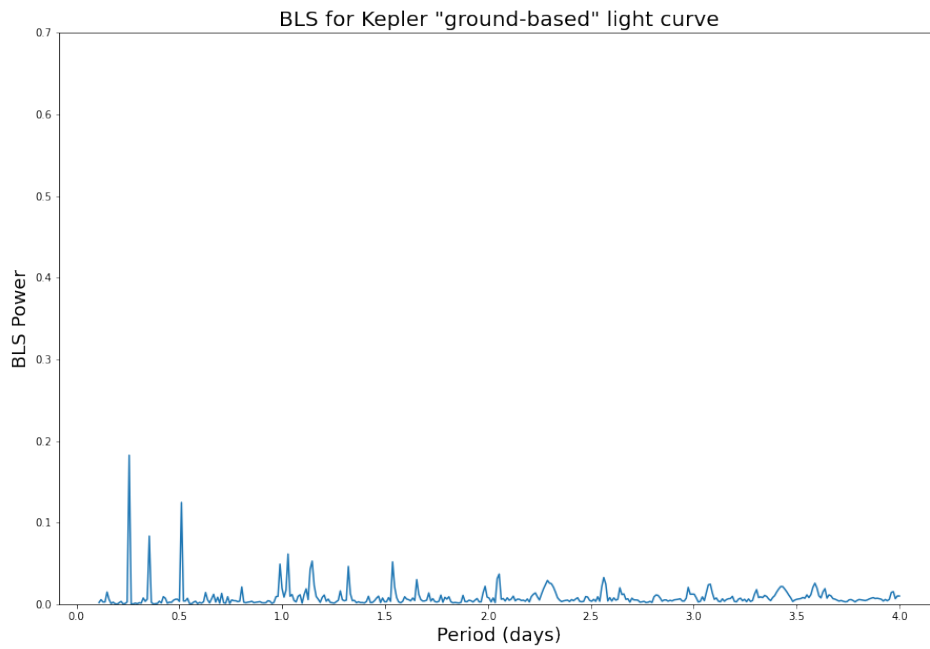
**Figure 13:** BLS power spectrum for Kepler light curve KIC5534702 that was modified to look like it was taken using a ground-based telescope. The true period of the system is 1.025 days, whereas BLS found the period to again be a quarter of that at approximately 0.25 days.
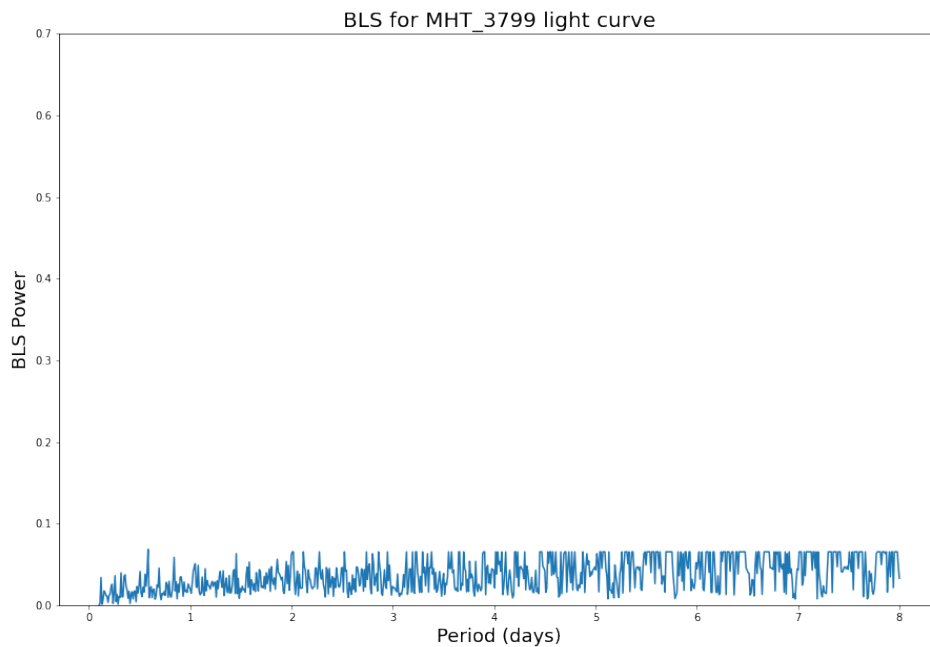


**Figure 14:** BLS power spectrum for MOSES survey light curve MHT 3799. The true period of the system is 3.68 days, however BLS was unable to find even a harmonic of the system.

## 4.2   Lomb-Scargle Periodogram

Lomb-Scargle is an algorithm used for detecting periodic signals in unevenly sampled time-series data (VanderPlas 2018). It efficiently computes a Fourier-like power spectrum, which allows the best candidate period of variability to be determined from the data (VanderPlas 2018). PyAstronomy's LombScargle program was used in the testing of this method. Like BLS, this Lomb-Scargle program outputs a power spectrum, where the largest peak on the graph indicates where the program thinks the true period is. PyAstronomy's LombScargle software again allows the user to set a range over which to search for periodicity and the step size at which periodicity is sampled for in this range.

It can be seen in Figure 15 that this method was able to find half the period of a full Kepler light curve using a step of 0.01 days. For the modified Kepler data this method was able to find a period close to but slightly higher than the true period, with a value of 1.15 days, as shown in Figure 16. When Lomb-Scargle was tested with MHT data for the known MOSES survey EB MHT 3799 it was unable to find even a harmonic of the true period, as can be seen in Figure 17.
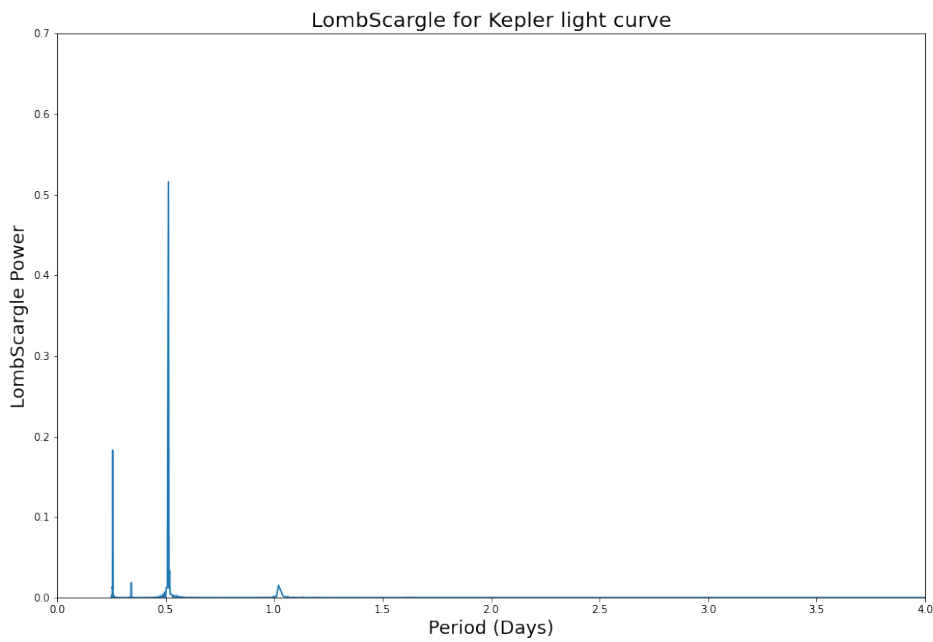
28



**Figure 15:** Lomb-Scargle power spectrum for Kepler light curve KIC5534702. The peaks on the graph indicate where the period of the system has been found, with stronger peaks indicating the more likely period. The true period of the system is 1.025 days which Lomb-Scargle found half of, as indicated by the largest peak on the graph.
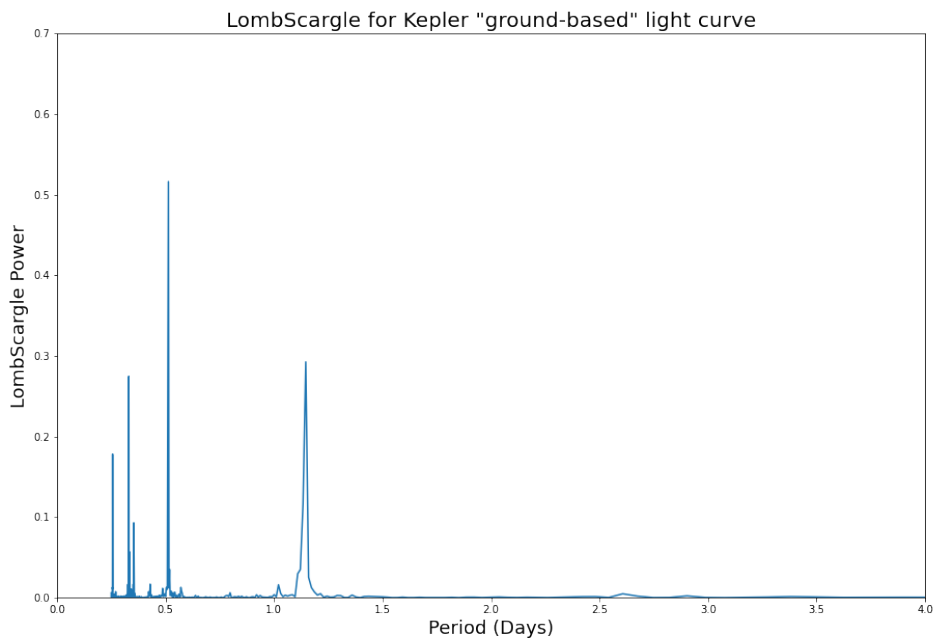


**Figure 16:** Lomb-Scargle power spectrum for Kepler light curve KIC5534702 that was modified to look like it was taken using a ground-based telescope. The true period of the system is 1.025 days, whereas Lomb-Scargle found the period to be slightly higher at 1.15 days.
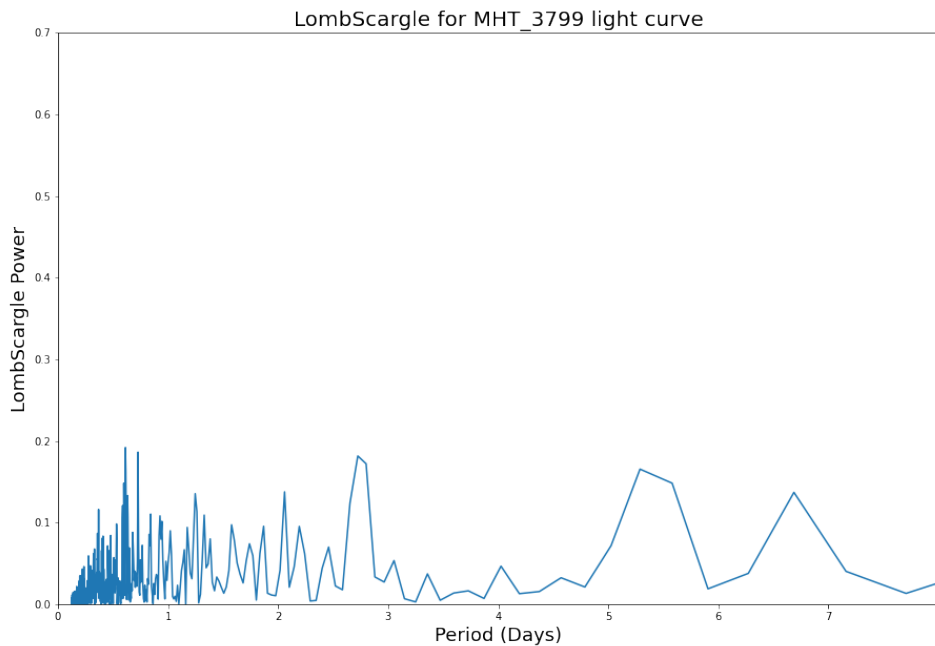
**Figure 17:** Lomb-Scargle power spectrum for MOSES survey light curve MHT 3799. The true period of the system is 3.68 days and Lomb-Scargle was unable to find even a harmonic of the true period.

## 4.3 Phase Dispersion Minimisation (PDM)

PDM is a phase-folding method which uses a similar method to the least-squares fitting technique to find the best fit period (Stellingwerf 1978). It folds observations as a function of phase using a trial period and splits the folded data into several bins and calculates the variance of the amplitude within each bin. The overall variance is calculated using the sum of the variance of the bins, with a bin variance to total variance ratio close to zero indicating a good fit period, and a ratio close to unity indicating a false period. The data are folded using each test period and the period with the lowest ratio indicates the true period. PDM is useful for analysis of unevenly spaced time-series data and non-sinusoidal variation.

To test this method, PyAstronomy's version of PDM was used at first. PyAstronomy's PDM software allows the user to select a range over which to search for peri-

odicity and the step size at which periodicity is checked for within these limits. It also allows the number of bins used to be changed which can help average the observation errors in larger datasets. PDM outputs a theta value for test periods which can be plotted against period to give a graph similar to the power spectra seen previously in this section. In this case, lower theta values indicate a better candidate period.

For the testing of this method, the same steps and ranges were used as before, and the number of bins were set to 7. Using these parameters, the method was able to find one and a half times the periods for the full Kepler light curve, as seen in Figure 18, and the same for the modified Kepler data, as seen in Figure 19. It can be seen in Figure 20 that it was unable to find even a harmonic of the period for the known MOSES survey EB MHT 3799.
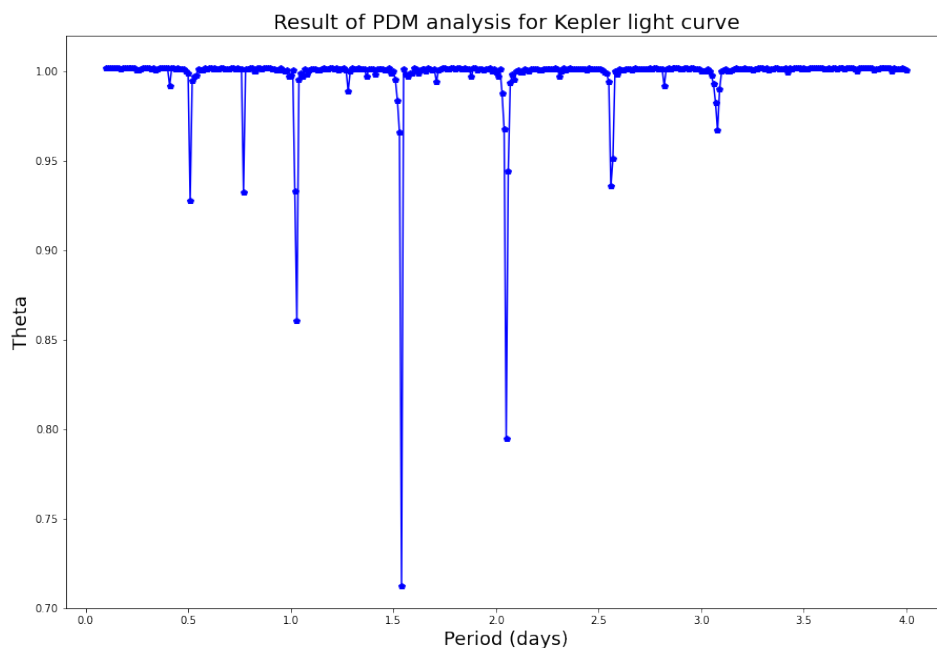


**Figure 18:** Result of pyPDM analysis for Kepler light curve KIC5534702 using 7 bins. The lower theta value dips on the graph indicate where the period of the system has been found, with lower dips indicating the more likely periods. The true period of the system is 1.025 days, and pyPDM found one and a half times this value.
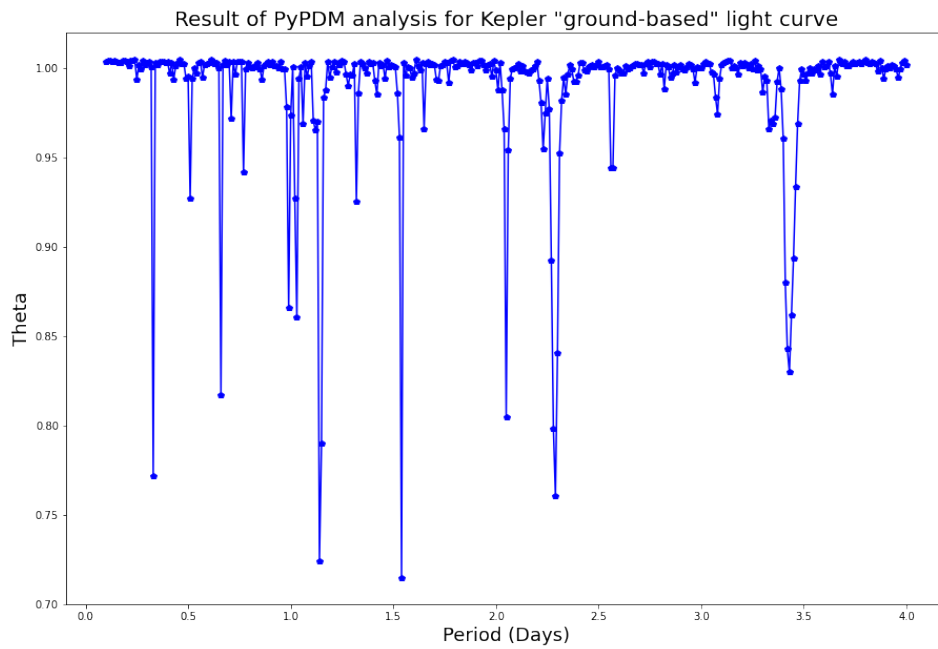
**Figure 19:** Result of pyPDM analysis using 7 bins for Kepler light curve KIC5534702 which has been modified to imitate ground-based observations. The true period of the system is 1.025 days, and pyPDM found one and a half times this value.
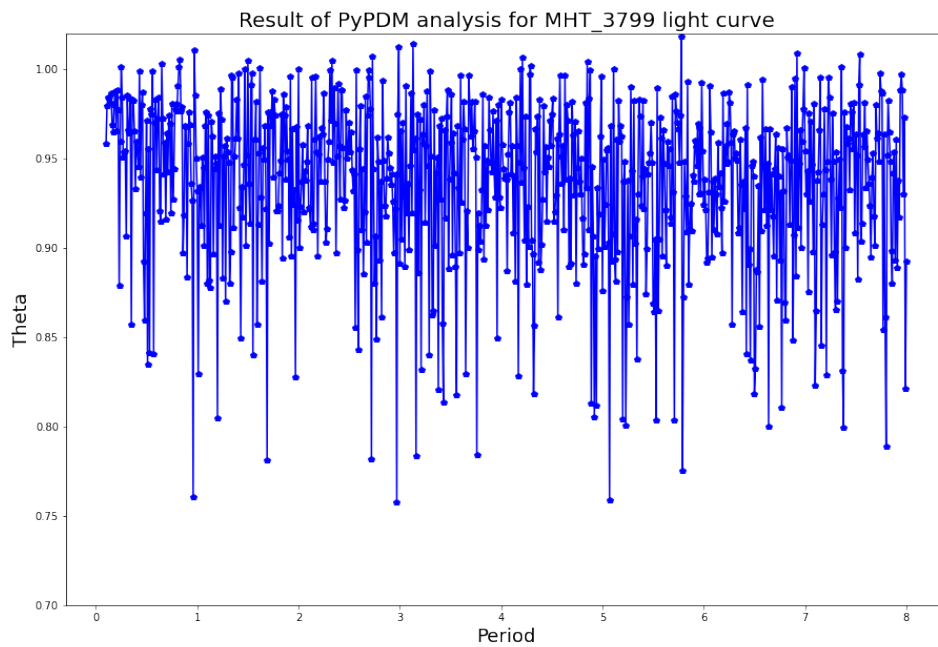


**Figure 20:** Result of pyPDM analysis for MOSES survey light curve MHT 3799 using 7 bins. The true period of the system is 3.68 days, which pyPDM was unable to find.

Although this method was similar in success rate to the other methods tested, this method was well described in Stellingwerf (1978) and upon inspection it was decided that it could be easily manipulated to work better for the data being used. As the variability of the stars from the MOSES survey are unknown, a wide range with a small step must be set, leading to a long computational time using any of the methods that were tested. Thus, it was decided that a more suitable version of PDM that worked faster and more accurately for the data from the MHT would be written.

The method and equations PDM uses are detailed in Stellingwerf (1978) and using this information a new version of PDM was written. The first change was made to the binning of the data. Stellingwerf uses sliding bin covers to improve phase coverage, however after testing pyPDM with and without bin covers using MOSES data it was found that this did not improve the results a significant amount and increased the computational time considerably. Thus, fixed width bins with no sliding covers were used in the new version of PDM.

Another change that was made was in the sampling of trial periods. As the MOSES survey was 180 days in length, a 120 day range is required in order to ensure 1.5 cycles of each light curve are available to confirm the variability of each EB. PyPDM allows you to set the range and step size to search over, but to search over a 120 day range at a 0.01 day step (12,000 trial periods) takes approximately 6 minutes per light curve. To reduce the number of trial periods to be tested an adaptive step size was used in the new version of PDM. It first used a broad step of 0.1 days during the first pass search for periodicity over a 120 day range (1,200 trial periods). The best period found using this first pass and a list of 10 harmonics (5 either side) were then used to search over a smaller range of 0.2 days around these periods at a step of 0.01 days (220 trial periods). The candidate period with the lowest theta value was then deduced to be the best fit period for the data. This gave a period precise to 2 decimal places with an error of 0.02 days. By reducing the number of trial periods from 12,000 to 1,420 the computation time was reduced from ~6 minutes per light curve to ~20 seconds per light curve. With 697

variable objects to run through the code, this reduced the overall computation time from ~70 hours to ~4 hours. By checking the harmonics of the best fit period from the first pass search during the second pass search, the accuracy of the PDM code for the data from the MOSES survey also increased, and it was less likely to pick out a harmonic of the period as the true period.

This new version of PDM was very quick and was able to find the true period for the full Kepler light curve that was tested. In Figure 21 the first pass results of PDM analysis can be seen where it appears that a period of just over 1.5 days is the true period, but the PDM code reanalysed at a step of 0.01 days and a range of 0.2 days around the harmonics seen on the graph. This resulted in the true period being output as the best candidate period. The modified Kepler data was analysed as can be seen in Figure 22 and half the true period was found during the first pass. The harmonics were then analysed and again the true period was found to be the best candidate period.
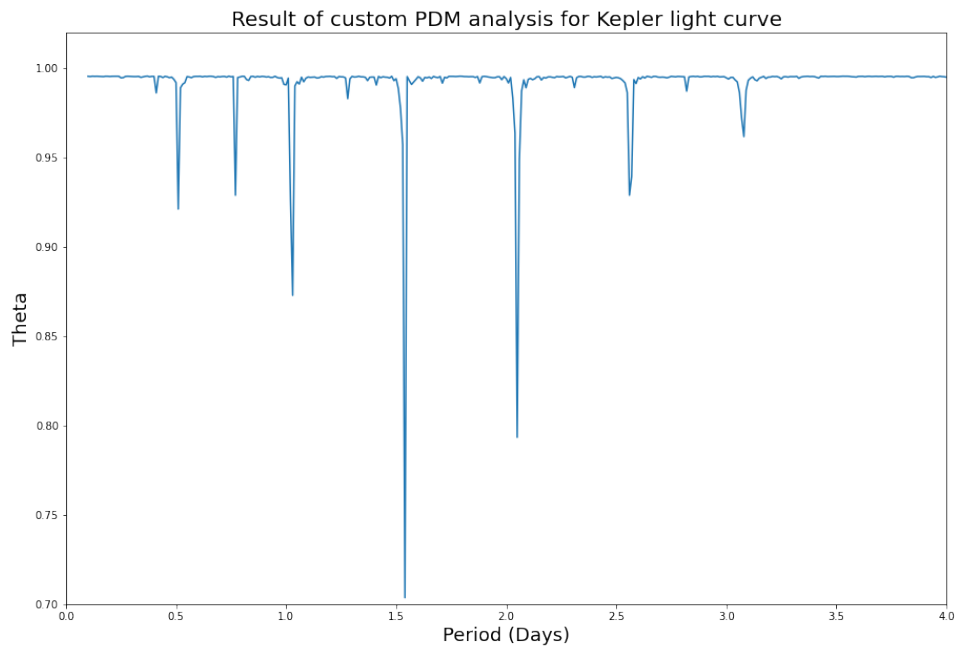
**Figure 21:** Result of the first pass of custom PDM analysis for Kepler light curve KIC5534702 using 7 bins. The lower theta value dips on the graph indicate where the period of the system has been found, with lower dips indicating the more likely periods. The true period of the system is 1.025 days, which the first pass of custom PDM was able to find a harmonic for at one and a half times the period. After analysis of the harmonics the period was found to be the true period.
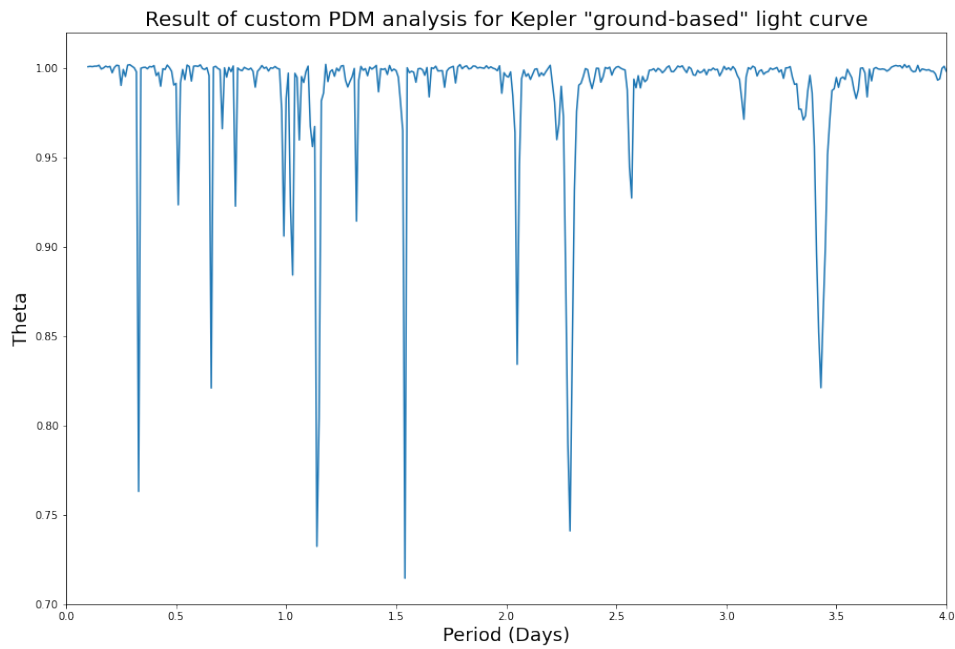
**Figure 22:** Result of the first pass of custom PDM analysis for Kepler light curve KIC5534702 which has been modified to imitate a ground-based observation using 7 bins. The true period of the system is 1.025 days, which the first pass of custom PDM was able to find a harmonic for at one and a half times the period. After analysis of the harmonics the period was found to be the true period.

Figure 23 shows that during the custom PDM's first pass it was also able to find half the true period for the known MOSES survey EB MHT 3799. After analysis of the harmonics the best candidate period was still found to be half the true period. This method was then tested with another known EB from the MOSES survey (MHT 5720) and it was able to find the true period of the system on its first pass, as shown in Figure 24.
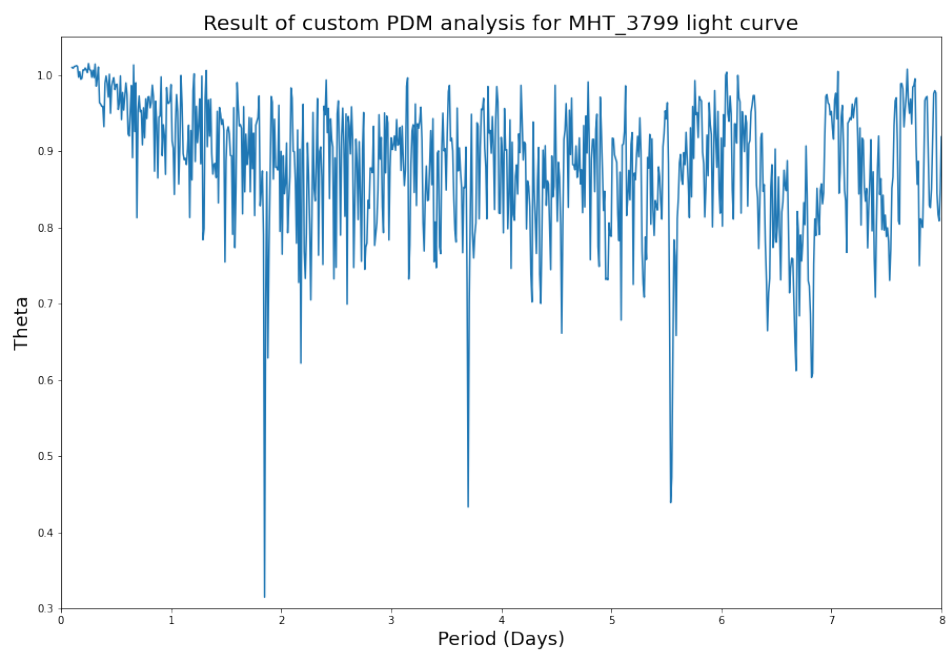
**Figure 23:** Result of the first pass of custom PDM analysis for MOSES survey light curve MHT 3799 using 7 bins. The true period of the system is 3.68 days, which the first pass of custom PDM was able to find a harmonic of at half the period. After analysis of the harmonics the period was again found to be half the true period.
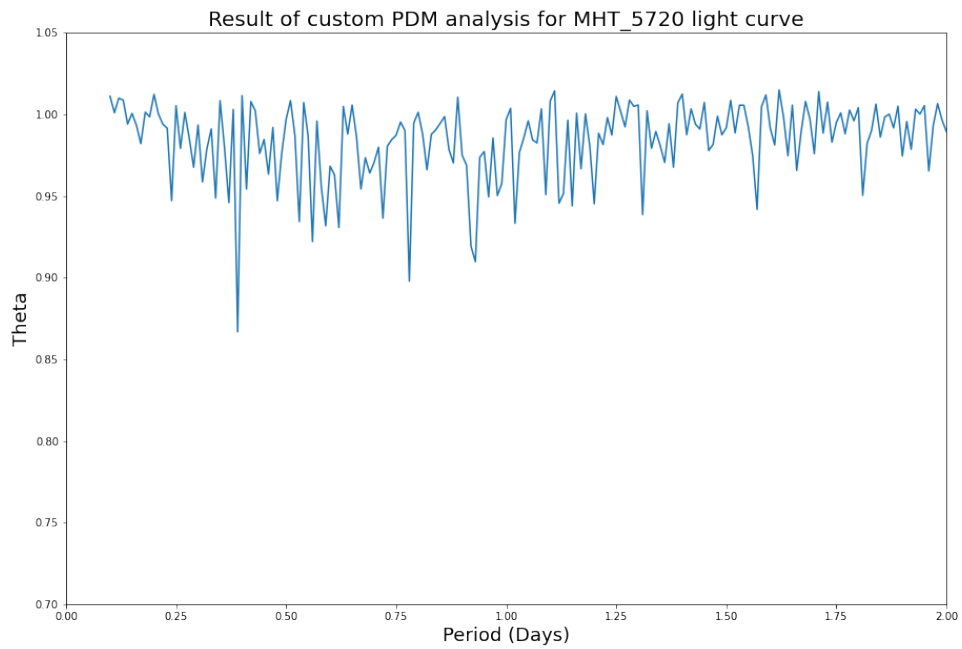
**Figure 24:** Result of the first pass of custom PDM analysis for MOSES survey light curve MHT 5720 using 7 bins. The true period of the system is 0.39 days which the custom PDM was able to find successfully on its first pass.

Although the custom PDM that was written still sometimes found a harmonic of the system as the best fit period, it performed much better than any of the previously tested methods. Most notably, the custom PDM was able to find a harmonic for one of the MOSES datasets and the true period for another, whereas all of the previously tested methods were unable to find even a harmonic for these datasets. Due to the fast computation speed of the custom PDM and its ability to find the periods of the variable stars from unevenly spaced time-series data to an adequate degree of accuracy, it was this method that was used to find the periods of the EBs in this project.

# 5 Analysing the MOSES Data

## 5.1 Data Cut

In order to analyse the variable stars in the MOSES data, the light curve data must be classified into groups of variable and non-variable stars. The first step in doing this was to remove any data sets for stars that could not be used. Those with fewer than 100 data points were too sparsely sampled to be analysed. Those that had average magnitudes measured of over 17 mags were too dim to have been accurately measured by the MHTs CCD, and those with average magnitudes below 11.5 mags were too bright and may have saturated the CCD, rendering the data unreliable. The data cuts can be seen visually in Figure 25. After these data cuts the number of stars to be analysed had dropped from 87,396 to 33,038.
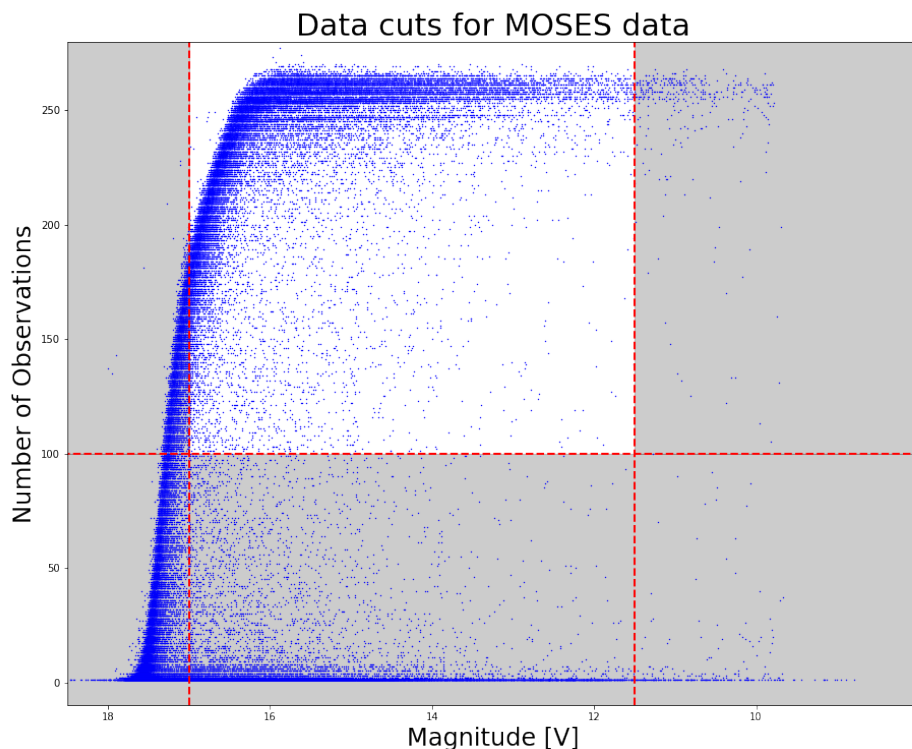


**Figure 25:** The data cuts made to the MOSES data. The greyed out areas include the datasets that were not used in analysis. The red dashed lines are where the data cuts were made, at 17 mag, 11.5 mag, and when the number of observations equals 100.

## 5.2   Finding Variable Stars

To find the variable stars in the data, each light curve was analysed for variability. Stars whose magnitude had a standard deviation of less than 0.3 were deemed to not be variable, and subsequently they were binned by average magnitude into 0.25 magnitude bins, adding the standard deviation of the star's magnitude to the appropriate bin. The median value of the standard deviation of each bin was found and is represented by the red line on Figure 26. This created a base value for each magnitude of star to compare variation to, which also considered the noise levels for each magnitude of star measured. A star was defined as variable if the standard deviation of its magnitude was equal to or greater than three times the standard deviation plus the median of the bin its average magnitude would fall into. This is represented by the green line on Figure 26, where objects that lie above this line are deemed variable (red points), and those that lie below it are non-variable (blue points). Of the 33,038 datasets for the stars in the MOSES archive, 697 of these were found to be variable stars.
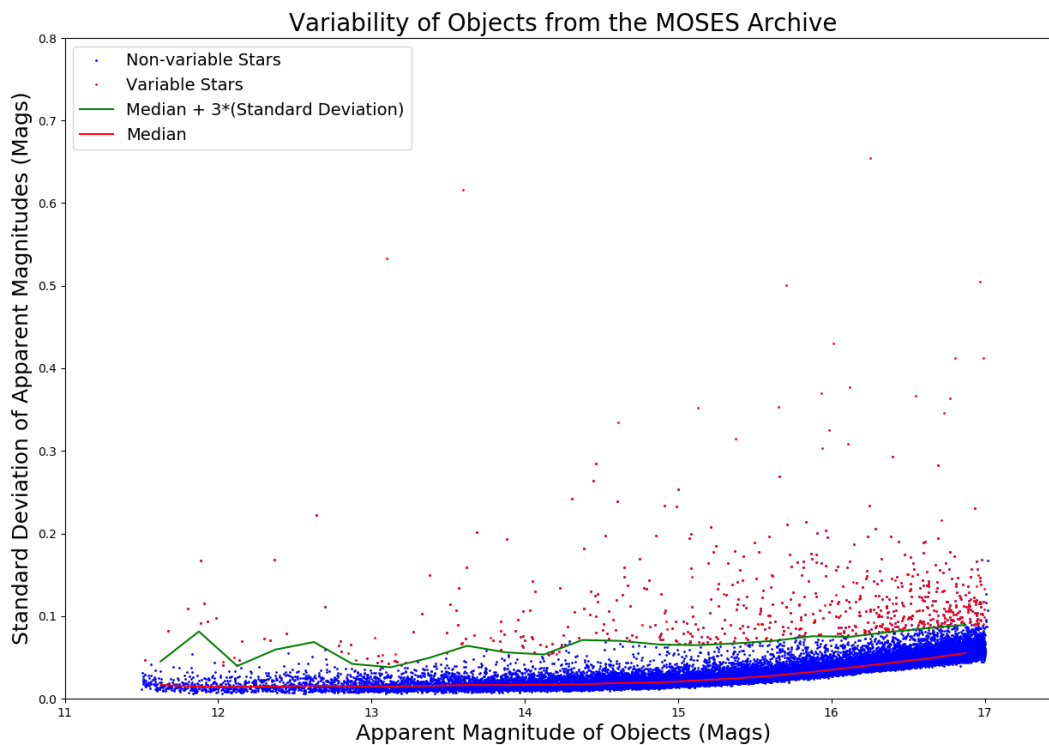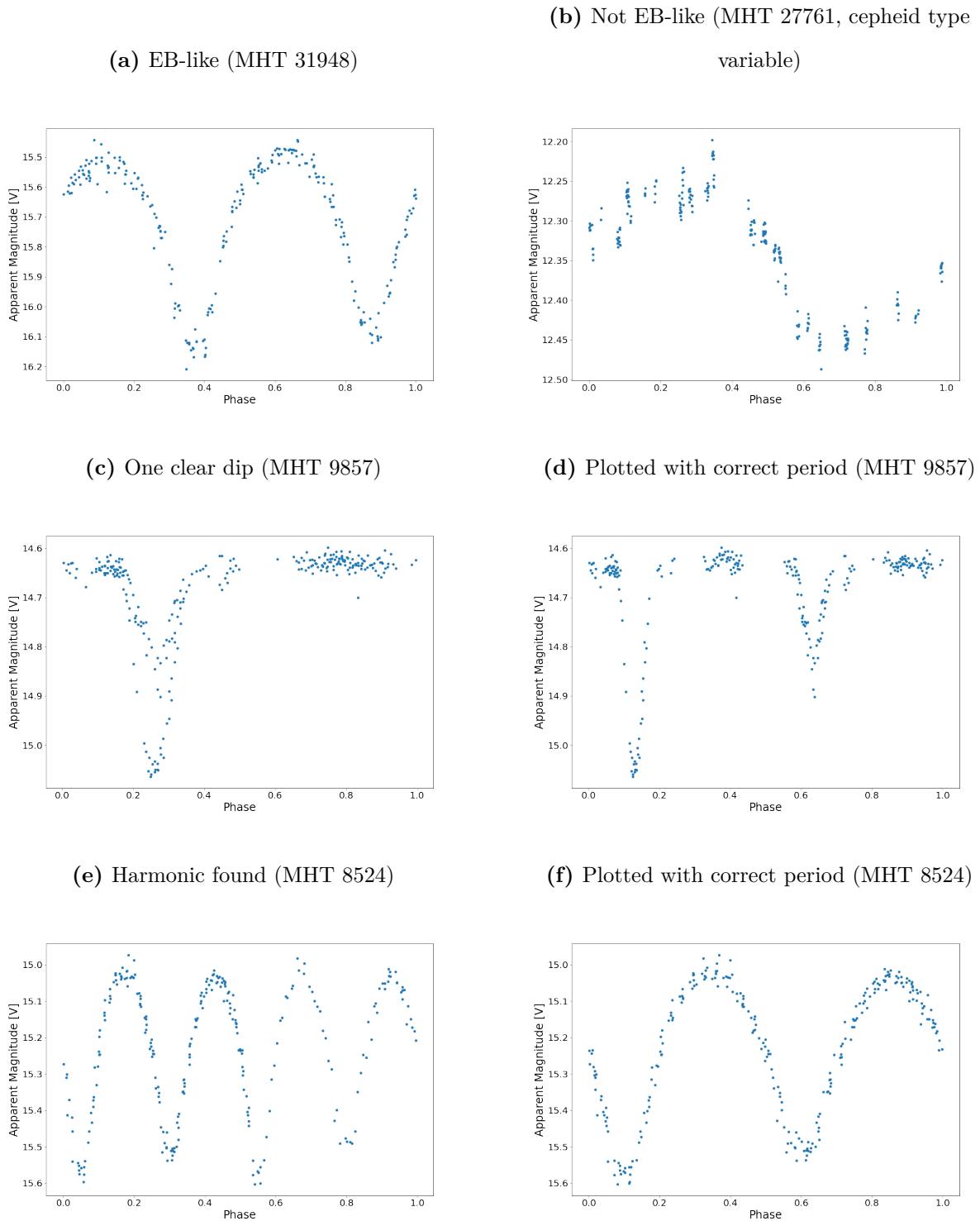
**Figure 26:** The standard deviation of the magnitude of each object plotted against its average apparent magnitude. The red line is the median standard deviation of the magnitude of the binned objects that were deemed non-variable at each magnitude, and the green line is the median plus three times the standard deviation of binned objects at that magnitude. The data were binned by average magnitude into 0.25 magnitude bins to determine these values.

## 5.3    Finding EBs

Once the variable stars had been found from the data, the next step was to find the EBs. The custom PDM code that was written was adjusted to plot the phase-folded light curve of each star system using the period found, and then to ask for a user input to decide which folder to move the star data to.

The first pass separated those systems that definitely did not have an EB-like light curve from those that could possibly be an EB. The second pass separated the systems that could possibly be EBs into four folders. The four folder categories were defined as: those which clearly showed an EB-like light curve (i.e. two clear dips), those

which showed one clear dip (could be an EB plotted using half the period), those that could be an EB but plotted with a harmonic as opposed to the true period, and those that definitely did not have an EB-like light curve. An example of the four different categories of light curve can be seen in Figure 27. In Figure 27 (a), an EB type light curve is clearly visible so this star was moved into the EB folder. The light curve for (b) in the Figure shows a sawtooth pattern, indicative of a cepheid type variable, so this star was moved into the non-EB folder. For (c) the light curve shows one clear dip, so this light curve was moved to a folder where it would be replotted using double the period found by PDM to see if the single dip could be separated into two distinct eclipses. In this case it was found that there were indeed two distinct eclipses, as shown in (d). For the light curve in (e), there is clearly an EB-like light curve plotted with a harmonic, and as such it was moved to the folder containing other EBs plotted with harmonics and replotted to give the phased light curve shown in (f).

**Figure 27:** Examples of resulting phase-folded light curves from PDM.



**(a)** EB-like (MHT 31948)

**(b)** Not EB-like (MHT 27761, cepheid type variable)

**(c)** One clear dip (MHT 9857)

**(d)** Plotted with correct period (MHT 9857)

**(e)** Harmonic found (MHT 8524)

**(f)** Plotted with correct period (MHT 8524)

The first pass on picking out the EBs was run using a range of 120 days for the periods, an initial step of 0.1 days, and 7 bins. This found 232 systems that had a light curve that showed some sort of repeating pattern with noticeable periodic drops in

magnitude. These systems were then run through the PDM code again with the same period range and bin number, but with a smaller initial step of 0.01 days, and the light curves were separated into the appropriate folders as described above. Although a smaller step size took longer to run (approximately 3 minutes per light curve), it increased the PDM code's ability to find harmonics of the period in the light curves. PDM often found half the period for the variable stars, but this could often be spotted by eye and corrected by plotting the light curve with a manually set period for the system. This allowed some of the EBs that initially only had one clear dip to be moved into the folder that contained clear EBs. After analysing all the variable stars found from the MOSES archive, this method yielded 70 systems that were determined to clearly show an EB-like light curve, 28 systems that required further analysis, and 599 that were determined to not have an EB-like light curve. A sample of the EBs found using this method along with the periods found for them using PDM are shown in Table 1. The full version of this table can be found in Appendix A.

**Table 1:** Parameters derived by PHOEBE for a subset of EBs.

| MOSES ID (MHT...) | Period ($\pm$ 0.02 Days) |
| --- | --- |
| 2707 | 1.71 |
| 3549 | 1.66 |
| 3799 | 3.70 |
| 4206 | 1.44 |
| 4708 | 0.75 |
| 5132 | 0.55 |
| 5720 | 0.39 |
| 6742 | 0.69 |
| 7687 | 0.41 |
| 7981 | 1.11 |
| ... | ... |

The coordinates of the EBs that have been found were cross-referenced with the ASAS-SN (All Sky Automated Survey for SuperNovae) Variable Stars Database (Shappee et al. 2014, Jayasinghe et al. 2018) and VSX (The International Variable Star Index)

44

(Watson et al. 2006, *AAVSO: The International Variable Star Index* 2022) to determine how many of the EBs are known in the literature. ASAS-SN can detect objects in the magnitude range of 8-18 magnitude, so covers the range of magnitude of objects detected in the MOSES survey (Shappee et al. 2014). VSX is a database that contains data for variable stars that have been collated from several catalogues (*AAVSO: The International Variable Star Index* 2022). Of the 70 systems found, 58 were found to be known EBs. These are shown in Table 2 below. This means that 12 of the EBs found are new and will be analysed for the first time in this thesis.

**Table 2:** The known EBs from the MOSES survey and their ID's

| MOSES ID (MHT...) | ID | R.A. (Deg) | Dec (Deg) |
|---|---|---|---|
| 2707 | WISE J021603.72+621730.0 | 34.01550 | 62.29167 |
| 3549 | WISE J021310.4+623841 | 33.29368 | 62.64483 |
| 3799 | WISE J021352.97+623215.5 | 33.47072 | 62.53763 |
| 4206 | WISE J021208.50+624242.7 | 33.03542 | 62.71185 |
| 4708 | WISE J022204.52+624050.2 | 35.51883 | 62.68061 |
| 5132 | WISE J022051.09+623538.7 | 35.21288 | 62.59407 |
| 5720 | WISE J021906.93+623743.8 | 34.77870 | 62.62888 |
| 6742 | WISE J022755.71+624318.9 | 36.98213 | 62.72192 |
| 7687 | WISE J022601.63+623009.5 | 36.50681 | 62.50263 |
| 7981 | WISE J021155.01+630407.0 | 32.97919 | 63.06862 |
| 8476 | WISE J021055.3+631020 | 32.73070 | 63.17241 |
| 8489 | ZTF J021055.26+632114.2 | 32.73029 | 63.35397 |
| 8490 | WISE J021048.34+630053.2 | 32.70145 | 63.01480 |
| 8524 | WISE J021048.77+630600.1 | 32.70320 | 63.10004 |
| 9550 | ZTF J020624.47+631650.2 | 31.60197 | 63.28062 |
| 9857 | WISE J020709.24+632251.9 | 31.78848 | 63.38109 |
| 10451 | WISE J020818.46+630339.9 | 32.07693 | 63.06109 |
| 10636 | ZTF J020841.32+632502.6 | 32.17219 | 63.41740 |
| 10886 | ZTF J020616.49+632114.9 | 31.56873 | 63.35416 |
| 11212 | WISE J021729.65+632141.4 | 34.37353 | 63.36149 |
| 11762 | WISE J021628.83+631608.5 | 34.12055 | 63.26884 |
| 12030 | WISE J021556.69+630807.9 | 33.98620 | 63.13554 |
| 12510 | ZTF J021505.60+630148.4 | 33.77334 | 63.03013 |
| 13617 | WISE J021418.54+630127.2 | 33.57724 | 63.02421 |
| 14747 | WISE J022215.06+632713.8 | 35.56274 | 63.45382 |
| 14758 | ZTF J022214.37+625204.2 | 35.55991 | 62.86784 |
| 15185 | WISE J022117.57+625317.5 | 35.32320 | 62.88819 |
| 15220 | ZTF J022120.00+631837.6 | 35.33334 | 63.31047 |
| 15846 | ZTF J021836.43+631001.9 | 34.65181 | 63.16721 |
| ... | ... | ... | ... |

| MOSES ID (MHT...) | ID | R.A. (Deg) | Dec (Deg) |
|---|---|---|---|
| ... | ... | ... | ... |
| 16056 | ZTF J021902.53+625843.3 | 34.76056 | 62.97871 |
| 17309 | ZTF J022850.34+632816.4 | 37.20978 | 63.47124 |
| 17580 | ZTF J022806.09+630546.7 | 37.02538 | 63.09632 |
| 19537 | WISE J021111.08+633346.9 | 32.79616 | 63.56302 |
| 20080 | WISE J021004.36+635300.7 | 32.51817 | 63.88352 |
| 20211 | WISE J020947.97+633845.6 | 32.44988 | 63.64599 |
| 20473 | ZTF J020922.66+635334.2 | 32.34445 | 63.89284 |
| 22431 | WISE J021724.47+640529.2 | 34.35197 | 64.09145 |
| 22695 | ZTF J021650.01+634453.9 | 34.20839 | 63.74833 |
| 23589 | ZTF J021241.73+634234.3 | 33.17391 | 63.70955 |
| 26689 | WISE J021922.20+633726.9 | 34.84249 | 63.62414 |
| 27033 | WISE J022009.48+633957.2 | 35.03950 | 63.66588 |
| 27293 | ZTF J022045.99+633727.5 | 35.19165 | 63.62433 |
| 28909 | WISE J022607.32+634408.1 | 36.53051 | 63.73558 |
| 28973 | WISE J022619.6+635149 | 36.58180 | 63.86370 |
| 29516 | ZTF J021143.86+643800.0 | 32.93277 | 64.63336 |
| 29705 | ZTF J021117.96+643018.2 | 32.82487 | 64.50507 |
| 30495 | WISE J020945.48+643639.6 | 32.43952 | 64.61101 |
| 31041 | ZTF J020627.37+641057.4 | 31.61406 | 64.18263 |
| 31948 | WISE J020808.2+641800 | 32.03437 | 64.30010 |
| 31956 | ZTF J020805.84+643341.9 | 32.02435 | 64.56166 |
| 32190 | ZTF J020834.31+643220.5 | 32.14296 | 64.53905 |
| 32831 | ZTF J021731.03+641028.8 | 34.37931 | 64.17469 |
| 34596 | ZTF J021427.43+642549.5 | 33.61433 | 64.43042 |
| 35564 | ZTF J022228.18+642958.0 | 35.61742 | 64.49945 |
| 35712 | WISE J022153.00+641949.9 | 35.47083 | 64.33054 |
| 39408 | ZTF J022258.27+623116.4 | 35.74283 | 62.52124 |
| 42898 | ZTF J021537.79+644051.2 | 33.90750 | 64.68090 |
| 48251 | WISE J022539.8+644939 | 36.41602 | 64.82761 |

# 6  PHOEBE

PHOEBE (PHysics Of Eclipsing BinariEs; (Prša et al. 2011b)) is a modelling package for eclipsing binary stars based on the commonly used WD program (Wilson & Devinney 1971). The underlying WD code is made up of two parts: the light curve (LC) program that computes light and radial velocity (RV) curves, and the differential corrections (DC) program that solves the inverse problem (Prša & Zwitter 2005). WD takes a more physical approach to modelling EB systems over its predecessors and allows the stars to be non-spherical by computing a discrete representation of the stellar surfaces of the components from the Roche equipotentials. Radial vectors are determined for a corresponding distribution of grid points over both stars, which allows a system of surface points to be determined (Kallrath & Milone 2009b). The WD program accounts for gravity brightening, limb darkening, and reflection effects, and is able to model stellar atmospheres.

PHOEBE builds upon the WD model with suggested improvements to the DC method and introduces proper handling of colour indices, interstellar reddening effects, and main sequence constraining. It also introduces new minimisation schemes into the solution-seeking process (Prša 2018). PHOEBE can fit light curves, radial velocity curves, and spectral line profiles for eclipsing binary systems (Prša et al. 2011b). PHOEBE is commonly used by researchers in this field and includes a GUI and significant online resources including tutorials and workshops, making it an attractive package to use in this project. However, PHOEBE's full capacity was unable to be utilised due to the lack of parameters provided in the MOSES data. In this project it was used to plot the light curves of the EBs found from the MOSES data with their errors and PHOEBE's *lc_geometry* function was used to accurately determine the depths of minima, the eclipse widths, and the ingress and egress of each light curve by fitting a 2-gaussian model to the data.

PHOEBE only takes flux measurements for computing models, so the magnitude

measurements from the MOSES data had to be converted to flux. This was done using the equation below:

$$\text{Normalised Flux} = \frac{10^{\frac{-mag}{2.5}}}{10^{-\frac{avmag}{2.5}}} \tag{10}$$

In the equation *mag* is magnitude and *avmag* is the average magnitude outside of eclipse. The fluxes, errors, and periods derived from PDM for each EB found from the MOSES data were input into PHOEBE. PHOEBE was then able to plot the phase folded light curves, examples of which are shown in Figures 28, 29 and 30. The phase folded light curves made by PHOEBE for all the EBs found in the MOSES data can be found in Appendix B.
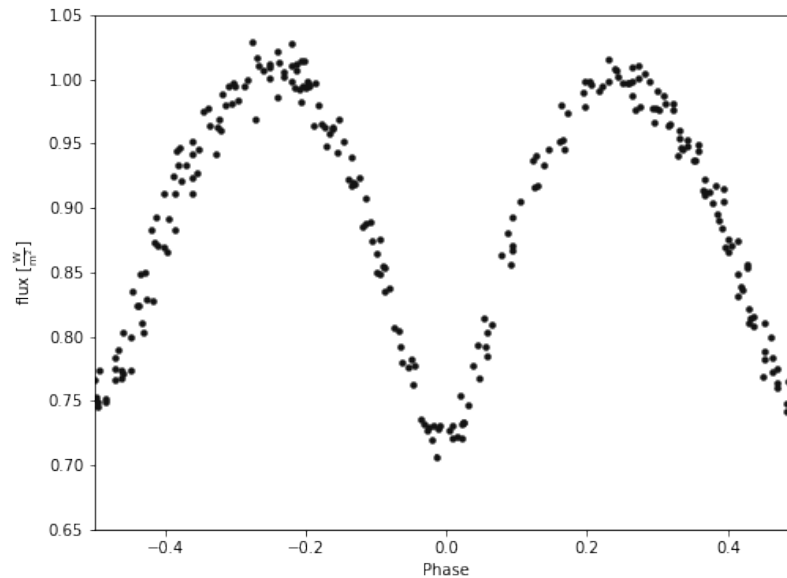


**Figure 28:** The PHOEBE plot for MHT 15185. The continuous variation of the light curve, similar minima depths, and short period of 0.51 days indicate that this is a W UMa type binary system.

48
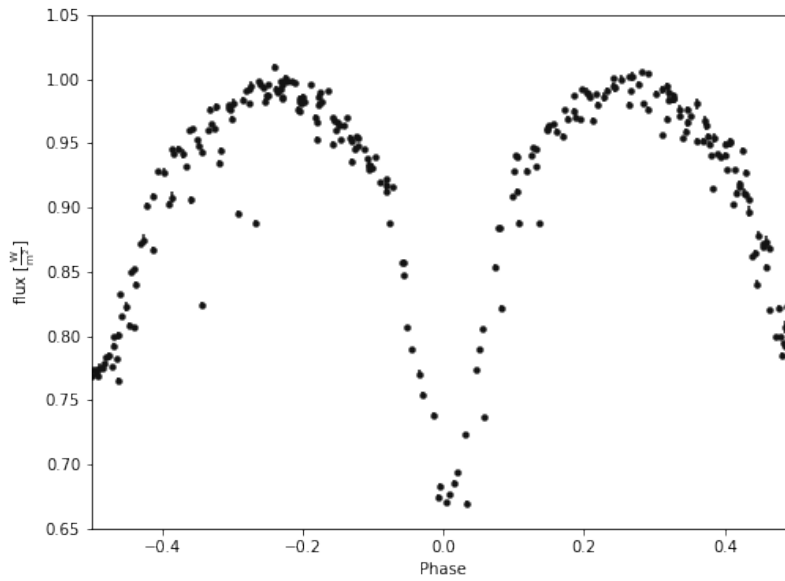


**Figure 29:** The PHOEBE plot for MHT 6742 . The continuous variation of the light curve, significantly different minima depths, and period of 0.69 days indicate that this is a $\beta$ Lyrae type binary system.
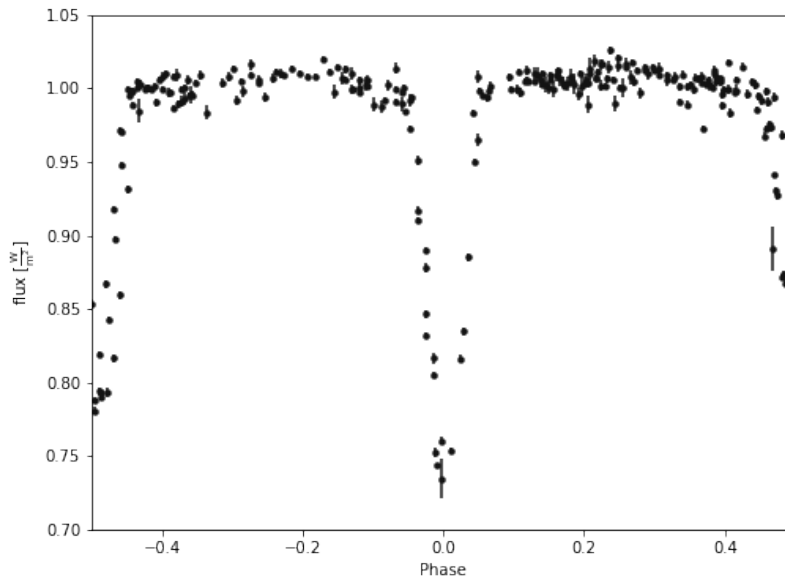


**Figure 30:** The PHOEBE plot for MHT 28909. The constant light outside eclipse and period of 1.64 days indicate that this is an Algol type binary system.

The PHOEBE solver lc_geometry was then used on each dataset. lc_geometry is a light curve geometry estimator which fits a 2-gaussian model to the data which is

used to determine the phases of eclipse minima, eclipse widths, eclipse depths, and the eclipse edges for each EB light curve dataset. The parameters derived by PHOEBE for a subset of EBs from the MOSES data including the systems shown in Figures 28, 29 and 30 are shown in Table 3 below.

The errors on these parameters seen in Table 3 were found by taking away the model that PHOEBE fitted to the data from the original MOSES data. This allowed the residuals to be plotted against phase and the errors to be determined by looking at the scatter of residuals around the phases where measurements were made. Less scatter with residual values around zero indicated smaller errors, whereas larger scatter and residual values that were greater than zero indicated larger errors. The range of scatter was used to determine the magnitudes of the errors.

**Table 3:** Parameters derived by PHOEBE for a subset of EBs.

| MOSES ID (MHT...) | Primary Phase (Phase) | Secondary Phase (Phase) | Primary Width (Phase) | Secondary Width (Phase) | Primary Depth ($\frac{W}{m^2}$) | Secondary Depth ($\frac{W}{m^2}$) |
|---|---|---|---|---|---|---|
| 3799 | $0.33 \pm 0.03$ | $-0.19 \pm 0.04$ | $0.20 \pm 0.03$ | $0.20 \pm 0.03$ | $0.17 \pm 0.02$ | $0.15 \pm 0.06$ |
| 5720 | $0.27 \pm 0.03$ | $-0.22 \pm 0.02$ | $0.33 \pm 0.04$ | $0.30 \pm 0.04$ | $0.40 \pm 0.03$ | $0.38 \pm 0.03$ |
| 6742 | $-0.23 \pm 0.02$ | $0.28 \pm 0.02$ | $0.23 \pm 0.03$ | $0.24 \pm 0.05$ | $0.28 \pm 0.03$ | $0.19 \pm 0.03$ |
| 12030 | $0.36 \pm 0.05$ | $-0.11 \pm 0.04$ | $0.12 \pm 0.03$ | $0.15 \pm 0.05$ | $0.27 \pm 0.04$ | $0.17 \pm 0.05$ |
| 15185 | $0.21 \pm 0.04$ | $-0.29 \pm 0.03$ | $0.30 \pm 0.04$ | $0.32 \pm 0.05$ | $0.22 \pm 0.02$ | $0.19 \pm 0.02$ |
| 20211 | $-0.40 \pm 0.03$ | $0.08 \pm 0.04$ | $0.12 \pm 0.04$ | $0.13 \pm 0.05$ | $0.20 \pm 0.02$ | $0.19 \pm 0.02$ |
| 22431 | $0.28 \pm 0.04$ | $-0.22 \pm 0.05$ | $0.21 \pm 0.06$ | $0.21 \pm 0.06$ | $0.25 \pm 0.04$ | $0.26 \pm 0.04$ |
| 28909 | $-0.09 \pm 0.04$ | $0.42 \pm 0.03$ | $0.13 \pm 0.04$ | $0.12 \pm 0.04$ | $0.27 \pm 0.04$ | $0.22 \pm 0.05$ |
| 30495 | $-0.23 \pm 0.02$ | $0.28 \pm 0.02$ | $0.06 \pm 0.04$ | $0.07 \pm 0.03$ | $0.15 \pm 0.07$ | $0.18 \pm 0.03$ |
| 31867 | $-0.22 \pm 0.03$ | $0.37 \pm 0.02$ | $0.14 \pm 0.06$ | $0.10 \pm 0.06$ | $0.20 \pm 0.03$ | $0.11 \pm 0.01$ |
| 35712 | $-0.42 \pm 0.03$ | $0.18 \pm 0.04$ | $0.26 \pm 0.04$ | $0.50 \pm 0.05$ | $0.48 \pm 0.01$ | $0.24 \pm 0.05$ |

Table 3 shows the parameters PHOEBE derived for the subset of MHT data. The errors are relatively small and when comparing the values to the graphs in Figures 28, 29 and 30 the measurements appear to be accurate for primary phase and secondary phase. The measurements for primary width, secondary width, primary depth, and secondary depth also appear to be accurate for MHT 28909, shown in Figure 30. However,

when comparing the parameters found for widths and depths for MHT 15185 and MHT 6742 with the graphs of their phase folded light curves in Figures 28 and 29 respectively, it can be seen that these parameters have been underestimated by PHOEBE. This is likely due to the continuously varying nature of these light curves. Without a period of constant light outside of the eclipses it is more difficult for PHOEBE to determine where the edges of eclipse are, thus leading to less reliable width and depth measurements. From inspection of the parameters derived and comparison with the corresponding light curves, this was found to be true for almost all of the $\beta$ Lyrae and W UMa systems that were analysed.

We can conclude that PHOEBE is a useful tool in analysing the shape of eclipsing binary phase folded light curves. However, it is more accurate with Algol type light curves, such as in Figure 30, where the start and end of eclipses are obvious due to the periods of constant light outside of the eclipses. PHOEBE becomes less accurate with light curves that continuously vary, such as $\beta$ Lyrae (Figure 29) and W UMa (Figure 28) type light curves.

# 7   Manual Analysis of EBs

To derive absolute parameters of EB systems both photometric and radial velocity data is needed. The MOSES archive only contains photometric data for the objects it observed, meaning that only relative parameters of the systems may be derived. A subset of EB stars, some of which have TESS data also available for them, were analysed in more detail to find some of these relative parameters of the systems.

## 7.1   Classification

The subset of EBs to be analysed were first classified into their different subtypes by eye based on their phase-folded light curves and the periods of the systems. Algols are characterised by constant light outside of their eclipse with minima that dip and rise again abruptly and take up only a small portion of the phased light curve. They have long periods which range from days to weeks or more. $\beta$ Lyrae type EBs have continuously varying light curves, with their minima occupying a sizeable portion of their phased light curve and have periods usually of days. W UMa systems have continuously varying light curves, with their minima depths being very similar, and they typically have periods of less than a day.

The subclasses that were determined for each EB in the subset are shown in Table 4. The subset was found to contain 7 Algol type systems, 5 $\beta$ Lyrae type systems, and 3 W UMa type systems.

**Table 4:** A subset of EBs with their determined subclasses.

| MOSES ID (MHT...) | EB Subclass |
|:---:|:---:|
| 3799 | Algol |
| 5720 | W Ursae Majoris |
| 6742 | $\beta$ Lyrae |
| 9550 | $\beta$ Lyrae |
| 10451 | $\beta$ Lyrae |
| 12030 | Algol |
| 15185 | W Ursae Majoris |
| 20211 | Algol |
| 22431 | Algol |
| 26689 | $\beta$ Lyrae |
| 28909 | Algol |
| 29918 | $\beta$ Lyrae |
| 30495 | Algol |
| 31867 | Algol |
| 35712 | W Ursae Majoris |

## 7.2   Analysis of Temperatures

The temperature ratios for the systems could be found by analysing the depths of eclipses in their phase-folded light curves using Equation 5 from Section 2.3. The change in flux during both the primary and secondary eclipse were determined using PHOEBE, providing values for both $F_0 - F_p$ and $F_0 - F_s$ to be used in the equation. A temperature ratio close to one indicates component stars of similar temperature, whereas a temperature ratio greater or less than one would indicate that the component stars are of significantly different temperatures.

**Table 5:** The temperature ratios of a subset of systems from the MOSES survey.

| MOSES ID (MHT...) | EB Subclass | Temperature Ratio |
|---|---|---|
| 3799 | Algol | $1.03 \pm 0.10$ |
| 5720 | W Ursae Majoris | $1.01 \pm 0.03$ |
| 6742 | $\beta$ Lyrae | $1.11 \pm 0.05$ |
| 9550 | $\beta$ Lyrae | $1.23 \pm 0.09$ |
| 10451 | $\beta$ Lyrae | $1.22 \pm 0.06$ |
| 12030 | Algol | $1.12 \pm 0.09$ |
| 15185 | W Ursae Majoris | $1.03 \pm 0.04$ |
| 20211 | Algol | $1.02 \pm 0.03$ |
| 22431 | Algol | $1.01 \pm 0.05$ |
| 26689 | $\beta$ Lyrae | $1.12 \pm 0.08$ |
| 28909 | Algol | $1.06 \pm 0.07$ |
| 29918 | $\beta$ Lyrae | $1.18 \pm 0.05$ |
| 30495 | Algol | $1.04 \pm 0.12$ |
| 31867 | Algol | $1.16 \pm 0.03$ |
| 35712 | W Ursae Majoris | $1.19 \pm 0.06$ |

Table 5 shows the resulting temperature ratios for the MOSES systems that were analysed. The systems MHT 5720 and MHT 22431 have the smallest temperature ratios with values of $1.01 \pm 0.03$ and $1.01 \pm 0.05$ respectively. This indicates that these EB systems have eclipse minima of similar depths, as can be seen in the phase folded light curve of MHT 5720 in Figure 31. This means that the temperatures of the two component stars in each system are very similar. The shape of MHT 5720's light curve varies continuously, and the system has a period of $0.39 \pm 0.02$ days. Using this information, it was deduced that this system is a W UMa type EB.
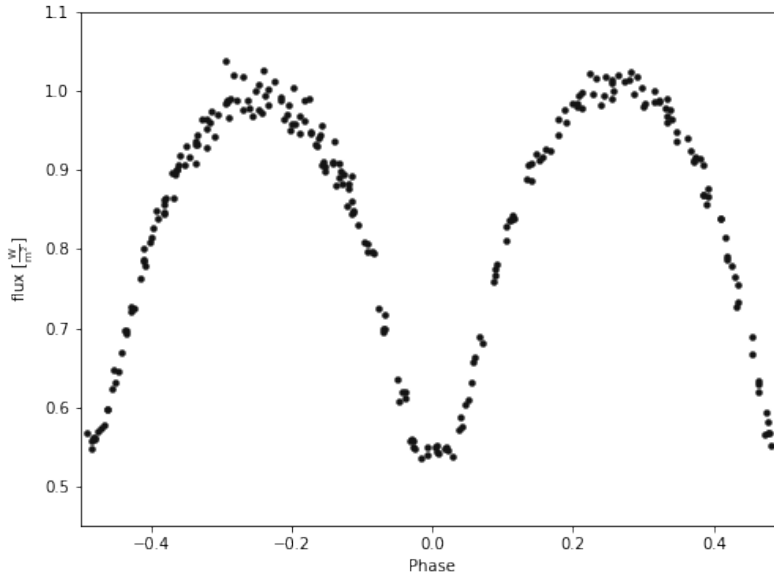
**Figure 31:** The phase-folded light curve of MHT 5720. The system is a W UMa type EB with a period of $0.39 \pm 0.02$ days.

MHT 9550 has the highest temperature ratio with a value of $1.23 \pm 0.09$, indicating an EB system with different depths of eclipse minima, as can be seen in Figure 32. This tells us that the two component stars are of significantly different temperatures. The system has a period of $0.77 \pm 0.02$ days, and has a continuously varying light curve, indicating a $\beta$ Lyrae type EB.
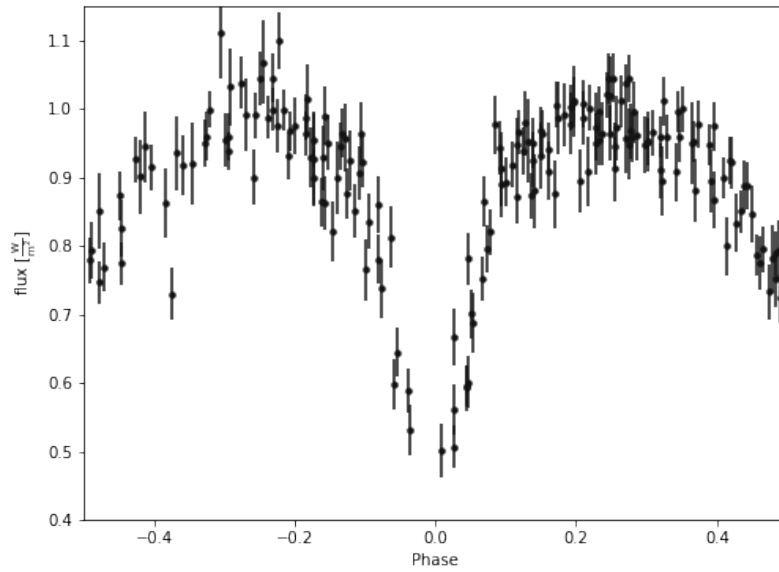
**Figure 32:** The phase-folded light curve of MHT 9550. The system is a $\beta$ Lyrae type EB with a period of $0.77 \pm 0.02$ days.

An example of an Algol type EB can be seen in Figure 33. This is the light curve of MHT 20211 that clearly shows constant light outside of eclipse with the eclipse minima only taking up a small amount of the phased light curve. It has a period of $2.03 \pm 0.02$ days and has a low temperature ratio of $1.02 \pm 0.03$, meaning that the component stars are of a similar temperature.
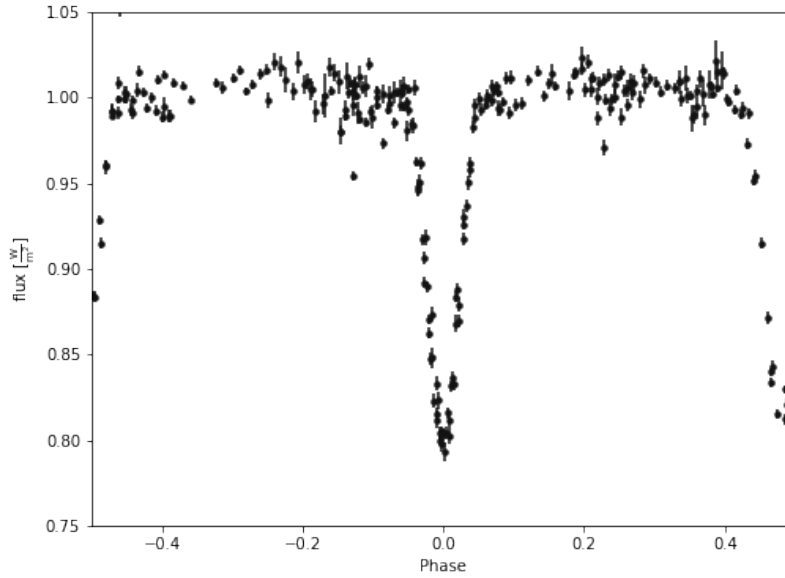
**Figure 33:** The phase-folded light curve of MHT 20211. The system is an Algol type EB with a period of $2.03 \pm 0.02$ days.

Some trends can be determined from the analysis of the temperature ratios and the phase-folded light curves about different types of EB systems. W UMa type systems tend to have similar temperature component stars, giving temperature ratios close to one. This is likely due to the component stars being in physical contact with each other and undergoing mass transfer, bringing the temperatures of the stars closer together as this process is undergone. $\beta$ Lyrae systems tend to have larger temperature ratios, meaning that the temperatures of the component stars are significantly different. Algol type systems have a range of temperature ratios, indicating that the component stars may be very similar in temperature, or conversely may be very different.

## 7.3   Analysis of Diameters

The ratios of the diameters of the component stars in terms of the systems orbital separation can also be found from the shape of their phase-folded light curves. Equations 6 and 7 from Section 2.3 can be rewritten in terms of phase instead of time in order to utilise

the values that the PHOEBE analysis outputs. This gives the following two equations.

$$\phi_4 - \phi_1 = \frac{D_1 + D_2}{2\pi R} \tag{11}$$

$$\phi_3 - \phi_2 = \frac{D_1 - D_2}{2\pi R} \tag{12}$$

Where $\phi_1$ and $\phi_4$ are the phases at the start and end of eclipse respectively, $\phi_2$ and $\phi_3$ are the phases when maximum eclipse depth starts and ends, $D_1$ and $D_2$ are the diameters of the two component stars, and $R$ is the orbital separation of the system. These equations assume an inclination angle of 90°, when the stars pass across the centre of each other with respect to the observer and form flat bottom eclipses. It is the secondary eclipse in the phase-folded light curve, when the smaller radius star passes in front of the larger radius star, which gives the information required for the equations. The slopes of the eclipse minima give information on the radius of the smaller star, and the duration of the flat bottom of the minima gives information on the radius of the larger star.

These equations can be rearranged and substituted into one another to give expressions for $D_1$ and $D_2$ in terms of orbital separation ($R$), as shown below.

$$D_1 = \pi R(\phi_4 - \phi_1 + \phi_3 - \phi_2) \tag{13}$$

$$D_2 = \pi R(\phi_4 - \phi_1 - \phi_3 + \phi_2) \tag{14}$$

The phases at the start and end of the secondary eclipse, $\phi_1$ and $\phi_4$, were determined using PHOEBE, but the phases at the start and end of maximum eclipse depth, $\phi_2$ and $\phi_3$, were determined from the phase-folded light curves of each EB system by eye.

**Table 6:** The diameters of each EB component in terms of the systems orbital separation for a subset of systems from the MOSES survey.

| MOSES ID (MHT...) | EB Subclass | $D_1$ (In terms of R) | $D_2$ (In terms of R) | $D_1 - D_2$ (In terms of R) |
|---|---|---|---|---|
| 3799 | Algol | $0.72 \pm 0.17$ | $0.53 \pm 0.17$ | $0.19 \pm 0.24$ |
| 5720 | W Ursae Majoris | $1.10 \pm 0.17$ | $0.78 \pm 0.17$ | $0.31 \pm 0.25$ |
| 6742 | $\beta$ Lyrae | $0.90 \pm 0.21$ | $0.58 \pm 0.21$ | $0.31 \pm 0.29$ |
| 9550 | $\beta$ Lyrae | $0.93 \pm 0.22$ | $0.43 \pm 0.22$ | $0.50 \pm 0.31$ |
| 10451 | $\beta$ Lyrae | $1.85 \pm 0.22$ | $1.29 \pm 0.22$ | $0.57 \pm 0.31$ |
| 12030 | Algol | $0.53 \pm 0.21$ | $0.41 \pm 0.21$ | $0.13 \pm 0.29$ |
| 15185 | W Ursae Majoris | $1.24 \pm 0.21$ | $0.80 \pm 0.21$ | $0.44 \pm 0.29$ |
| 20211 | Algol | $0.49 \pm 0.21$ | $0.30 \pm 0.21$ | $0.19 \pm 0.29$ |
| 22431 | Algol | $0.79 \pm 0.23$ | $0.54 \pm 0.23$ | $0.25 \pm 0.32$ |
| 26689 | $\beta$ Lyrae | $1.01 \pm 0.23$ | $0.76 \pm 0.23$ | $0.25 \pm 0.32$ |
| 28909 | Algol | $0.44 \pm 0.19$ | $0.32 \pm 0.23$ | $0.13 \pm 0.27$ |
| 29918 | $\beta$ Lyrae | $1.05 \pm 0.22$ | $0.68 \pm 0.22$ | $0.38 \pm 0.31$ |
| 30495 | Algol | $0.31 \pm 0.16$ | $0.12 \pm 0.16$ | $0.19 \pm 0.23$ |
| 31867 | Algol | $0.41 \pm 0.24$ | $0.22 \pm 0.24$ | $0.19 \pm 0.34$ |
| 35712 | W Ursae Majoris | $1.73 \pm 0.21$ | $1.41 \pm 0.21$ | $0.31 \pm 0.29$ |

The relative diameters of the components in terms of their orbital separation for a subset of EBs can be seen in Table 6. The system MHT 10451 has the largest difference in relative diameter between its two components, indicating component stars of significantly different sizes, with each having a value of $1.85 \pm 0.22$ R and $1.29 \pm 0.22$ R respectively, giving a difference of $0.57 \pm 0.31$ R. Its light curve can be seen in Figure 34 which shows very wide eclipses, and a continuously varying light curve. The depths of the two minima are also significantly different and the system has a period of $0.73 \pm 0.02$ days, indicating a $\beta$ Lyrae type system.
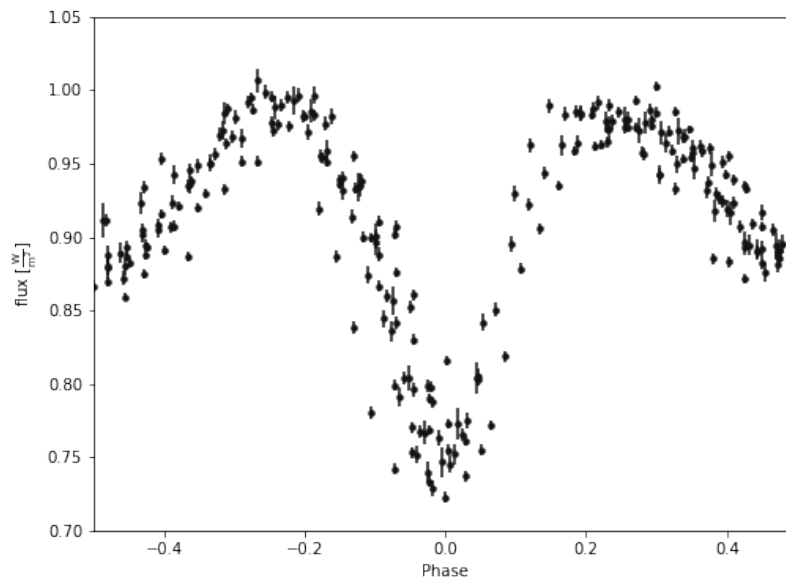
**Figure 34:** The phase-folded light curve of MHT 10451. The system is a $\beta$ Lyrae type EB with a period of $0.73 \pm 0.02$ days.

The systems MHT 20211 and MHT 28909 have the smallest difference in relative diameters, indicating two similarly sized stars orbiting each other. The two components in MHT 20211 have relative diameters of $0.49 \pm 0.21$ R and $0.30 \pm 0.21$ R, giving a difference of $0.19 \pm 0.29$ R, and its light curve can be seen previously in this section in Figure 33. The light curve for MHT 28909 can be seen in Figure 30 in Section 6. This system has components with relative diameters of $0.44 \pm 0.19$ R and $0.32 \pm 0.23$ R respectively, giving a difference of $0.13 \pm 0.27$ R. In both cases, the eclipses in the light curves are very narrow with constant light outside of eclipse, and the two systems have periods of $2.03 \pm 0.02$ days and $1.64 \pm 0.02$ days respectively, indicating Algol type systems.

For further comparison a W UMa system will also be discussed. The light curve for MHT 5720 is shown in Figure 31 previously in this section. Its components have relative diameters of $1.10 \pm 0.17$ R and $0.78 \pm 0.17$ R, giving a difference of $0.31 \pm 0.25$ R. As stated previously, the system has a period of $0.39 \pm 0.02$ days, and its light curve shows continuous variation in brightness, with wide eclipses of similar sizes.

Some trends can be determined from the analysis about the relative diameters of an EBs components and the types of EBs. Algol type systems tend to have component stars of very similar diameter, whereas $\beta$ Lyrae type systems tend to have component stars of very different diameter, and W UMa type systems fall somewhere in between. This is evident in the shape of the different types of systems light curves. Algol type systems have very narrow eclipses that take up a small portion of their phased light curves, whereas $\beta$ Lyrae and W UMa type systems have much wider eclipses, with $\beta$ Lyrae systems also having very different eclipse depths. These wider eclipses make the difference in width and the start and end phase of eclipse minima more pronounced, leading to larger differences in the relative diameters of their component stars.

## 7.4   HR Diagram

Gaia measured the parallaxes and G magnitudes of the EBs from the MOSES survey during its ongoing mission, along with parallaxes and G magnitudes for all of the other objects in the MOSES archive. The data which are used henceforth can be found in Gaia's DR2 data release. This allowed the distances to each system to be calculated using Equation 8 from Section 2.3. Using the distance calculated and the apparent G magnitude measured by Gaia, the absolute G magnitude of each system could be found. The absolute magnitude can be found using Equation 9 from Section 2.3, as shown below.

$$M_G - m_G = -5 \log d + 5 \tag{9}$$

Where $M_G$ is the absolute G magnitude, $m_G$ is the apparent G magnitude, and $d$ is the distance to the system in parsecs.

Gaia also recorded BP (Blue Photometer) and RP (Red Photometer) magnitudes for the systems which provides colour information for each object. This allows an HR diagram to be plotted for the objects in the MOSES archive and provides useful information on the EBs found. Extinction corrections have also been applied to the data

using 3D dustmaps (Dabbs 2021).
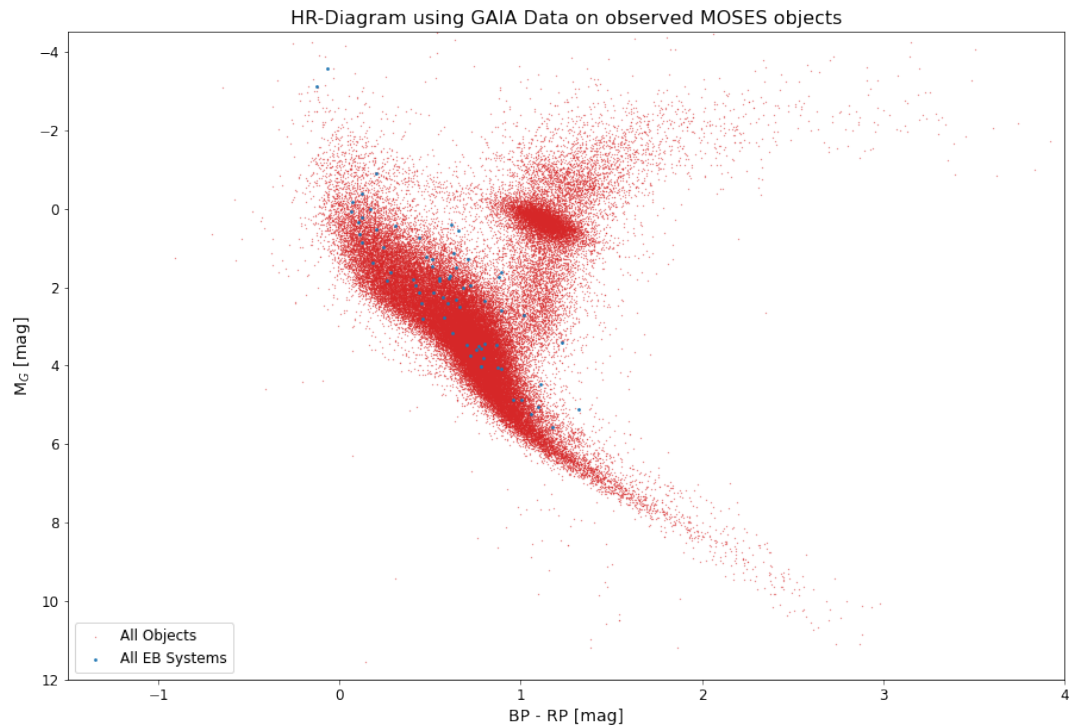


**Figure 35:** An HR diagram of all the objects in the MOSES archive (red) with the EBs found plotted over the top (blue).

The HR diagram in Figure 35 shows that the MOSES archive contains a wide variety of objects that cover almost all areas of a typical HR diagram. Almost all of the EBs found from the MOSES survey lie on the main sequence as expected. However, there are two EBs that sit very high on the main sequence. These are the EBs MHT 3799 and MHT 26689. Their phase-folded light curves can be seen in Figure 36.

(a) MHT 3799
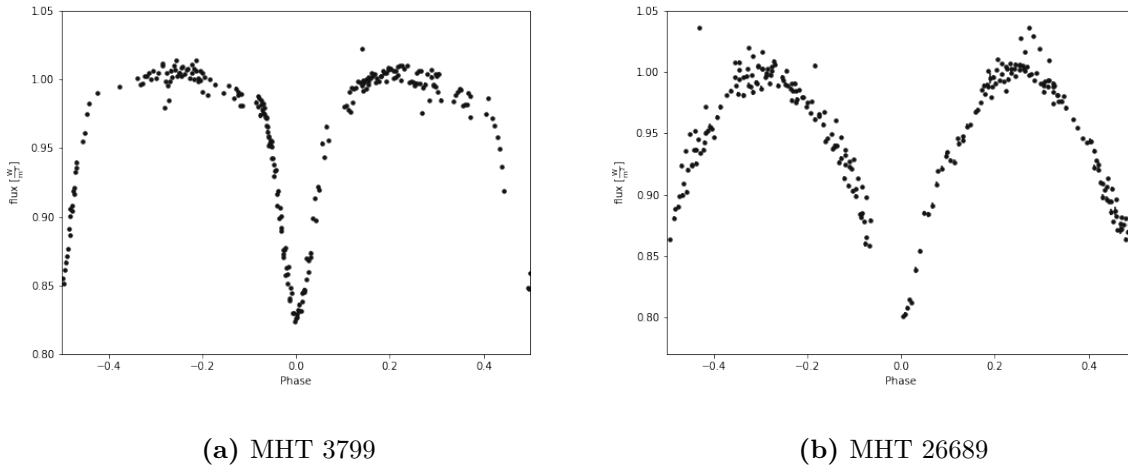
(b) MHT 26689

**Figure 36:** The phase-folded light curves of MHT 3799 and MHT 26689. The systems have periods of 3.69 ± 0.02 days and 1.88 ± 0.02 days respectively.

MHT 3799 can be identified as an Algol type EB from its period of 3.69 ± 0.02 days and its near constant light outside of eclipse. MHT 26689 can be identified as a $\beta$ Lyrae type EB due to its shorter period of 1.88 ± 0.02 days and its continuously varying light curve seen in Figure 36. MHT 3799 was found to have similar temperature component stars with a temperature ratio of 1.03 ± 0.10, whereas MHT 26689 was found to have component stars of different temperatures with a ratio of 1.12 ± 0.08. The differences in relative diameters for MHT 3799 and MHT 26689 were found to be 0.05 ± 0.07 R and 0.13 ± 0.17 R respectively. Unfortunately, as the MOSES archive contains only photometric data, only relative parameters can be derived, giving no indication for absolute values to confirm the systems placements on the HR diagram. The values for BP-RP from Gaia before any corrections were 0.980 mag for MHT 3799 and 1.024 mag for MHT 26689. These became -0.067 mag and -0.127 mag after corrections for extinction. MHT 3799 has a G magnitude of 11.947 mag as measured by Gaia, which after corrections was 9.805 mag, giving an absolute G magnitude of -3.580 mag. Similarly, MHT 26689 has a G magnitude of 12.604 mag, a corrected G magnitude of 10.248 mag and an absolute G magnitude of -3.117 mag.

These values directly lead to the placement of these EBs on the HR diagram,

indicating very bright and hot EBs and suggesting that O or B type stars could be present in the systems. The Gaia archive contains effective temperature values for both of these systems, with MHT 3799 having an effective temperature of 5260 K and MHT 26689 having an effective temperature of 5170 K according to Gaia. These values are much lower than expected for stars found this high on the main sequence. For O or B type stars, typical temperatures are in the range 10,000 - 50,000 K. However, the values from Gaia have not had corrections for extinction applied. DR2 contains no effective temperature values outside of the range 3,000 - 10,000 K as these values were not contained in the training data for the algorithm used to estimate temperatures (Brown et al. 2018). Stars with effective temperatures outside this range will have incorrect values listed in Gaia DR2, with those in high extinction areas being underestimated as the training data didn't contain any stars that suffer from high extinction (Brown et al. 2018). We can assume that since the data has now been corrected for extinction using 3D dustmaps that the EB systems in question were obscured by a lot of dust, making them appear redder and thus making the original temperature derivations by Gaia an underestimate.

The TESS input catalogue also contains effective temperature values for MHT 3799 and MHT 26689 with values of 9420 K and 10,332 K respectively (Stassun et al. 2019). These values are closer to the temperatures expected given their positions on the HR diagram, however, they still seem to be an underestimate. Effective temperatures from TESS are less reliable for hot stars with $G_{BP} - G_{RP} < 0$, as is the case with the systems in question (Stassun et al. 2019).

# 8  Comparisons with TESS Data

TESS observed the same portion of the sky as MOSES observed during its mission, so TESS data were available for some of the EB stars from the MOSES survey. This allowed these EB systems to be analysed again using TESS data and the results to be compared. As TESS is space-based its data are of a higher quality than the ground-based MOSES data. Agreement between results using these two different datasets would indicate that MOSES data are of a high enough quality to accurately derive parameters of EB systems.

Firstly, the TESS light curves were analysed using the same PDM code that was used for the MOSES data. The results are shown alongside the MOSES results in Table 7 below.

**Table 7:** The resulting periods from PDM analysis for MOSES and TESS data of the same systems.

| MOSES ID (MHT...) | TESS ID (TIC...) | MOSES PERIOD ($\pm$ 0.02 Days) | TESS PERIOD ($\pm$ 0.02 days) |
|---|---|---|---|
| 3799 | 12638944 | 3.69 | 3.72 |
| 5720 | 374394641 | 0.39 | 0.39 |
| 6742 | 13526041 | 0.69 | 0.69 |
| 12030 | 12833943 | 1.62 | 1.63 |
| 15185 | 357669270 | 0.51 | 0.51 |
| 20211 | 286123245 | 2.03 | 2.02 |
| 22431 | 374222005 | 2.05 | 2.05 |
| 28909 | 13266469 | 1.64 | 1.65 |
| 30495 | 286125974 | 6.29 | 6.29 |
| 31867 | 627715545 | 2.19 | 2.18 |
| 35712 | 458845005 | 0.79 | 0.79 |

As can be seen from the table, all of the periods determined agree within experimental error between the two different datasets for the same EB systems. Due to the congruence of results, this indicates that the MOSES survey data are of a high enough quality to derive accurate periods for EB systems with short periods (e.g less than 10 days).

The TESS data were then passed through the routine that phase-folded the MOSES light curves and derived parameters for eclipse widths and eclipse depths using PHOEBE. In general, the TESS data provided smoother light curves than the MOSES data that are dense with data points as seen in several of the figures below. All of the phase-folded light curves of TESS datasets plotted by PHOEBE can be found in Appendix C. A comparison of the light curves plotted using MOSES and TESS data of an Algol type EB (MHT 31867) can be seen in Figure 37. The TESS light curve is much smoother, sharper, and denser than the MOSES light curve, but both have small error bars and clearly show the shape of the EBs eclipses.



**(a)** MHT 31867      **(b)** TIC 627715545
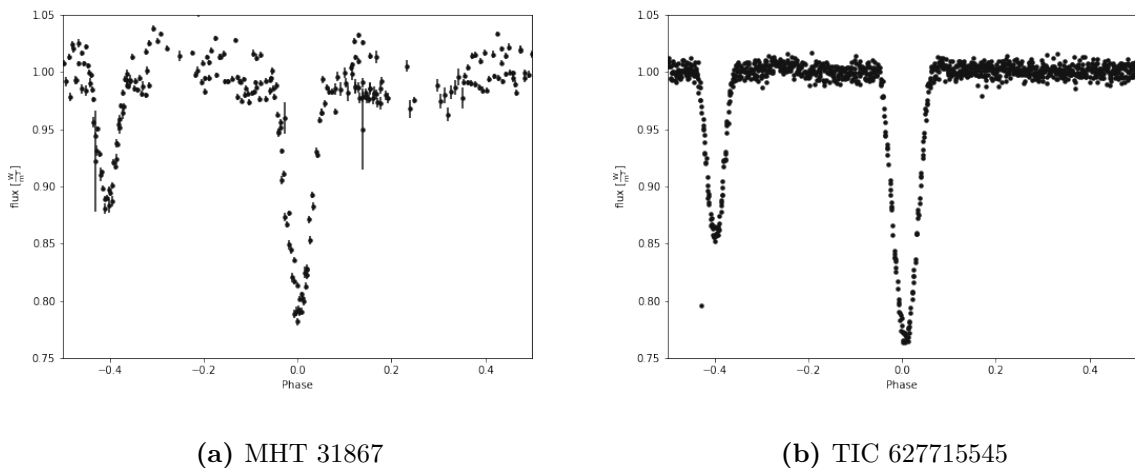
**Figure 37:** The phase-folded light curves for MHT 31867 plotted using PHOEBE for MHT data (error bars plotted) and corresponding TESS data (error bars not plotted: TESS average flux error of 0.01 $W/m^2$).

A comparison for a $\beta$ Lyrae type EB (MHT 6742) plotted using both MOSES and TESS data is shown in Figure 38. Again, the TESS data provide a much denser light curve but both datasets show the eclipses clearly. However, the TESS error bars are significantly larger for a $\beta$ Lyrae type EB, whereas the error bars on the MOSES light curve are again small. This may be due to the errors on the MOSES data being underestimated or the objects could be near to the bright or faint limits for the TESS R+I filter. Comparison of a W UMa type EB plotted using the two datasets can be seen in Figure 39. The same trends described before are also apparent in this light curve comparison,

and again the TESS error bars are even larger for this type of EB. This suggests again that the error bars on the MOSES datapoints may have been underestimated or that the objects may be approaching the bright or faint limits for the TESS filter.



(a) MHT 6742      (b) TIC 13526041
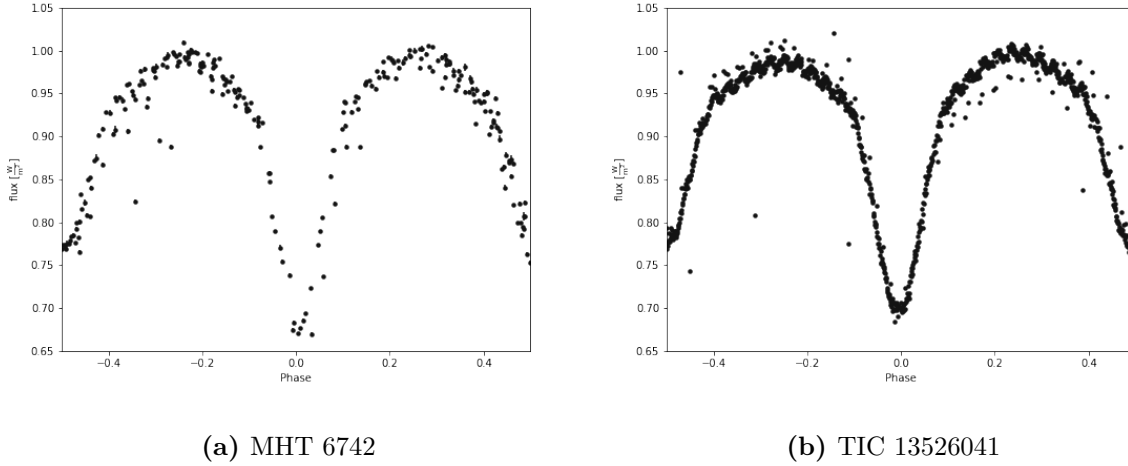
**Figure 38:** The phase-folded light curves for MHT 6742 plotted using PHOEBE for MHT data (error bars plotted) and corresponding TESS data (error bars not plotted: TESS average flux error of 0.05 $W/m^2$).

The results from PHOEBE analysis for eclipse widths and eclipse depths for the TESS data are shown alongside the corresponding results from the MOSES data in Tables 8 and 9 respectively.

**Table 8:** The eclipse widths derived by PHOEBE for both MOSES and TESS data of the same EBs.

| MOSES ID (MHT...) | TESS ID (TIC...) | MOSES Primary Width (Phase) | TESS Primary Width (Phase) | MOSES Secondary Width (Phase) | TESS Secondary Width (Phase) |
|---|---|---|---|---|---|
| 3799 | 12638944 | $0.20 \pm 0.03$ | $0.19 \pm 0.03$ | $0.20 \pm 0.03$ | $0.19 \pm 0.01$ |
| 5720 | 374394641 | $0.33 \pm 0.04$ | $0.44 \pm 0.03$ | $0.30 \pm 0.04$ | $0.41 \pm 0.05$ |
| 6742 | 13526041 | $0.23 \pm 0.03$ | $0.25 \pm 0.03$ | $0.24 \pm 0.05$ | $0.25 \pm 0.05$ |
| 12030 | 12833943 | $0.12 \pm 0.03$ | $0.12 \pm 0.01$ | $0.15 \pm 0.05$ | $0.14 \pm 0.01$ |
| 15185 | 357669270 | $0.30 \pm 0.04$ | $0.48 \pm 0.05$ | $0.32 \pm 0.05$ | $0.47 \pm 0.04$ |
| 20211 | 286123245 | $0.12 \pm 0.04$ | $0.12 \pm 0.04$ | $0.13 \pm 0.05$ | $0.13 \pm 0.05$ |
| 22431 | 374222005 | $0.21 \pm 0.06$ | $0.20 \pm 0.02$ | $0.21 \pm 0.06$ | $0.22 \pm 0.04$ |
| 28909 | 13266469 | $0.13 \pm 0.04$ | $0.12 \pm 0.04$ | $0.12 \pm 0.04$ | $0.12 \pm 0.05$ |
| 30495 | 286125974 | $0.06 \pm 0.04$ | $0.07 \pm 0.01$ | $0.07 \pm 0.03$ | $0.07 \pm 0.01$ |
| 31867 | 627715545 | $0.14 \pm 0.06$ | $0.14 \pm 0.04$ | $0.10 \pm 0.06$ | $0.11 \pm 0.03$ |
| 35712 | 458845005 | $0.26 \pm 0.04$ | $0.50 \pm 0.08$ | $0.50 \pm 0.05$ | $0.45 \pm 0.07$ |

Almost all of the derived eclipse widths between the MOSES and TESS datasets agree within error. There are three EBs out of the eleven with results which do not agree: MHT 5720, MHT 15185, and MHT 35712. The eclipse widths for both the primary and secondary eclipse do not agree for both MHT 5720 and MHT 15185. The phase-folded light curves for MHT 5720 that were plotted using MOSES and TESS data using PHOEBE can be seen in Figure 39. By looking at the start and end phases of eclipse that PHOEBE calculated for each dataset and comparing these values to the graph by eye we can determine why the width values do not agree for this EB. PHOEBE determines the eclipse edges for MHT 5720 using the MOSES data to be at $0.10 \pm 0.04$, $0.44 \pm 0.02$, $-0.37 \pm 0.03$, and $-0.07 \pm 0.02$ phase. Comparing this with the graph in Figure 39 it can be seen that the eclipse edges are inaccurate, with the ingress and egress being cut off, leading to narrower eclipse widths being calculated. PHOEBE determines the eclipse edges for the TESS data of this EB to be at $-0.02 \pm 0.02$, $0.42 \pm 0.02$, $-0.50 \pm 0.04$, and $-0.10 \pm 0.03$ phase, which can be seen to encompass the entire eclipse in both cases, giving larger and more accurate widths than analysis of the MOSES data provided.



(a) MHT 5720        (b) TIC 374394641
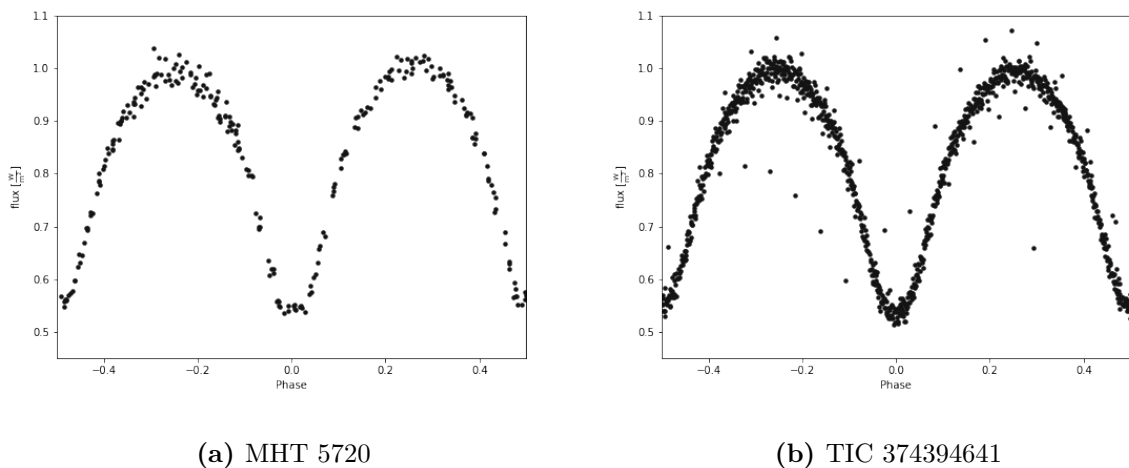
**Figure 39:** The phase-folded light curves for MHT 5720 plotted using PHOEBE for MHT data (error bars plotted) and corresponding TESS data (error bars not plotted: TESS average flux error of 0.18 $W/m^2$).

Similarly, the same issue was found in the discrepancy between eclipse widths for MHT 15185, the phase-folded light curve for which can be seen in Figure 40. PHOEBE computed the eclipse edges for this EB using the MOSES data to be at $0.05 \pm 0.02$, $0.36 \pm 0.03$, $-0.45 \pm 0.03$, and $-0.13 \pm 0.04$ phase. Comparing this to the graph in Figure 40 shows that again the width of eclipses has been underestimated from the MOSES data. The TESS data gave outputs of $-0.22 \pm 0.03$, $0.26 \pm 0.04$, $0.21 \pm 0.03$, and $-0.25 \pm 0.03$ phase for the eclipse edges from PHOEBE. When compared to Figure 40, these values are much more accurate and again encompass the entire eclipse without cutting off the start and end of the eclipses.



(a) MHT 15185      (b) TIC 357669270
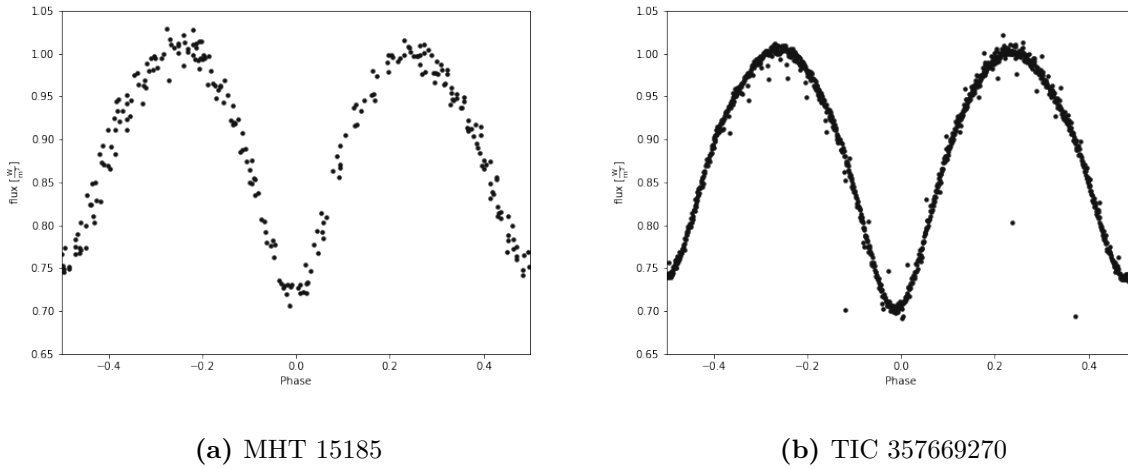
**Figure 40:** The phase-folded light curves for MHT 15185 plotted using PHOEBE for MHT data (error bars plotted) and corresponding TESS data (error bars not plotted: TESS average flux error of 0.13 $W/m^2$).

For MHT 35712 the secondary eclipse widths for each dataset agree within error, but the primary eclipse widths do not. The phase-folded light curves for each dataset can be seen in Figure 41. The eclipses edges derived by PHOEBE from the MOSES data for this EB were $0.45 \pm 0.05$, $-0.29 \pm 0.02$, $-0.07 \pm 0.03$, and $0.43 \pm 0.04$ phase. Comparing these values with Figure 41 it can be seen that the primary eclipse width has again been underestimated, and that the eclipse edges for the secondary eclipse are also inaccurate but shifted to the right of the actual eclipse. This results in a similar eclipse width to the one derived from TESS data despite the inaccuracies for eclipse start and end phase.

The eclipse edges derived from the TESS data for this EB are -0.26 $\pm$ 0.06, 0.24 $\pm$ 0.06, 0.26 $\pm$ 0.05, and -0.29 $\pm$ 0.05 phase. When compared with Figure 41 it can be seen that these values are much more accurate to the eclipse edges seen in the graph.



(a) MHT 35712                    (b) TIC 458845005
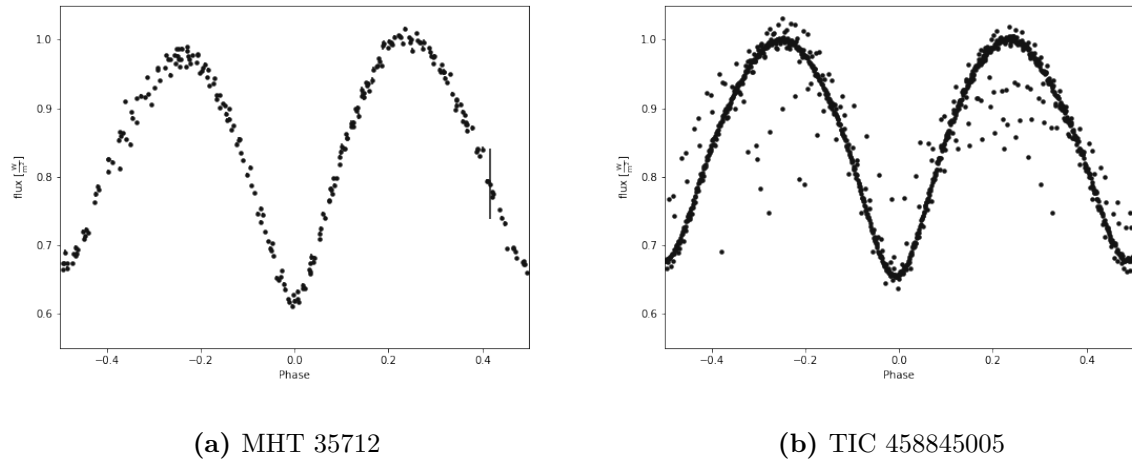
**Figure 41:** The phase-folded light curves for MHT 35712 plotted using PHOEBE for MHT data (error bars plotted) and corresponding TESS data (error bars not plotted: TESS average flux error of 0.16 $W/m^2$).

The depths of eclipses derived by PHOEBE from the MOSES and TESS data for the EBs yields very similar results. The values for depth agree within error for almost all of the EBs except MHT 5720, MHT 15185, and MHT 35712, the same three as before. By comparing the values in Table 9 with the light curves for MHT 5720 and MHT 15185 seen in Figures 39 and 40 respectively, we can see that the depths of minima have been underestimated from the MOSES data, but are accurate from the TESS data. In the case of MHT 35712, comparing the values from Table 9 and the light curves in Figure 41, the primary eclipse depth appears to have been overestimated from the MOSES data but is accurate for the TESS data. The secondary eclipse depth also appears to be underestimated from the MOSES data, and again is accurately derived from the TESS data.

**Table 9:** The eclipse depths derived by PHOEBE for both MOSES and TESS data of the same EBs.

| MOSES ID (MHT...) | TESS ID (TIC...) | MOSES Primary Depth (mags) | TESS Primary Depth (mags) | MOSES Secondary Depth (mags) | TESS Secondary Depth (mags) |
|---|---|---|---|---|---|
| 3799 | 12638944 | $0.17 \pm 0.02$ | $0.17 \pm 0.01$ | $0.15 \pm 0.06$ | $0.17 \pm 0.02$ |
| 5720 | 374394641 | $0.40 \pm 0.03$ | $0.51 \pm 0.01$ | $0.38 \pm 0.03$ | $0.50 \pm 0.01$ |
| 6742 | 13526041 | $0.28 \pm 0.03$ | $0.28 \pm 0.01$ | $0.19 \pm 0.03$ | $0.20 \pm 0.02$ |
| 12030 | 12833943 | $0.27 \pm 0.04$ | $0.25 \pm 0.01$ | $0.17 \pm 0.05$ | $0.20 \pm 0.01$ |
| 15185 | 357669270 | $0.22 \pm 0.02$ | $0.29 \pm 0.01$ | $0.19 \pm 0.02$ | $0.33 \pm 0.01$ |
| 20211 | 286123245 | $0.20 \pm 0.02$ | $0.19 \pm 0.01$ | $0.19 \pm 0.02$ | $0.16 \pm 0.01$ |
| 22431 | 374222005 | $0.25 \pm 0.04$ | $0.27 \pm 0.01$ | $0.26 \pm 0.04$ | $0.28 \pm 0.01$ |
| 28909 | 13266469 | $0.27 \pm 0.04$ | $0.21 \pm 0.02$ | $0.22 \pm 0.05$ | $0.18 \pm 0.01$ |
| 30495 | 286125974 | $0.15 \pm 0.07$ | $0.21 \pm 0.02$ | $0.18 \pm 0.03$ | $0.20 \pm 0.01$ |
| 31867 | 627715545 | $0.20 \pm 0.03$ | $0.24 \pm 0.01$ | $0.11 \pm 0.01$ | $0.14 \pm 0.05$ |
| 35712 | 458845005 | $0.48 \pm 0.01$ | $0.36 \pm 0.02$ | $0.24 \pm 0.05$ | $0.38 \pm 0.02$ |

The relative temperatures were determined using the TESS data for the EB systems using the same method as before, the results for which are found in Table 10. All of the results apart from those for MHT 35712 agree within error between the MOSES and TESS datasets. There is however a trend that the MOSES data produced slightly higher temperature ratios than the TESS data did for the same EBs. This is likely due to the different filters used by the two telescopes. The MOSES observations are in the V band whereas the TESS observations are in broadband R+I filters. Observing the EBs in different filters will result in slightly different light curves due to the wavelength of light emitted from the stars (see (Feng et al. 2021) for an example).

The results for MHT 35712 disagree due to the depth values from PHOEBE being inaccurate using the MOSES data, as discussed before. Using the MOSES data, the primary depth was overestimated, and the secondary depth was underestimated, resulting in a different ratio between the two. It can be seen that the temperature ratios for the two datasets agree for both MHT 5720 and MHT 15185 despite there also being inaccuracies in deriving depths from the MOSES data for these EBs. This is due to the primary and secondary depths both being underestimated in each case, thus keeping the

ratio between the depths roughly the same.

**Table 10:** The temperature ratios calculated from the parameters derived by PHOEBE for both MOSES and TESS data of the same EBs.

| MOSES ID (MHT...) | TESS ID (TIC...) | MOSES Temperature Ratio | TESS Temperature Ratio |
|---|---|---|---|
| 3799 | 12638944 | $1.03 \pm 0.10$ | $1.01 \pm 0.03$ |
| 5720 | 374394641 | $1.01 \pm 0.03$ | $1.00 \pm 0.01$ |
| 6742 | 13526041 | $1.11 \pm 0.05$ | $1.08 \pm 0.03$ |
| 12030 | 12833943 | $1.12 \pm 0.09$ | $1.06 \pm 0.02$ |
| 15185 | 357669270 | $1.03 \pm 0.04$ | $1.03 \pm 0.01$ |
| 20211 | 286123245 | $1.02 \pm 0.03$ | $1.04 \pm 0.02$ |
| 22431 | 374222005 | $1.01 \pm 0.05$ | $1.00 \pm 0.01$ |
| 28909 | 13266469 | $1.06 \pm 0.07$ | $1.03 \pm 0.02$ |
| 30495 | 286125974 | $1.04 \pm 0.12$ | $1.01 \pm 0.03$ |
| 31867 | 627715545 | $1.16 \pm 0.03$ | $1.15 \pm 0.11$ |
| 35712 | 458845005 | $1.19 \pm 0.06$ | $1.02 \pm 0.02$ |

The relative diameters, $D_1$ and $D_2$, with respect to orbital separation, $R$, were derived using the TESS data, and are shown alongside the results from the MOSES data in Table 11. There is good congruence among results with almost all of them agreeing within error. The values for $D_1$ do not agree within error for the EBs MHT 5720 and MHT 15185. This is again due to the inaccuracies in determining the start and end phase of their eclipses using the MOSES data with PHOEBE analysis.

**Table 11:** The relative diameters in terms of orbital separation of the system calculated from the parameters derived by PHOEBE for both MOSES and TESS data of the same EBs.

| MOSES ID (MHT...) | TESS ID (TIC...) | MOSES $D_1$ (In terms of R) | TESS $D_1$ (In terms of R) | MOSES $D_2$ (In terms of R) | TESS $D_2$ (In terms of R) |
|---|---|---|---|---|---|
| 3799 | 12638944 | $0.72 \pm 0.17$ | $0.60 \pm 0.14$ | $0.53 \pm 0.17$ | $0.57 \pm 0.14$ |
| 5720 | 374394641 | $1.10 \pm 0.17$ | $1.77 \pm 0.21$ | $0.78 \pm 0.17$ | $0.80 \pm 0.21$ |
| 6742 | 13526041 | $0.90 \pm 0.21$ | $0.91 \pm 0.21$ | $0.58 \pm 0.21$ | $0.64 \pm 0.21$ |
| 12030 | 12833943 | $0.53 \pm 0.21$ | $0.48 \pm 0.14$ | $0.41 \pm 0.21$ | $0.37 \pm 0.14$ |
| 15185 | 357669270 | $1.24 \pm 0.21$ | $1.76 \pm 0.19$ | $0.80 \pm 0.21$ | $1.16 \pm 0.19$ |
| 20211 | 286123245 | $0.49 \pm 0.21$ | $0.44 \pm 0.21$ | $0.30 \pm 0.21$ | $0.38 \pm 0.21$ |
| 22431 | 374222005 | $0.79 \pm 0.23$ | $0.74 \pm 0.19$ | $0.54 \pm 0.23$ | $0.61 \pm 0.19$ |
| 28909 | 13266469 | $0.44 \pm 0.19$ | $0.43 \pm 0.21$ | $0.76 \pm 0.23$ | $0.35 \pm 0.21$ |
| 30495 | 286125974 | $0.31 \pm 0.16$ | $0.23 \pm 0.14$ | $0.12 \pm 0.16$ | $0.21 \pm 0.14$ |
| 31867 | 627715545 | $0.41 \pm 0.24$ | $0.40 \pm 0.17$ | $0.22 \pm 0.24$ | $0.32 \pm 0.17$ |
| 35712 | 458845005 | $1.73 \pm 0.21$ | $1.62 \pm 0.26$ | $1.41 \pm 0.21$ | $1.23 \pm 0.26$ |

The higher quality TESS data have been found to yield more accurate results when analysed using PHOEBE, however the majority of the values derived from analysis of the MOSES data agree within error with those from the TESS data. The values that did not agree were all derived from W UMa type systems. This shows that PHOEBE has more difficulty constraining the eclipse edges for this type of EB due to the nature of their continuously varying light curves, and that larger datasets that are less sparsely sampled yield more reliable results, such as the TESS datasets used in this analysis comparison. Overall, this shows that the MOSES data can be used reliably for deriving the periods of EBs with a high level of accuracy. It has been shown that it can also be used for analysis of EBs using the methods described previously to determine eclipse widths, eclipse depths, temperature ratios, and relative diameter with a good level of accuracy.

# 9 Conclusion

## 9.1 Overview

Of the 33,038 datasets from the MOSES survey that were analysed, 697 of them were determined to be variable objects. These new objects were analysed using a new version of PDM that was written, which found 70 of the variable objects to be EBs. The periods of the EBs were successfully determined using this PDM software. The co-ordinates of the EBs found were cross-referenced with ASAS-SN's database and AAVSO's VSX database and it was found that 58 of the 70 EBs found are known in the literature. The other 12 are newly discovered EBs.

The EBs were then analysed using PHOEBE to plot their light curves and determine the eclipse widths, depths of minima, and the ingress and egress times. A smaller subgroup of EBs were classified using the shapes of their light curves and the periods that were determined from PDM. Of the 15 EBs that were classified, 7 were found to be Algol type systems, 5 were found to be $\beta$ Lyrae type systems, and 3 were found to be W UMa type systems. This subgroup was also analysed to find the ratios of the temperatures between the component stars and the relative diameters of the components in terms of their orbital separation. An HR diagram for all of the objects observed during the MOSES survey was made by cross-referencing the co-ordinates with Gaia's DR1 and DR2 to find the distances to the objects. The EBs were also plotted on this diagram and were found to lie along the main sequence.

Since TESS has observed the same portion of the sky as MOSES there are TESS data available for some of the EBs found. These data were used to analyse 11 of the EBs again using the same methods and compare the results. It was found that the periods of the EBs between the MOSES and TESS data all agree within experimental error. The TESS observations were found to provide slightly smoother and sharper looking light curves than the MOSES data and the TESS data had far more populated light curves

due to the large amount of data available. Almost all of the eclipse widths and eclipse depths derived using PHOEBE agreed between the two datasets, and those that did not were found to be due to PHOEBE determining the eclipse edges inaccurately for W UMa type EBs from the MOSES data, due to the data being more sparsely sampled. The temperature ratios and relative diameters also agreed well with only one set of results not agreeing among the temperature ratios and two among the relative diameters. These were again due to the determination of eclipse edges of W UMa type systems.

Overall, it was found that the data from the MOSES archive is of a high enough quality to reliably derive the periods of EB systems accurately. It is also suitable to derive relative parameters of EBs from the data using the methods demonstrated such as temperature ratios and relative diameters, with reliable results being derived from Algol and $\beta$ Lyrae type EBs. W UMa type systems were found to be more difficult to analyse reliably, with better results being derived from larger, less sparse datasets, such as from the TESS data that were used for comparison.

## 9.2   Future Work

A subgroup of 15 EB stars were analysed in detail during this project, leaving another 55 EBs to be analysed further using the methods described or similar analysis. There are also multiple implementations of Lomb-Scargle, some of which may work more reliably with the MOSES data than the implementation tested here, as shown in preliminary work by Dabbs (2021). These could be tested for reliability and compared with the results derived here. Additional observations of the EBs could also be taken to provide a much longer baseline to improve the determination of periods. Observations in other photometric bands could also be taken to aid in constraining other properties of the systems, such as stellar type. Using a spectrograph in follow up observations to obtain RV data of a high quality would also allow the absolute parameters for the EBs to be determined.

In this project, only the EBs found from the MOSES data were analysed which

make up 10% of the variable objects found in the MOSES archive, leaving a further 627 variable objects that could also be classified and analysed. With the full set of variable stars, machine learning could be employed to classify the variable stars in the data and classify the eclipsing binaries into their subtypes. This could use a tree-based method to classify the systems based on their parameters, or an image-based method that would classify the systems based on the shapes of their phased light curves.

# References

*AAVSO: The International Variable Star Index* (2022). Accessed: 02/02/2022.
  **URL:** *https://www.aavso.org/vsx/index.php*

Borucki, W., Koch, D., Basri, G., Batalha, N., Brown, T., Caldwell, D., Christensen-Dalsgaard, J., Cochran, W. et al. (2007), 'Finding earth-size planets in the habitable zone: the kepler mission', *Proceedings of the International Astronomical Union* **3**(S249), 17–24.

Brown, A. G. A., Vallenari, A., Prusti, T., Bruijne, J. H. J. d., Babusiaux, C., Bailer-Jones, C. A. L., Bakker, J., Jordan, S. et al. (2018), 'Gaia data release 2. summary of the contents and survey properties', *Astronomy and astrophysics (Berlin)* **616**, 1–22.

Catelan, M. & Smith, H. A. (2015), *Pulsating stars*, Wiley-VCH, Weinheim.

Csizmadia, S. & Klagyivik, P. (2004), 'On the properties of contact binary stars', *Astronomy and astrophysics (Berlin)* **426**(3), 1001–1005.

Dabbs, L. (2021), 'Extending and enhancing the moses survey', *University of Central Lancashire* . Masters thesis.

Dongen, H. P. A. V., Olofsen, E., Hartevelt, J. H. V. & Kruyt, E. W. (1999), 'A procedure of multiple period searching in unequally spaced time-series with the lomb-scargle method', *Biological rhythm research* **30**(2), 149–177.

Feng, G., Esamdin, A., Fu, J., Zhang, Y., Niu, H. & Li, C. (2021), 'Spectroscopic and photometric analysis of the eclipsing binary hip 7666 with  scuti pulsations', *Monthly Notices of the Royal Astronomical Society* .

Gendre, B., Stratta, G., Atteia, J. L., Basa, S., Boër, M., Coward, D. M., Cutini, S., D'Elia, V. et al. (2013), 'The ultra-long gamma-ray burst 111209a: The collapse of a blue supergiant?', *The Astrophysical journal* **766**(1), 30.

Grundahl, F., Clausen, J. V., Hardis, S. & Frandsen, S. (2008), 'A new standard: age and distance for the open cluster ngc 6791 from the eclipsing binary member v20', *Astronomy and Astrophysics* **492**, 171–184.

Ivanova, N., Justham, S., Chen, X., Marco, O., Fryer, C. L., Gaburov, E., Ge, H., Glebbeek, E. et al. (2013), 'Common envelope evolution: where we stand and how we can move forward', *The Astronomy and astrophysics review* **21**(1), 1–73.

Jayasinghe, T., Stanek, K. Z., Kochanek, C. S., Shappee, B. J., Holoien, T. W. S., Thompson, T. A., Prieto, J. L., Dong, S. et al. (2018), 'The asas-sn catalog of variable stars ii: Uniform classification of 412,000 known variables', *Monthly Notices of the Royal Astronomical Society* .

Kallrath, J. & Milone, E. F. (2009a), *Eclipsing Binary Stars: Modeling and Analysis*, 2 edn, Springer, New York.

Kallrath, J. & Milone, E. F. (2009b), *The Wilson–Devinney Program: Extensions and Applications*, Eclipsing Binary Stars: Modeling and Analysis, Springer New York, New York, NY, pp. 305–330.

Karttunen, H., Kroger, P., Oja, H., Poutanen, M. & Donner, K. J. (2007), *Observations and Instruments*, Springer Berlin Heidelberg, Berlin, Heidelberg.

Kervella, P., Thevenin, F., Folco, E. D. & Segransan, D. (2004), 'The angular size of dwarf stars and subgiants - surface brightness relations calibrated by interferometry', *Astronomy and Astrophysics* **426**, 297–307.

Kirk, B., Conroy, K., Prša, A., Abdul-Masih, M., Kochoska, A., Matijevič, G., Hambleton, K., Barclay, T. et al. (2016), 'Kepler eclipsing binary stars. vii. the catalog of eclipsing binaries found in the entire kepler data set', *The Astronomical Journal* **151**(3).

Knigge, C., Baraffe, I. & Patterson, J. (2011), 'The evolution of cataclysmic variables as revealed by their donor stars', *The Astrophysical journal. Supplement series* **194**(2), 28.

Kopal, Z. (1959), *Close Binary Systems*, Chapman Hall, London, UK.

Kovács, G., Zucker, S. & Mazeh, T. (2002), 'A box-fitting algorithm in the search for periodic transits ', *Astronomy and Astrophysics* **391**, 369–377.

Lindegren, L., Hernández, J., Bombrun, A., Klioner, S., Bastian, U., Ramos-Lerate, M., de Torres, A., Steidelmüller, H. et al. (2018), 'Gaia data release 2. the astrometric solution', *Astronomy and Astrophysics* .

Lindegren, L., Lammers, U., Bastian, U., Hernandez, J., Klioner, S., Hobbs, D., Bombrun, A., Michalik, D. et al. (2016), 'Gaia data release 1: Astrometry - one billion positions, two million proper motions and parallaxes', *Astronomy and astrophysics (Berlin)* **595**, id.A4.

Martín-Fleitas, J., Sahlmann, J., Mora, A., Kohley, R., Massart, B., L'Hermitte, J., Roy, M. L. & Paulet, P. (2014), Enabling gaia observations of naked-eye stars, Vol. 9143, SPIE, pp. 91430Y–12.

*Planewave Instrument, CDK700* (2020). Accessed: 09/01/2022.
   **URL:** *https://planewave.com/product/cdk700-0-7m-cdk-telescope-system/*

Prša, A. (2018), *Modeling and analysis of eclipsing binary stars*, IOP Publishing, Bristol England (Temple Circus, Temple Way, Bristol BS1 6HG, UK).

Prša, A., Batalha, N., Slawson, R. W., Doyle, L. R., Welsh, W. F., Orosz, J. A., Seager, S., Rucker, M. et al. (2011a), 'Kepler eclipsing binary stars. i. catalog and principal characterization of 1879 eclipsing binaries in the first data release', *The Astronomical Journal* **141**(83).

Prša, A., Matijevic, G., Latkovic, O., Vilardell, F. & Wils, P. (2011b), 'Phoebe: Physics of eclipsing binaries', *Astrophysics Source Code Library* .

Prša, A. & Zwitter, T. (2005), 'A computational guide to physics of eclipsing binaries. i. demonstrations and perspectives', *The Astrophysical journal* **628**(1), 426–438.

Rambukwella-Gill, A. S. (2019), 'Moses: Mht optical star and exoplanet survey'. Masters thesis. Accessed: 09/01/22.
   **URL:** *http://clok.uclan.ac.uk/34495/*

Ricker, G. R., Winn, J. N., Vanderspek, R., Latham, D. W., Bakos, G. , Bean, J. L., Berta-Thompson, Z. K., Brown, T. M. et al. (2015), 'Transiting exoplanet survey satellite', *Journal of astronomical telescopes, instruments, and systems* **1**(1), 014003.

Russell, H. N. & Merrill, J. E. (1952), *The Determination of the Elements of Eclipsing Binaries*, Princeton University Press, USA.

Shappee, B. J., Prieto, J. L., Grupe, D., Kochanek, C. S., Stanek, K. Z., Rosa, G. D., Mathur, S., Zu, Y. et al. (2014), 'The man behind the curtain: X-rays drive the uv through nir variability in the 2013 active galactic nucleus outburst in ngc 2617', *The Astrophysical journal* **788**(1), 48.

Simonsen, M. (2012), *Variable Star Classification and Light Curves*, Carolyn Hurless Online Institute for Continuing Education in Astronomy (CHOICE).

Southworth, J., Maxted, P. F. L. & Smalley, B. (2005a), 'Eclipsing binaries as standard candles: Hd 23642 and the distance to the pleiades', *Astronomy and Astrophysics (Berlin)* **429**, 645–655.

Southworth, J., Smalley, B., Maxted, P. F. L., Claret, A. & Etzel, P. B. (2005b), 'Absolute dimensions of detached eclipsing binaries. i. the metallic-lined system ww aurigae', *Monthly Notices of the Royal Astronomical Society* **363**, 529–542.

Stassun, K. G., Oelkers, R. J., Paegert, M., Torres, G., Pepper, J., Lee, N. D., Collins, K., Latham, D. W. et al. (2019), 'The revised tess input catalog and candidate target list', *The Astronomical Journal* **158**.

Stellingwerf, R. F. (1978), 'Period determination using phase dispersion minimization', *The Astrophysical journal* **224**, 953.

Udalski, A., Szymański, M. K. & Szymański, G. (2015), 'Ogle-iv: Fourth phase of the optical gravitational lensing experiment', *Acta Astronomica* **65**(1), 1–38.

VanderPlas, J. T. (2018), 'Understanding the lomb–scargle periodogram', *The Astrophysical Journal* **236**(16), 1–2.

Vilardell, F., Ribas, I., Jordi, C., Fitzpatrick, E. L. & Guinan, E. F. (2010), 'The distance to the andromeda galaxy from eclipsing binaries', *Astronomy and Astrophysics* **509**, 171–184.

Vogel, H. C. (1890), 'Spectrographische beobachtungen an algol', *Astronomische Nachrichten* **123**, 289.

Walker, R. (2017), *Spectral Atlas for Amateur Astronomers*, Cambridge University Press.

Watson, C. L., Henden, A. A. & Price, A. (2006), 'The international variable star index (vsx)', *Society for Astronomical Sciences* p. 47.

Wilson, R. E. & Devinney, E. J. (1971), 'Realization of accurate close-binary light curves: Application to mr cygni', *The Astrophysical journal* **166**, 605.

# 10 Appendices

## 10.1 Appendix A: MOSES EB Periods

**Table 12:** The derived periods for all the EBs found in the MOSES survey

| MHT ID | Period ($\pm$ 0.02 Days) | MHT ID | Period ($\pm$ 0.02 Days) |
|---|---|---|---|
| MHT 2707 | 1.71 | MHT 19537 | 2.64 |
| MHT 3549 | 1.66 | MHT 20080 | 3.80 |
| MHT 3799 | 3.70 | MHT 20211 | 2.03 |
| MHT 4206 | 1.44 | MHT 20473 | 0.84 |
| MHT 4708 | 0.75 | MHT 22431 | 2.05 |
| MHT 5132 | 0.55 | MHT 22695 | 0.48 |
| MHT 5720 | 0.39 | MHT 23589 | 0.25 |
| MHT 6742 | 0.69 | MHT 26229 | 1.37 |
| MHT 7687 | 0.41 | MHT 26689 | 1.88 |
| MHT 7981 | 1.11 | MHT 27033 | 0.25 |
| MHT 8476 | 0.40 | MHT 27293 | 0.69 |
| MHT 8489 | 1.21 | MHT 28909 | 1.64 |
| MHT 8490 | 4.26 | MHT 28973 | 0.58 |
| MHT 8524 | 0.55 | MHT 29516 | 1.68 |
| MHT 8783 | 1.26 | MHT 29705 | 0.39 |
| MHT 9550 | 0.77 | MHT 29918 | 0.58 |
| MHT 9857 | 4.40 | MHT 30481 | 0.67 |
| MHT 10451 | 0.73 | MHT 30495 | 6.29 |
| MHT 10636 | 0.33 | MHT 31041 | 0.35 |
| MHT 10886 | 0.78 | MHT 31205 | 4.71 |
| MHT 11212 | 2.52 | MHT 31822 | 0.44 |
| MHT 11762 | 5.90 | MHT 31867 | 2.19 |
| MHT 12030 | 1.62 | MHT 31948 | 0.34 |
| MHT 12056 | 5.36 | MHT 31956 | 0.87 |
| MHT 12510 | 0.54 | MHT 32190 | 0.48 |
| MHT 12782 | 2.80 | MHT 32831 | 0.39 |
| MHT 13617 | 0.28 | MHT 34595 | 3.31 |
| MHT 14747 | 0.89 | MHT 34596 | 0.54 |
| MHT 14758 | 0.29 | MHT 35564 | 2.69 |
| MHT 15185 | 0.51 | MHT 35712 | 0.79 |
| MHT 15220 | 1.15 | MHT 36815 | 1.95 |
| MHT 15846 | 0.64 | MHT 38795 | 4.43 |
| MHT 16056 | 0.90 | MHT 39408 | 0.32 |
| MHT 17309 | 1.17 | MHT 42898 | 0.52 |
| MHT 17580 | 0.28 | MHT 48251 | 0.42 |

## 10.2 Appendix B: MOSES Light Curves
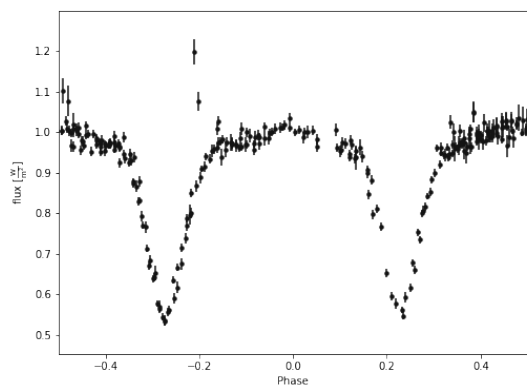


(a) MHT 2707
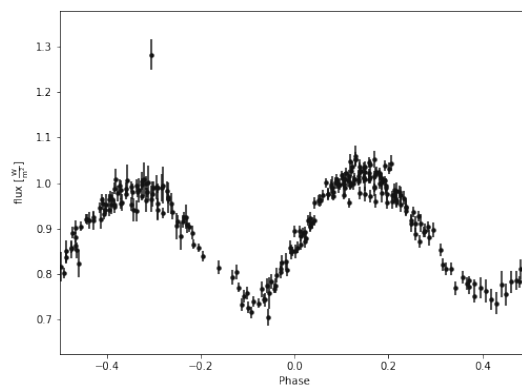


(b) MHT 3549
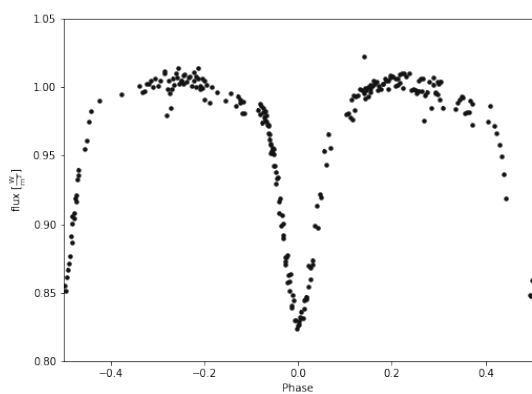


(c) MHT 3799
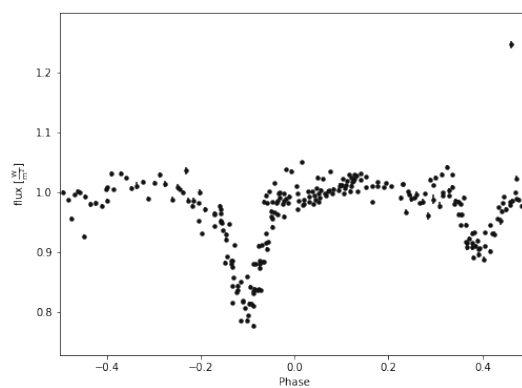


(d) MHT 4206
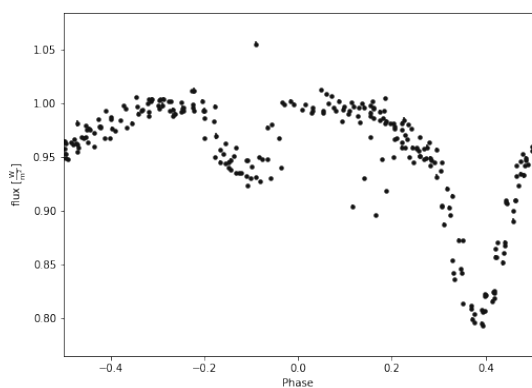


(e) MHT 4708
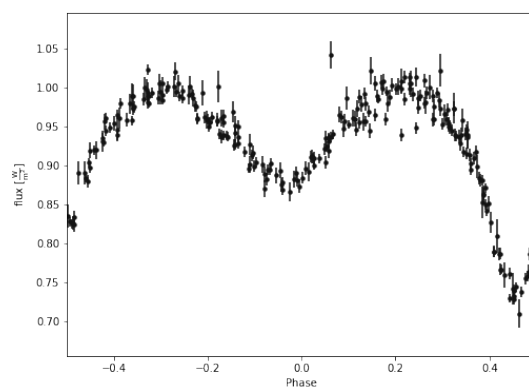


(f) MHT 5132
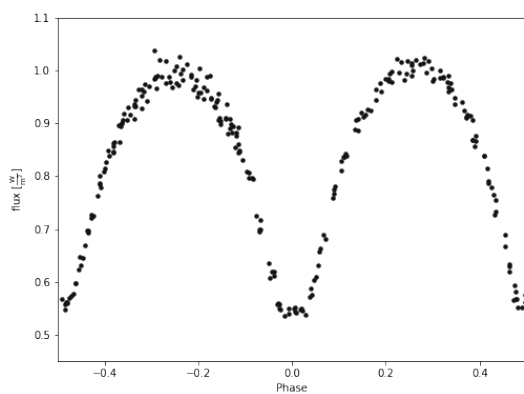
**(g)** MHT 5720
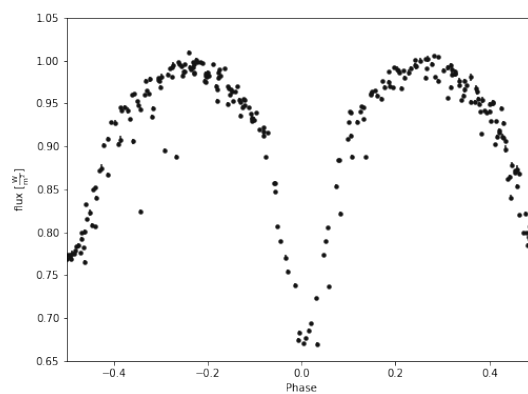


**(h)** MHT 6742
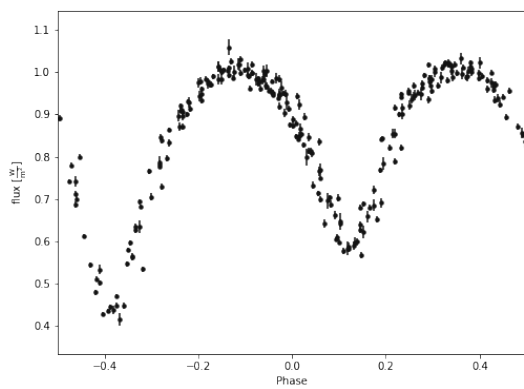


**(i)** MHT 7687
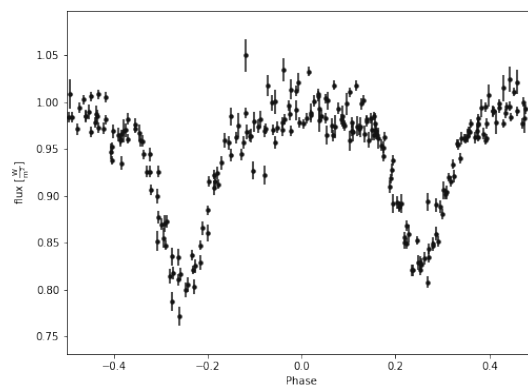


**(j)** MHT 7981
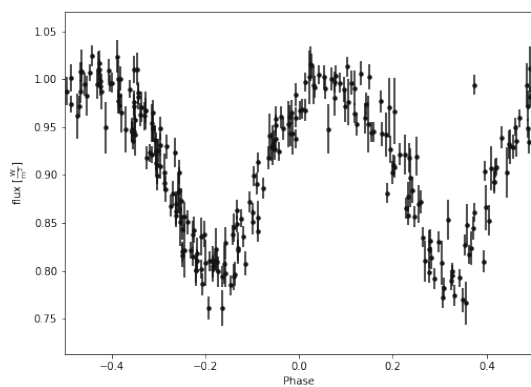


**(k)** MHT 8476
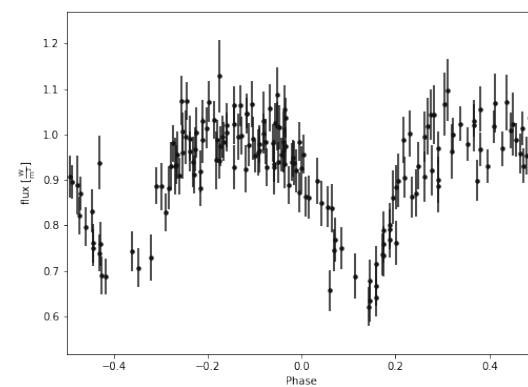


**(l)** MHT 8489
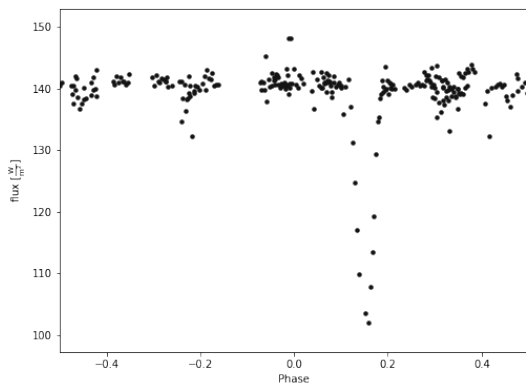
(m) MHT 8490
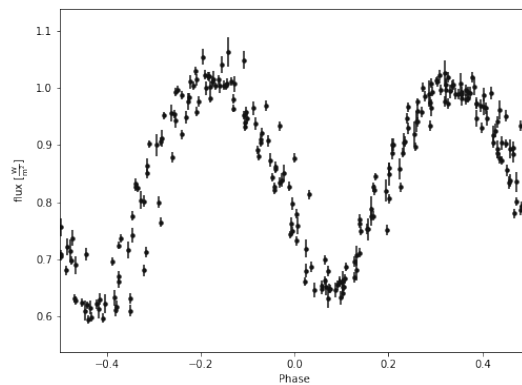


(n) MHT 8524
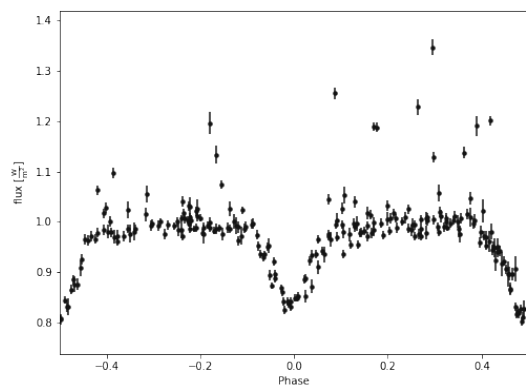


(o) MHT 8783
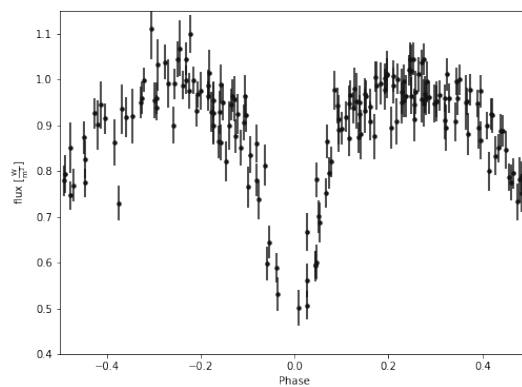


(p) MHT 9550
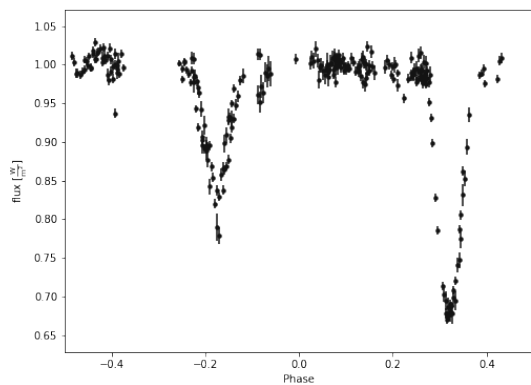


(q) MHT 9857
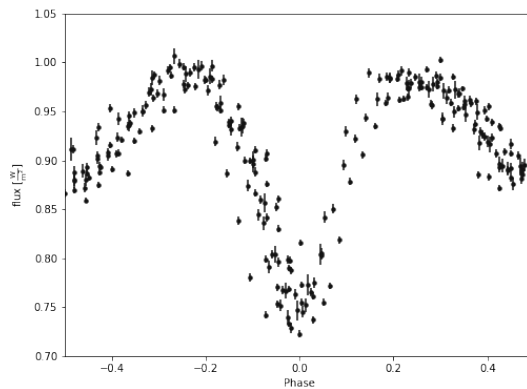


(r) MHT 10451
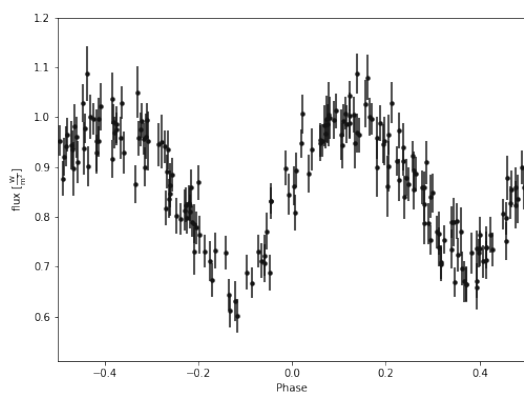
**(s)** MHT 10636
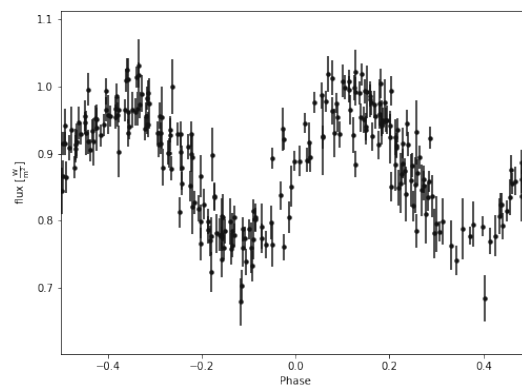


**(t)** MHT 10886
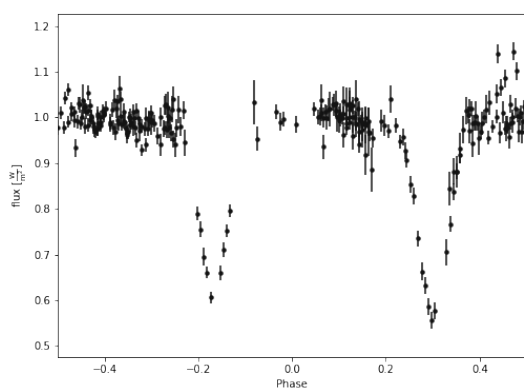


**(u)** MHT 11212
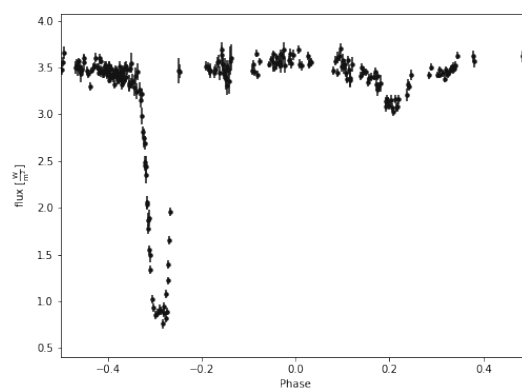


**(v)** MHT 11762
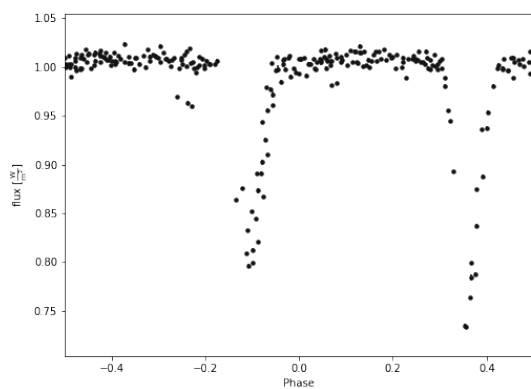


**(w)** MHT 12030
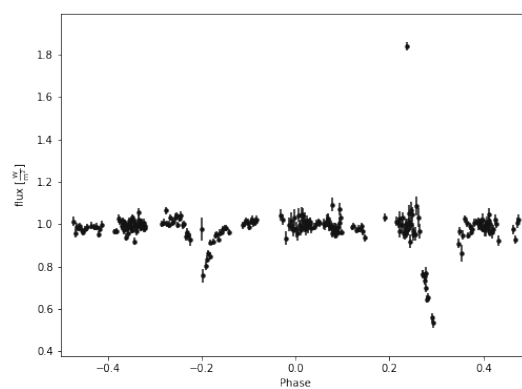


**(x)** MHT 12056
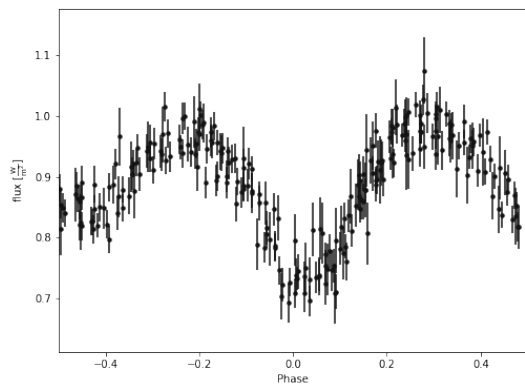
**(y)** MHT 12510
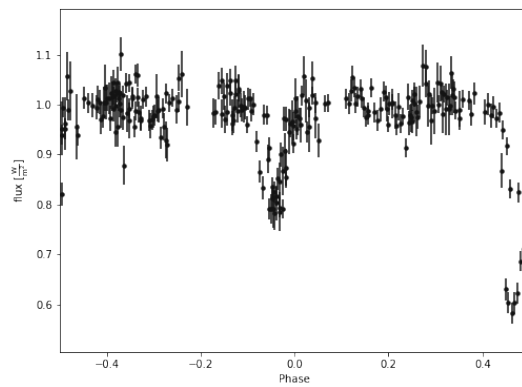


**(z)** MHT 12782
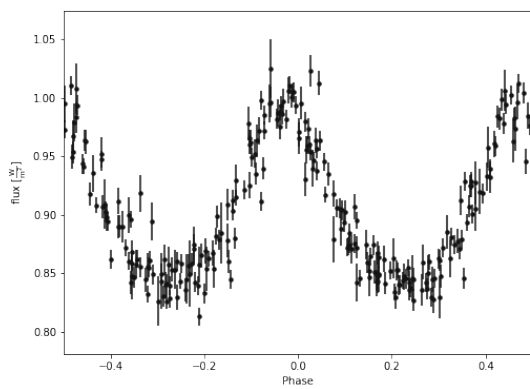


**(aa)** MHT 13617
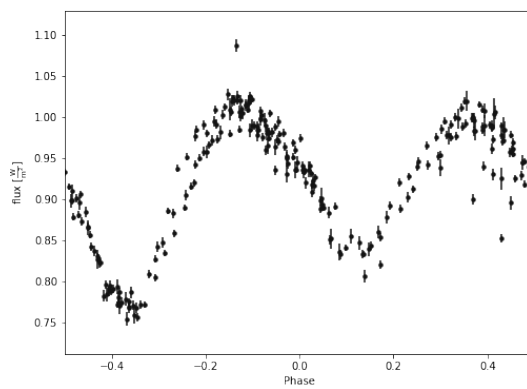


**(ab)** MHT 14747
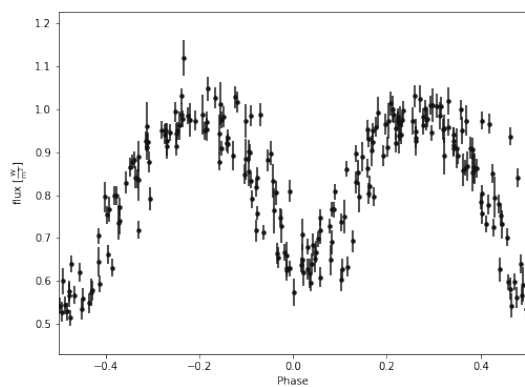


**(ac)** MHT 14758
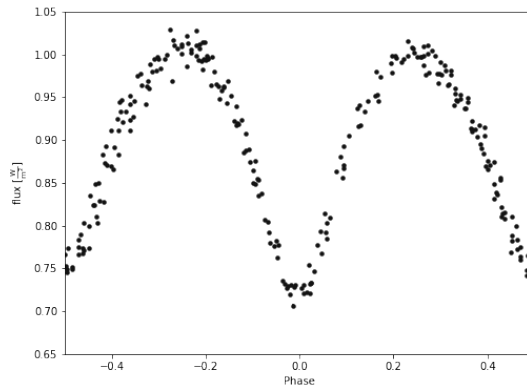


**(ad)** MHT 15185
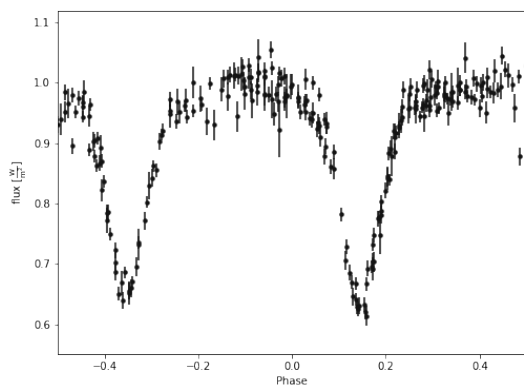
**(ae)** MHT 15220
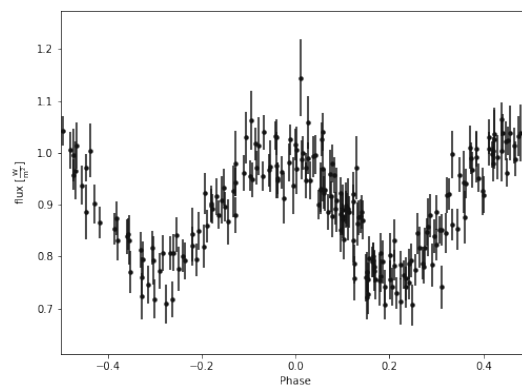


**(af)** MHT 15846
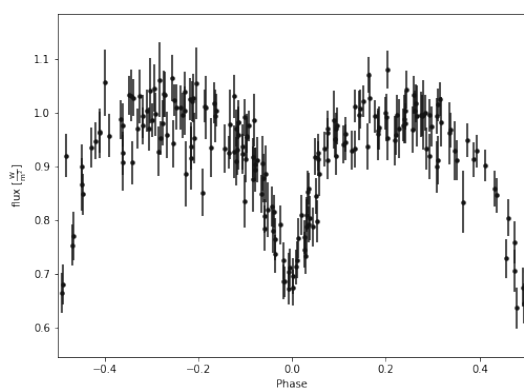


**(ag)** MHT 16056
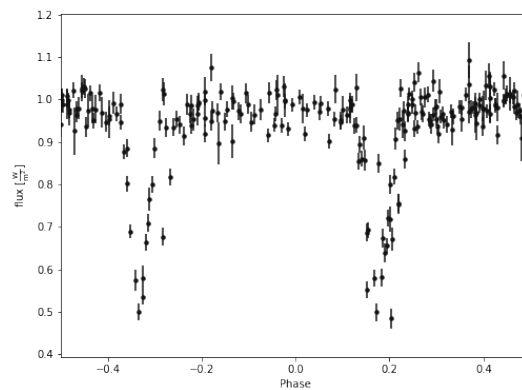


**(ah)** MHT 17309
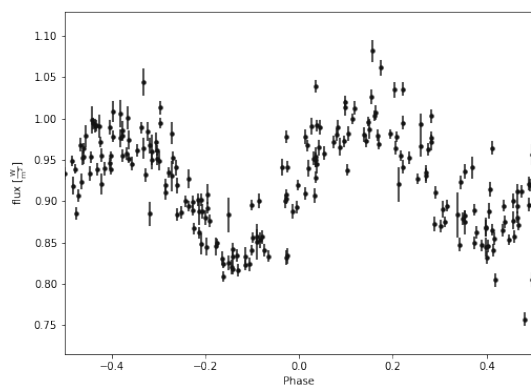


**(ai)** MHT 17580
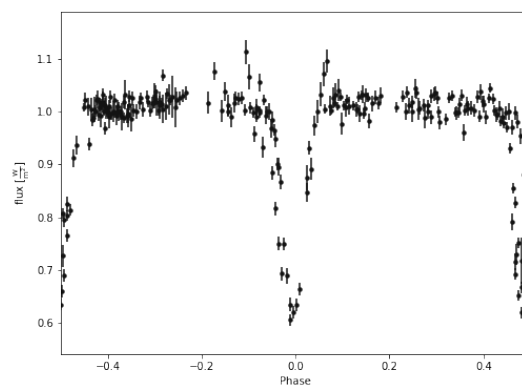


**(aj)** MHT 19537
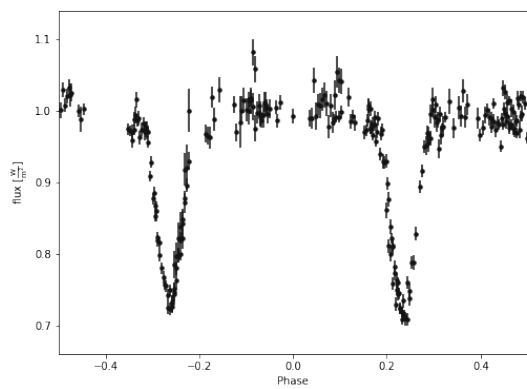
(ak) MHT 20080
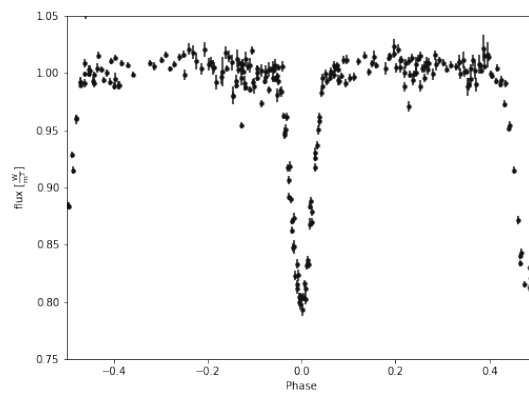


(al) MHT 20211
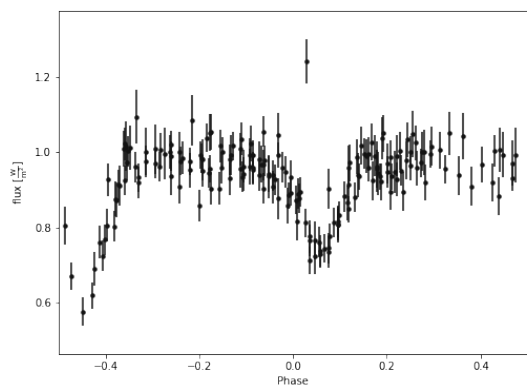


(am) MHT 20473
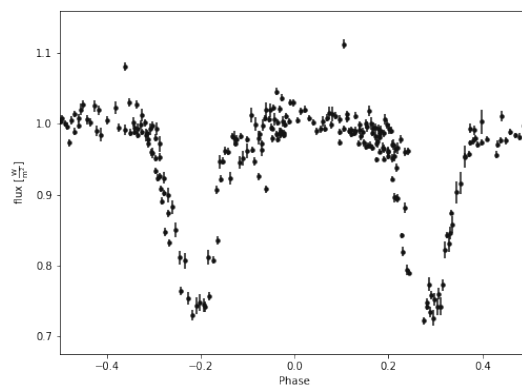


(an) MHT 22431
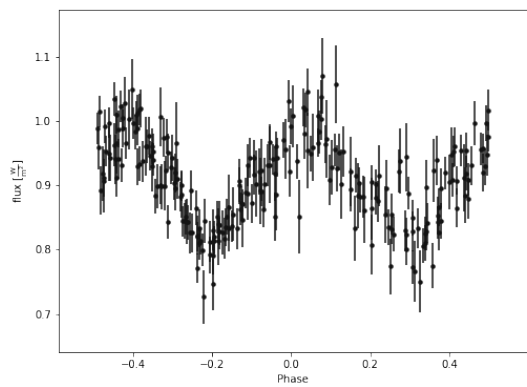


(ao) MHT 22695
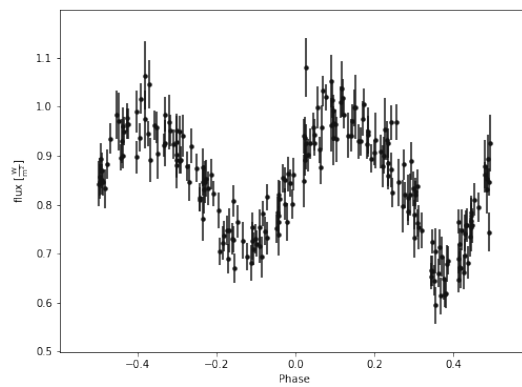


(ap) MHT 23589
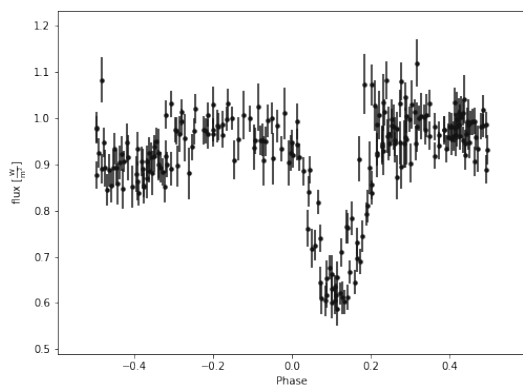
**(aq)** MHT 26229
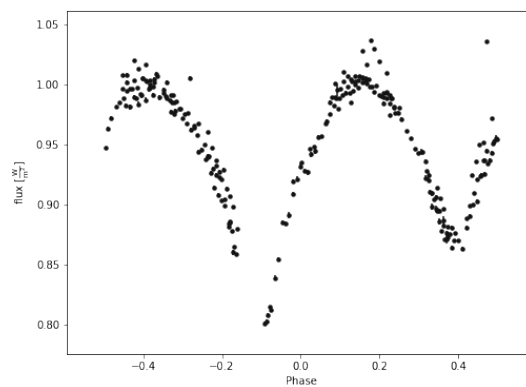


**(ar)** MHT 26689
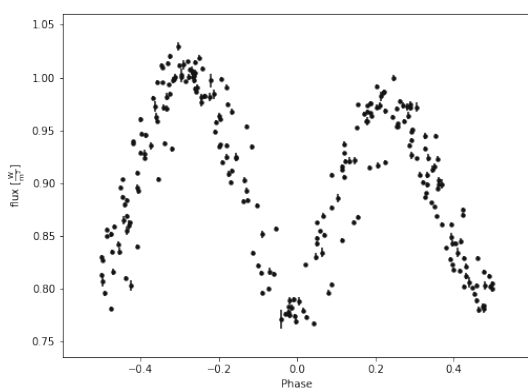


**(as)** MHT 27033
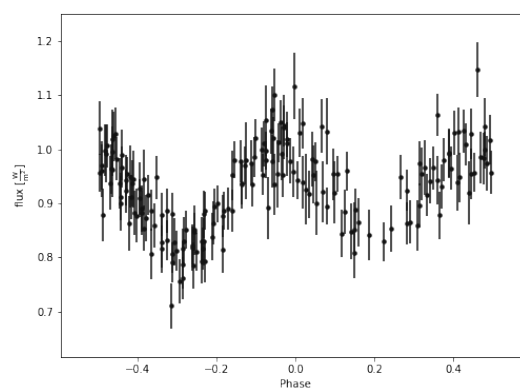


**(at)** MHT 27293
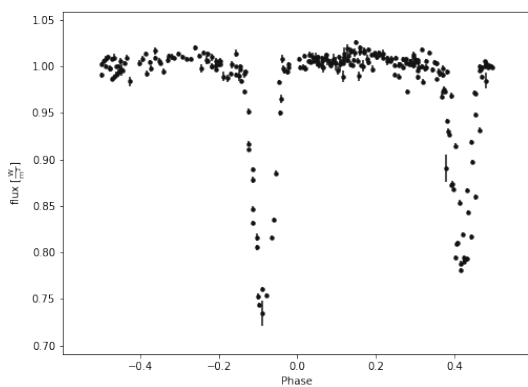


**(au)** MHT 28909
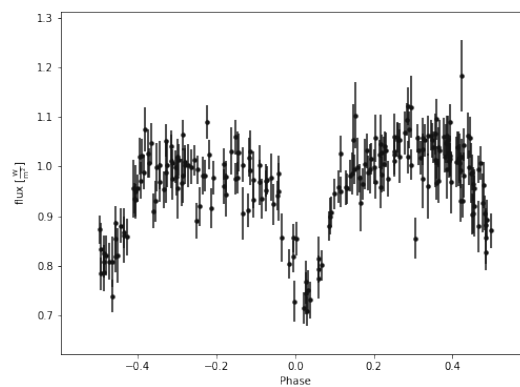


**(av)** MHT 28973
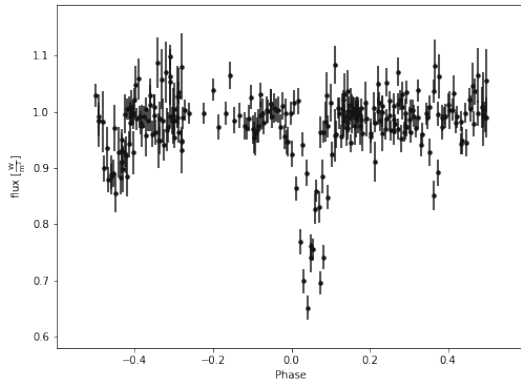
**(aw)** MHT 29516
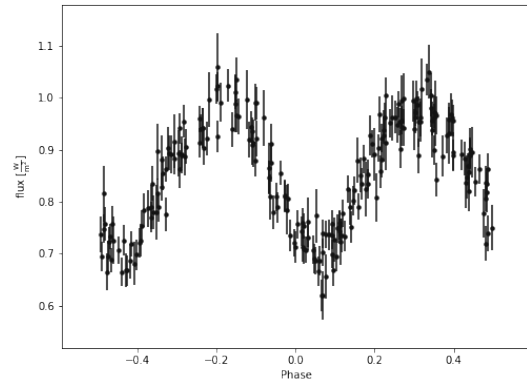


**(ax)** MHT 29705
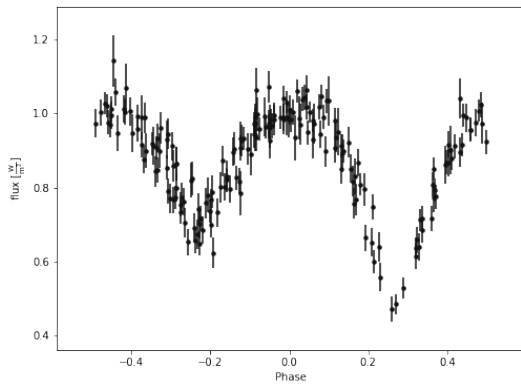


**(ay)** MHT 29918
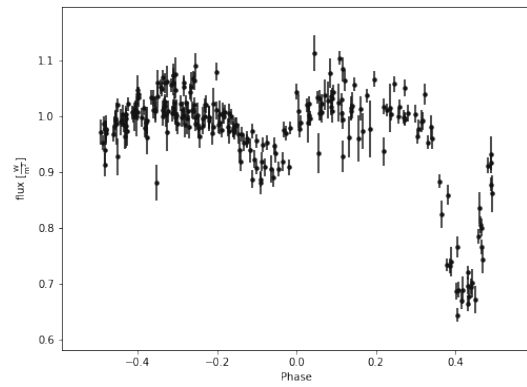


**(az)** MHT 30481
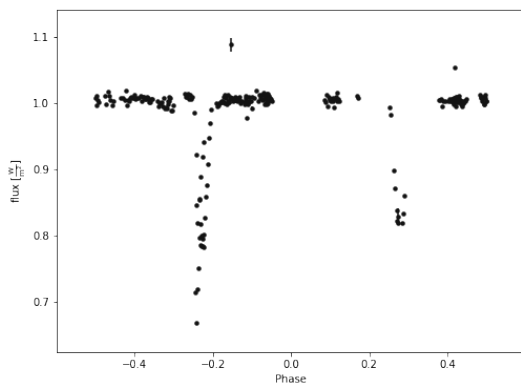


**(ba)** MHT 30495
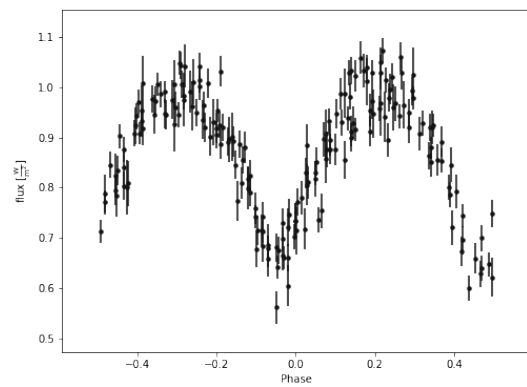


**(bb)** MHT 31041
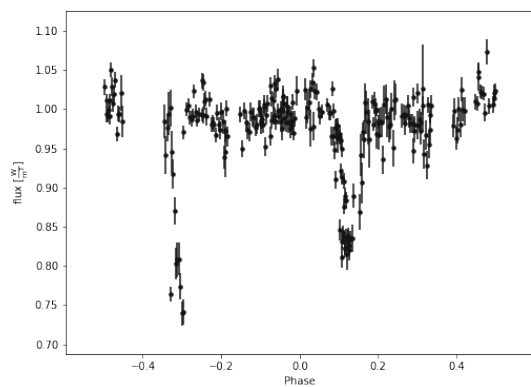
**(bc)** MHT 31205
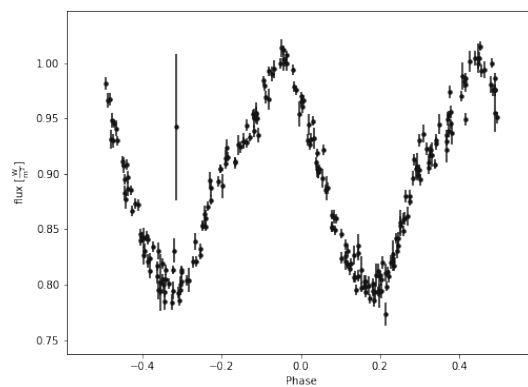


**(bd)** MHT 31822
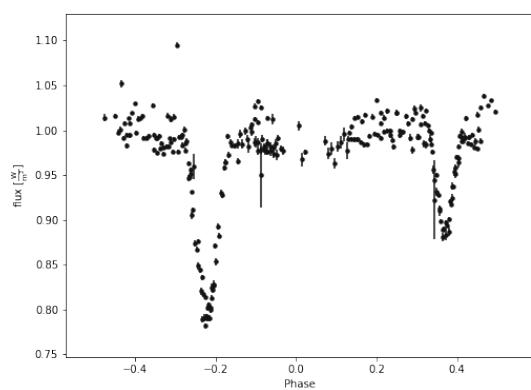


**(be)** MHT 31867
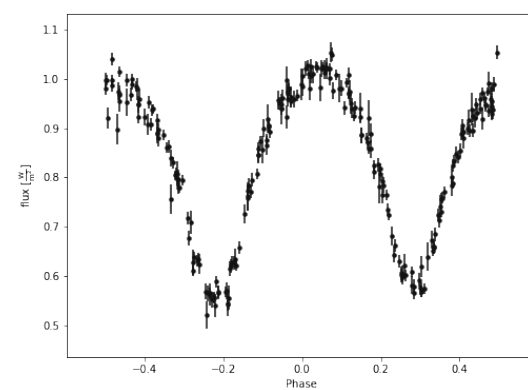


**(bf)** MHT 31948
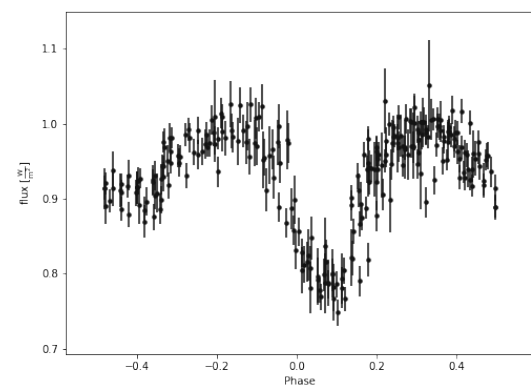


**(bg)** MHT 31956
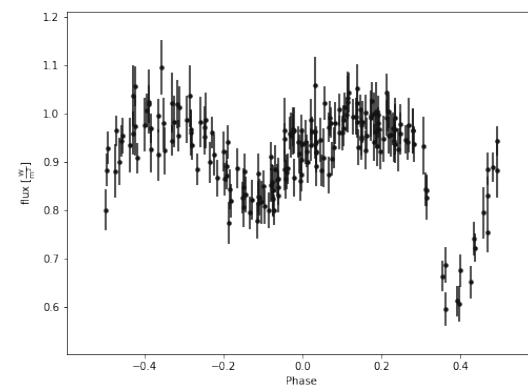


**(bh)** MHT 32190
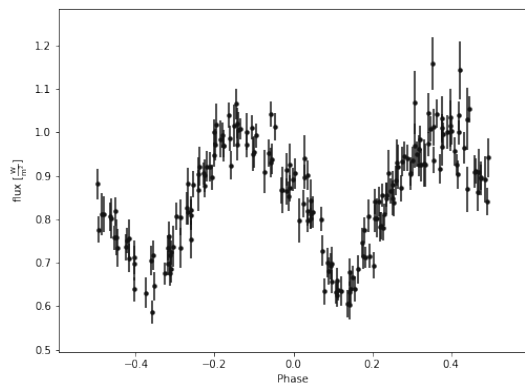
(bi) MHT 32831
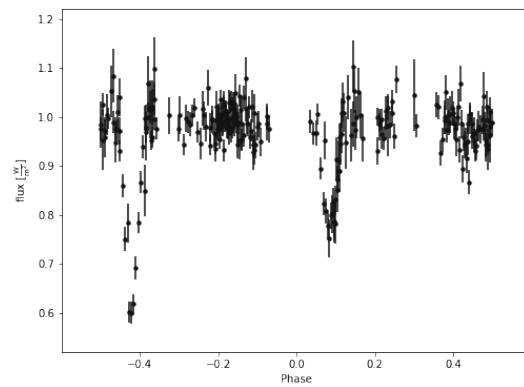


(bj) MHT 34595
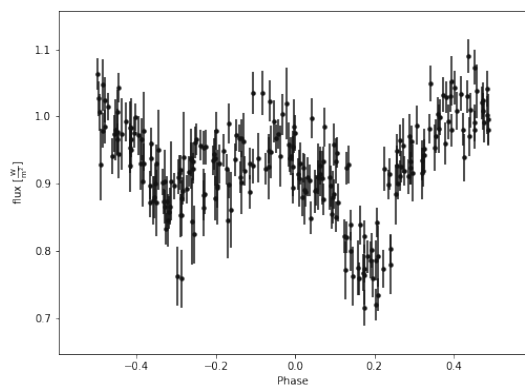


(bk) MHT 34596
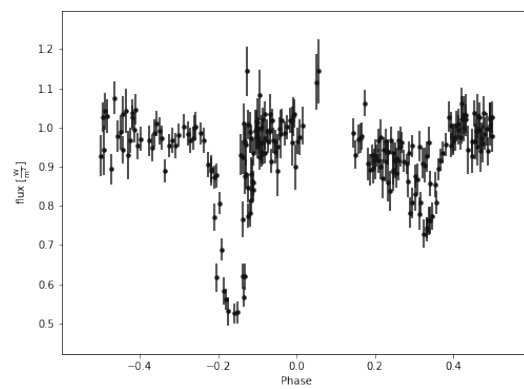


(bl) MHT 35564
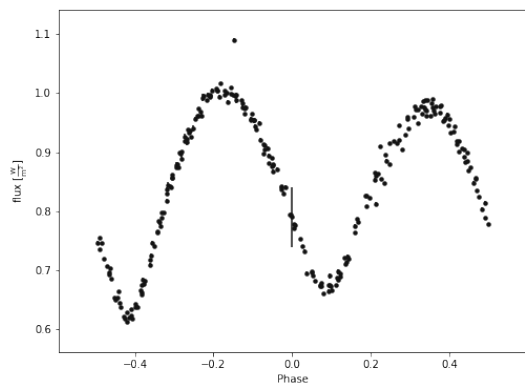


(bm) MHT 35712
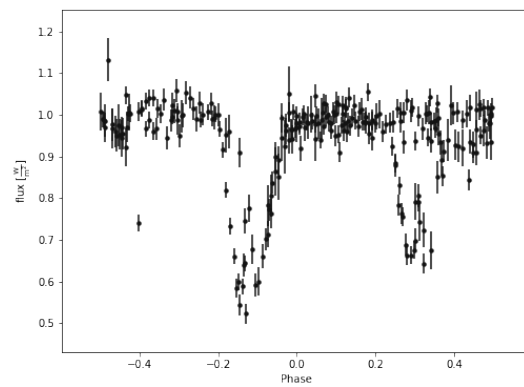


(bn) MHT 36815
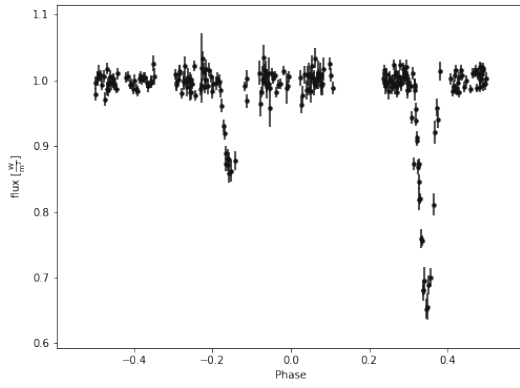
**(bo)** MHT 38795
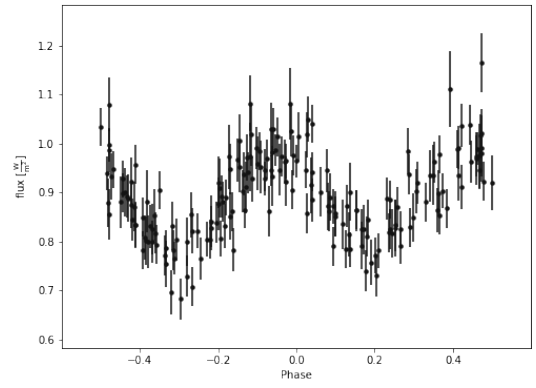


**(bp)** MHT 39408
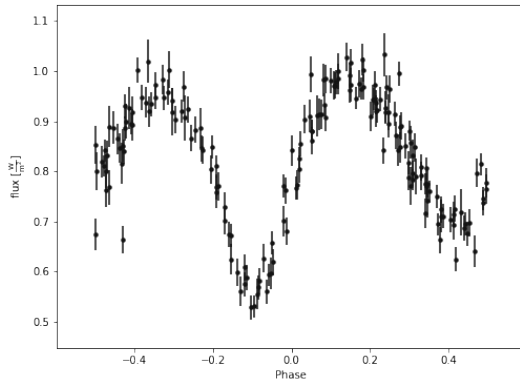


**(bq)** MHT 42898
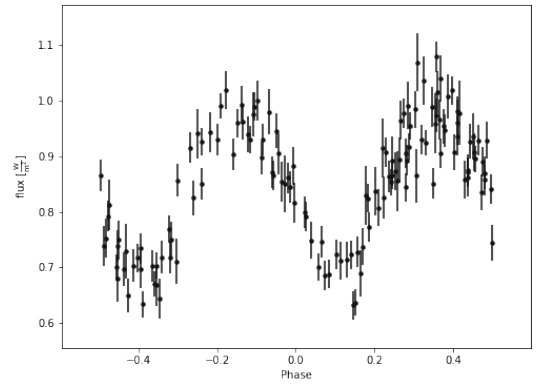


**(br)** MHT 48251

## 10.3 Appendix C: TESS Light Curves
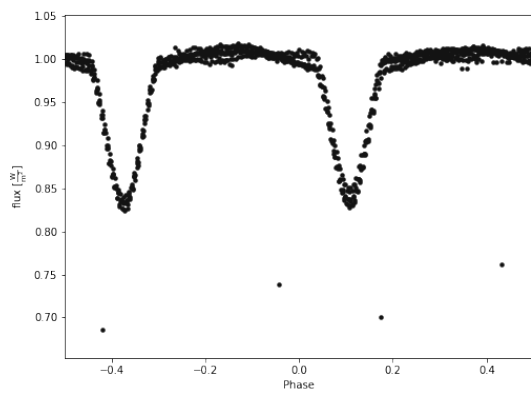


**(bs)** TIC 12638944 (MHT 3799)
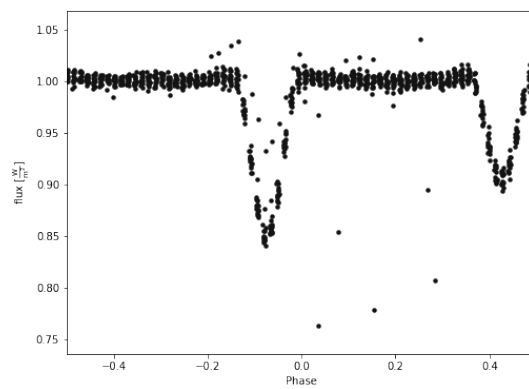


**(bt)** TIC 12410758 (MHT 4206)
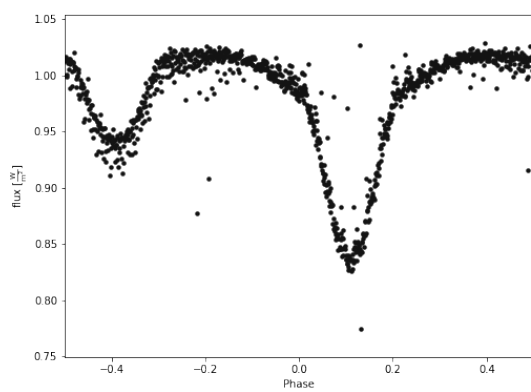


**(bu)** TIC 458865366 (MHT 4708)
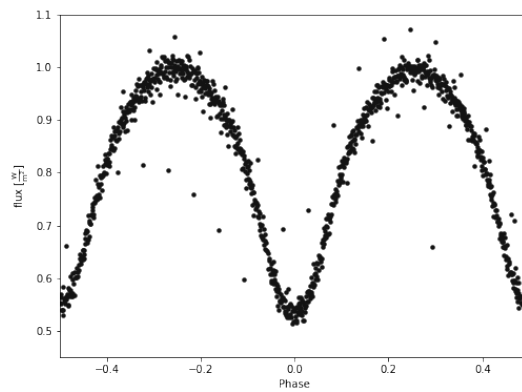


**(bv)** TIC 374394641(MHT 5720)
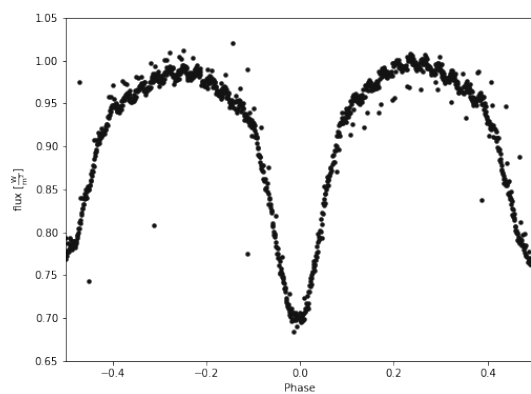
**(bw)** TIC 13526041 (MHT 6742)
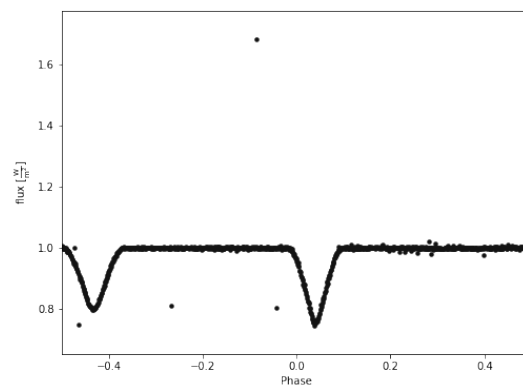


**(bx)** TIC 12833943 (MHT 12030)
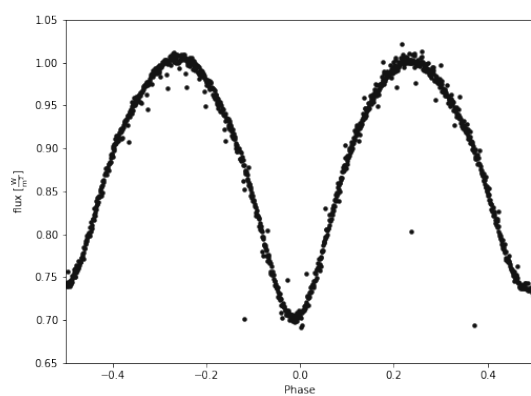


**(by)** TIC 357669270 (MHT 15185)
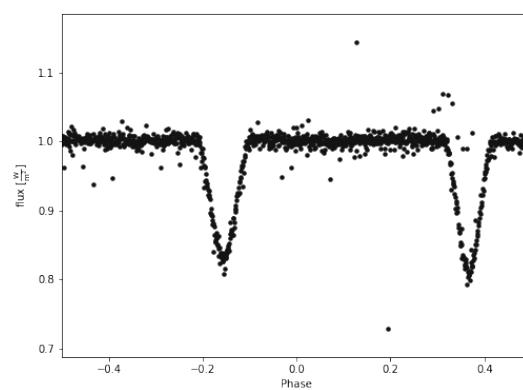


**(bz)** TIC 286123245 (MHT 20211)
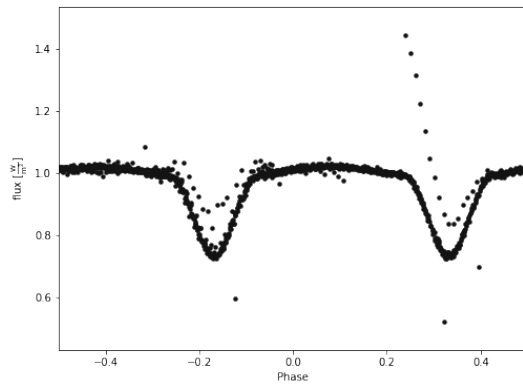
**(ca)** TIC 374222005 (MHT 22431)
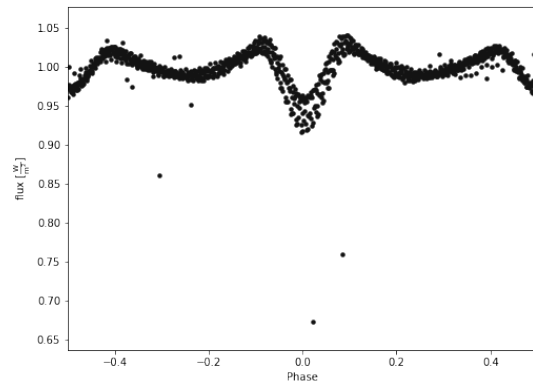


**(cb)** TIC 374398135 (MHT 26689)
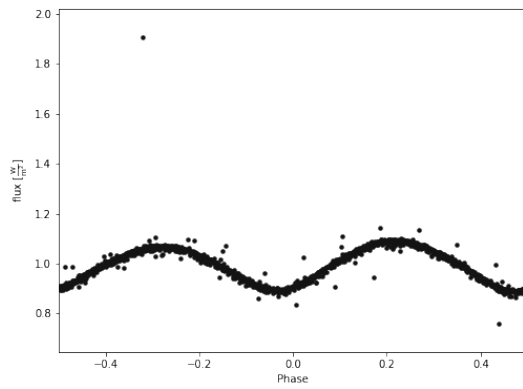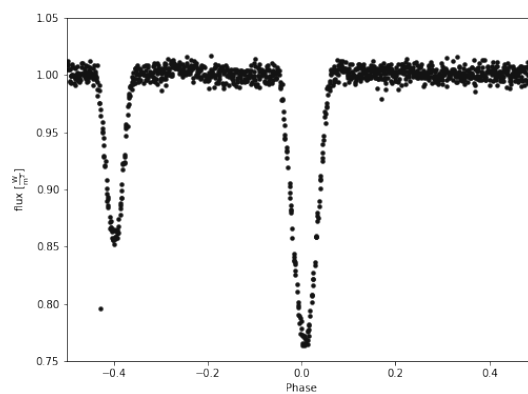


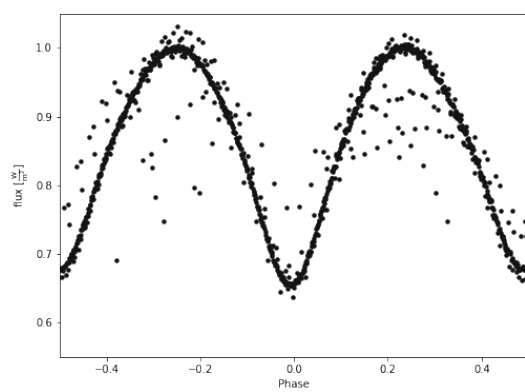**(cc)** TIC 423456116 (MHT 27033)
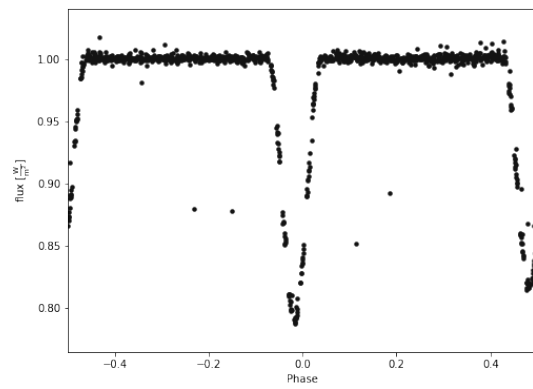


**(cd)** TIC 13266469 (MHT 28909)
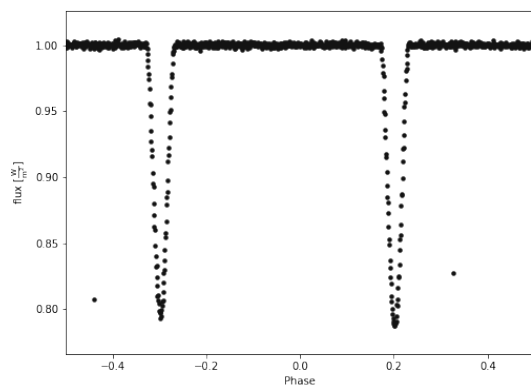
**(ce)** TIC 286125974 (MHT 30495)



**(cf)** TIC 285912631 (MHT 31867)



**(cg)** TIC 458845005 (MHT 35712)